Technical University of Denmark

DTU

# Improved optical solutions for on-chip light scattering detection

**Jensen, Thomas Glasdam**

*Publication date:*
2011

*Document Version*
Publisher's PDF, also known as Version of record

[Link back to DTU Orbit](#)

*Citation (APA):*
Jensen, T. G. (2011). Improved optical solutions for on-chip light scattering detection. Kgs. Lyngby, Denmark: Technical University of Denmark (DTU).

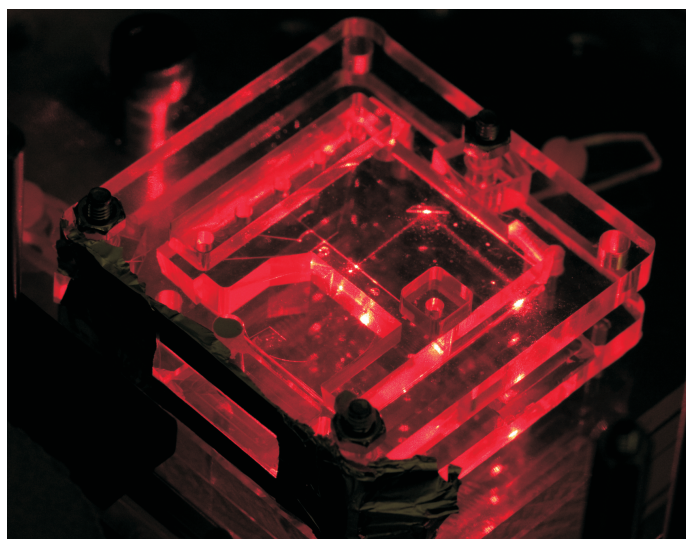**DTU Library**
Technical Information Center of Denmark

Ph.D Thesis

# Improved optical solutions for on-chip light scattering detection

Thomas Glasdam Jensen



Supervisor: Jörg P. Kutter

DTU Nanotech – Department of Micro and Nanotechnology
Technical University of Denmark

23 October 2010

**DTU Nanotech**
Department of Micro- and Nanotechnology

ii

# Abstract

Flow cytometry in microdevices has so far been limited to cells and particles with a size of several micrometers. However, by improving the sensitivity of these devices, such that particles in the low micrometer range and below can be detected, it may become possible to use integrated micro flow cytometers as a sensing tool for various bio-chemical assays in Lab-On-a-Chip (LOC) devices. This thesis presents the theory related to on-chip flow cytometry and describes the experiments performed with devices designed to push the limit of detection further towards submicrometer particles.

During this work, it was necessary to develop the LabVIEW program "RayLab" in order to be able to simulate the optical behavior of different waveguide/microlens configurations.

The first successful experiment was made with a microfluidic device consisting of a glass substrate with SU-8 and polydimethylsiloxane (PDMS) layers. The device contained integrated micro optical elements and a two-layer microchannel structure. With this channel structure it was possible to obtain on-chip three-dimensional (3D) hydrodynamic focusing over a wide range of Reynolds numbers (0.5<Re<20). Polystyrene particles of three sizes (2 $\mu$m, 1 $\mu$m, 0.5 $\mu$m) were measured in the microfluidic device demonstrating the feasibility of this approach to detect particles at or below 1 $\mu$m in diameter. To my knowledge, this is the first report of unlabeled particles in the 1 $\mu$m range having been measured by on-chip light scattering detection.

With the experience gained from the first chip, it was realized that the concept of coupling light in and out of the chip could be severely improved.

Hence, a novel chip design was developed, and the presentation in this thesis demonstrates the performance of a virtually alignment free optical set-up, which can be used for different microfluidic applications. It is shown how inexpensive external lenses combined with carefully designed on-chip lenses can be used to couple light from a bulk beam to on-chip waveguides and back into a bulk beam again. The proposed setup is based on a pin-aided alignment system that makes it possible to change chips in the optical train in only a few seconds with a standard deviation of about 2 % in the transmission intensity. The performance of this set-up was characterized by an optical test chip and a new flow cytometer chip, which demonstrated the possibility of detecting and counting polystyrene particles down to 1 $\mu$m at a rate of 100 Hz using this fiber free set-up.

# Resumé (in Danish)

Flowcytometri i mikroapparater har hidtil været begrænset til celler og partikler med en størrelse på flere mikrometer. Men ved at forbedre følsomheden af disse apparater, således at partikler i (og under) det lave mikrometer område kan påvises, kan det blive muligt at anvende integrerede mikro flowcytometre som sensor i forskellige bio-kemiske lab-On-a-Chip (LOC) enheder. Denne afhandling præsenterer den teori der vedrører on-chip flowcytometri og beskriver eksperimenter udført med anordninger beregnet til at flytte detektionsgrænsen længere mod submikrometer partikler.

Under dette arbejde, var det nødvendigt at udvikle LabVIEW programmet "RayLab" for at kunne simulere den optiske opførsel af forskellige bølgeleder og mikrolinse konfigurationer.

Det første vellykkede eksperiment blev lavet med en mikrofluid enhed bestående af et glas substrat med et SU-8 og et polydimethylsiloxan (PDMS) lag. Enheden indeholdt integrerede mikrooptiske elementer og en to-lags mikrokanal struktur. Med denne kanal struktur var det muligt at opnå on-chip tre-dimensionel (3D) hydrodynamisk fokusering over et bredt spektrum af Reynolds tal (0,5 <Re< 20). Polystyren partikler i tre størrelser (2 $\mu$m, 1 $\mu$m, 0,5 $\mu$m) blev målt i det mikrofluide apparat, og viser dermed at denne fremgangsmåde kan bruges til at detektere partikler på eller under 1 $\mu$m i diameter. Så vidt det vides, er dette den første rapport, der beskriver detektion af umærkede partikler i 1 $\mu$m størrelsen ved on-chip måling af spredt lys.

Med erfaringerne fra den første chip, blev det klart, at koblingen af lys, ind og ud af chippen, kunne forbedres betydeligt.

Derfor blev en chip med et nyt design udviklet, og præsentationen i denne afhandling demonstrerer egenskaberne af det justerings-fri optiske set-up, som kan bruges til forskellige mikrofluide applikationer. Det er vist, hvordan billige eksterne linser kombineret med omhyggeligt designet on-chip linser kan bruges til at koble lys fra en laser stråle til on-chip bølgeledere og tilbage til en laser stråle igen. Det foreslåede setup er baseret på en stålpind-baseret indretning, der gør det muligt at skifte apparater i det optiske tog på kun få sekunder med en standardafvigelse på cirka 2 % i transmissions intensitet. Egenskaberne af dette set-up blev testet med en optisk test-chip og en nydesignet flowcytometer chip, som påviste muligheden for at detektere og tælle polystyren partikler ned til 1 $\mu$m ved en tællehastighed på 100 Hz ved hjælp af dette set-up, helt uden brug af optiske fiber.

# Preface

This thesis was written as one of the requirements needed to obtain the PhD degree at the Technical University of Denmark (DTU). The Ph.D. study was supported by the European Commission through the Sixth Framework Programme, as part of the DetectHIV project. The Ph.D. project spanned from May 1st 2007 and until October 23rd 2010 at DTU Nanotech - Department of Micro and Nanotechnology. Throughout the project my supervisor has been:

Professor Jörg P. Kutter (DTU Nanotech)

I would like to take this chance to thank a lot of people who have been both kind and helpful to me during my time as a Ph.D student. First of all, I want to thank my supervisor Jörg P. Kutter, for showing a lot of confidence in me and letting me evolve this project according to my own decisions (or having used his awesome mind power to convince me so). Furthermore, I which to express my appreciation of the huge effort placed in correcting my English grammar throughout numerous reports, including this one.

Secondly, I wish to thank Guisheng Zhuang, who, as a PostDoc, participated in a large part of the work presented in this thesis, and especially helped with cleanroom fabrication and the development of the various employed PDMS moulding techniques. I also like to thank Santeri Tuomikoski for his collaboration through my first months on this project.

During this project I have had the honor of working together with a large group of international scientists, and though they were all greatly contributing to keeping me highly motivated, I especially wish to declare my appreciation of the great spirit of collaboration among the non-senior members of the DetectHIV project. Hence, I thank Yves Moser and Rana Afsahr from Switzerland and Julie Görge and Julien Charpentier from France, with whom I shared hundreds of emails discussing how to get all the pieces to fit.

I also want to thank my fellow Ph.D student Pelle Ohlsson for sharing office with me for three years. Throughout the years we have had many exiting conversations and I really admire your never ending curiosity and enthusiasm. Furthermore, I wish to thank Detlef Snakenborg for introducing me to the laboratories and especially to the milling machines and also Per Thor Jonassen for keeping everything up and running.

I wish to thank the entire ChemLabChip-group for creating a great working environment, and for making me truly appreciate the time spent in your company. The effort of people at DTU Danchip who patiently have instructed me in the use of the cleanroom machinery (in some cases more than once) is also highly appreciated.

I also wish to thank Massahiro Motosuke for willingly continuing my work. Knowing that the project will not be forgotten anytime soon is a great comfort. I wish you the best of luck.

Finally, I wish to give my thanks to friends and relatives for your emotional support. Especially, my beloved wife and daughter, who have shown me that there are more important things in life than differential equations and microfabrication.

*"If I have seen further it is only by standing on the shoulders of giants"*
-Sir Isaac Newton (15 February 1676)

Thomas Glasdam Jensen
DTU Nanotech – Department of Micro and Nanotechnology
Technical University of Denmark
23 October 2010

# Contents

# List of Figures

# List of Tables

# List of publications

## Peer review publications

- **<u>T. G. Jensen</u>**, L. Nielsen, J. P. Kutter. *"Fiber free coupling between bulk laser beams and on-chip polymer based multimode waveguides"*, Electrophoresis, 32(10):1224-32. doi: 10.1002/elps.201000593, 2011.
  Embedded as Section 7.3.

- G. S. Zhuang, **<u>T. G. Jensen</u>**, J. P. Kutter. *"Detection of Unlabeled Particles in the low Micrometer Size Range using Light Scattering and Hydrodynamic 3D Focusing in a Microfluidic System"*, Electrophoresis, 2012.
  Embedded as Section 6.2.

- D. Sabourin, M. Dufva, **<u>T. G. Jensen</u>**, J. P. Kutter, and D. Snakenborg. *"One-step fabrication of microfluidic chips with in-plane, adhesive-free interconnections"*. Journal of Micromechanics and Microengineering, 20(3):7, 2010.

- M. Hagster, **<u>T. G. Jensen</u>**, H. Bruus, J. P. Kutter. *"Acoustic resonances in microfluidic chips: full-image micro-PIV experiments and numerical simulations"*. Lab on a Chip, vol: 7, issue: 10, pages: 1336-1344, 2007.

- T. B. Christensen, C. M. Pedersen, K. G. Grøndahl, **<u>T. G. Jensen</u>**, D. D. Bang, A. Wolff. *"PCR biocompatibility of Lab-on-a-chip and MEMS materials"*. Journal of Micromechanics and Microengineering, vol: 17, issue: 8, pages: 1527-1532, 2007.

## Conference proceedings

- **<u>T. G. Jensen</u>**, J. P. Kutter. *"Fiber free plug and play on-chip scattering cytometer module - for implementation in microfluidic point of care devices"*, Proceedings of $\mu$TAS 2010, Groningen, The Netherland.

- **<u>T. G. Jensen</u>**, G. S. Zhuang, and J. P. Kutter. *"Highly sensitive on-chip submicrometer scattering cytometer module - for implementation in automated high throughput devices"* -, Proceedings of LabAutomation 2009, Palm springs, USA.

- O. Ordeig, P. D. Ohlsson, **T. G. Jensen**, G. S. Zhuang, K. B. Mogensen, D. Snakenborg, J. P. Kutter. *"Integrated waveguides for various detection schemes in microfluidic systems"*, Proceedings of LabAutomation 2009, Palm springs, USA.

- G. S. Zhuang, **T. G. Jensen**, and J. P. Kutter. *"Three-dimensional hydrodynamic focusing over a wide Reynolds number range using a two-layer microfluidic design"*, Proceedings of $\mu$TAS 2008, San Diego, USA.

- M. Sundin, **T. G. Jensen**, H. Bruus, J. P. Kutter. *"Full image micro-PIV analysis of transient and stationary flow patterns in microfluidic structures under piezo actuation"*. Proceedings of $\mu$TAS 2006, Tokyo, Japan.

# Introduction

After the discovery and following successful miniaturization of the transistor in the 1950s our world has been revolutionized by the ever increasing availability of smaller, smarter and cheaper electronic devices. Today, thanks to miniaturization and integration, transistors (and electronics in general) are a key component in a wide variety of products ranging from children's toys to space shuttles and kitchen appliances.

The scientific research field 'Microfluidics' started to take off in the early 1990s where Manz *et al.* [1] were among the first to introduce and discuss the concept of 'Micro Total Analysis Systems ($\mu$TAS)' or 'Lab-On-a-Chip (LOC)' devices. A major goal of this research field was (and still is) to recreate the same exponential growth in functional capabilities, positive influence on public life quality and reduced production costs in the chemical field as has been the case in the electronic field. Miniaturization of chemical analysis systems, allow for the possibility to perform the analysis with less sample consumption, under much better controlled conditions and often much faster than with conventional techniques. But even more importantly, it becomes possible to integrate the functionality from several conventional instruments in the same device.

The possible applications of microfluidic systems are widespread, from home pregnancy test to state of the art DNA sequencers. Even at very large facilities, such as chemical production plants or water treatment centers, there is a need for micro systems in the shape of cheap inline sensors for improved quality control.

## 1.1 Point of care diagnostics

Based on their proximity to the so-called 'Point Of Care'(POC) most $\mu$TAS devices can be divided into three groups: True POC devices for non-technical end-users, semi-POC devices for field-technicians and non-POC devices for laboratory experts. The main difference between these three groups is distance between the sample and the test result in terms of both time, cost and geography. Ideally, all devices should be true POC, this is, however, far from always possible as production costs and device complexity can make it unfeasible. Even though the POC-concept traditionally relates to medical treatment and diagnostics, the term can, in the context of $\mu$TAS devices, be used in other fields as well.

The most expensive and often also most complicated systems are limited to experts

at clinical laboratories and research facilities. These devices may either depend on non-trivial handling, provide such complex (or general) results, that only experts can confidently interpret the actual test outcome, or they are used so rarely that they only become economically viable when samples are accumulated from a large geographical area.

The group of least complex devices are often targeted directly at the non-technical end-users. To avoid misinterpretations the output from these devices is often either binary or limited to a single value (concentration, pH, etc.).

The intermediate class of devices often includes highly task-specific instruments, which are both too complex and expensive to appeal to actual end-users, but at the same time compact and robust enough to be used outside laboratories. Hence, the devices can be portable enough to be transported from site to site by car, or small enough to fit inside a doctor's office. In both cases, providing a non-optimal sample collection, but with immediate result.

Exemplified with environmental monitoring of water quality in a river, the level of true POC corresponds to having a devices permanently placed in the water, continually displaying (transmitting, recording, etc.) the measured quantity. The level of semi-POC could, for instance, be bringing the same instrument from one river site to another to perform the test. The level of non-POC would be to collect the water sample in a bottle and then send it to a central laboratory for testing.

A similar example can be made with medical diagnostics, comparing a home test, a test at the local doctor's office, and having a sample taken at the doctor's office and then having to wait two weeks for the result, while the sample is shipped, tested and evaluated.

Hence, in order for a device to be classified as a POC device, it must be cheap, easy to use and provide the result on location, within reasonable time. This kind of classification is naturally ambiguous, as a device might be considered POC in a wealthy western country, while semi- or non-POC in third world countries, simply because of the associated price tag.

### 1.1.1 The advantages of POC testing

There are many advantages of pushing the development of $\mu$TAS devices closer towards POC. The first and possibly largest advantage of a POC device is its user friendliness. Not in the sense that a given device is easy to handle (because that is a requirement), but that it will always be the easiest choice for the user to perform the test immediately and at the point of care.

A second great advantage of POC devices is that the increased availability of the test will lead to earlier testing, and therefore also earlier diagnostics. The earlier a problem is discovered and identified the faster and more efficient counter measures can be taken. This holds for both diseases, production line errors, and environmental contamination. Not only does a high POC level induce earlier diagnostics, it also makes it possible to perform more frequent tests. Within medicine, the ability to run frequent tests makes it possible to monitor the state of a patient more closely. By monitoring patients during therapy, the obtained feedback can be used to evaluate the response to the provided treatment. Should the treatment work less efficiently than supposed, it is immediately possible to

adapt it, thereby personalizing the treatment. The ability to personalize treatment is especially important with rapidly evolving diseases such as cancer, where the cells can evolve resistance to an initially effective drug.

Another important aspect of increased patient monitoring is the possibility to control the patient compliance. It is, of course, very important to be able to distinguish whether a treatment is failing because of the resistance of the disease itself or because the patient is not fully cooperating.

In conclusion, the many advantages of a high POC level makes it clear why it, in some cases, make sense to set a high POC level as goal in device development rather than test speed or accuracy. In many cases, it may even be fruitful to sacrifice sensitivity in order to get closer to the point of care.

## 1.2   Flow Cytometry

The work presented in this thesis has been oriented towards the miniaturization of a specific instrument used for cell detection and analysis in biochemical assays, the flow cytometer. The main reason to miniaturize the flow cytometer is to make it an integrateable module for $\mu$TAS devices. Normally the term 'cytometer' implies that cells are being measured. However, despite the fact that this work have almost exclusively been oriented towards the detection of polystyrene particles, I will keep referring to the devices as cytometers, as the detection principles are identical.

### 1.2.1   Conventional flow cytometry

In conventional flow cytometry a stream of suspended particles is counted and analyzed as it passes a beam of light. When the individual suspended particles get illuminated the incident light gets scattered, and by placing detectors at different angles it becomes possible to measure the intensity change in the scattered light and thereby detect the passing of each particle. With conventional flow cytometers the particles (or cells) are often labeled with a fluorescent marker to help discriminate between several mixed populations. Naturally, the more parameters that are simultaneously measured the more precise the test becomes and the easier it becomes to separate multiple populations. Hence, many commercial cytometers are fitted with several different excitation lasers, and numerous optical detectors equipped with filters to monitor several independent fluorescent signals. In some cases, the optical measurements are combined with electric impedance measurements obtained with Coulter counters. Some commercial suppliers claim their devices are able to provide measurements of up to 29 possible parameters [2]. A simplified sketch of a conventional flow cytometer is shown in Fig. 1.1. One of the main tasks performed by conventional flow cytometers is fluorescent activated cell sorting (FACS) [3], where cell populations are sorted based on their fluorescent signature.

### 1.2.2   Miniaturized flow cytometry

Even though the performance of conventional flow cytometers is very good, they suffer from being stand-alone-devices, which means that any kind of sample treatment prior to the cytometric detection must be performed before loading the sample into the cytometer. Hence, some kind of sample handling will be required, which often adds to reduced reproducibility and human error. Though certain high-end cytometers (such as the FC500 Flow Cytometer, Fluofarma, France) are somewhat automated as they are designed for easy integration with pippeting robots, the size and price of such devices makes them undesirable for most laboratories. So in order to avoid the need for having a conventional flow cytometer present to analyze the sample output from a $\mu$TAS device, it is highly desirable to develop a miniaturized cytometer module that can be integrated on-chip. By integrating the cytometer on-chip the sample can by directly injected, without ever leaving the chip. This a huge advantage, as the sample is kept in the same environment and it makes automation of the assay much easier.

When designing a $\mu$TAS device it is important, early in the design phase, to decide to what level the various components should be integrated. In one extreme, all components are integrated on-chip, including valves, light sources, detectors etc. This makes the use of additional instrumentation very limited, but at the same time makes the chip very expensive. Hence, to be economically feasible the chip must be able to perform a task numerous times. In cases where the sample consist of blood or other highly contaminating substances it becomes very difficult to clean the chip sufficiently to avoid cross contamination. In such cases it may be more feasible to keep the expensive components off chip, thereby making the chip fabrication cheap enough for the chips to be considered disposable after a single test. By using cheap disposable chips combined with a reusable instrument, the cost per test will decrease with the number of tests. This gives, in some cases, an advantage compared to the more constant price of a fully integrated chip. The chips described throughout this thesis have been made according to the disposable style as the chips are intended for medical use (see Chapter 5). The use of an on-chip integrated cytometer will be highly specific compared to a conventional stand alone cytometer. This means that the number of interesting detectable parameters may be drastically decreased as the application may only need one or two parameters to sufficiently detect the particles. In the work presented in this thesis, only the intensity of forward scattered light has been tested. Hence, neither fluorescent nor electrical measurements have been invoked. The sketch shown in Fig. 1.1 shows a possible layout of a mono-layered micro-device.
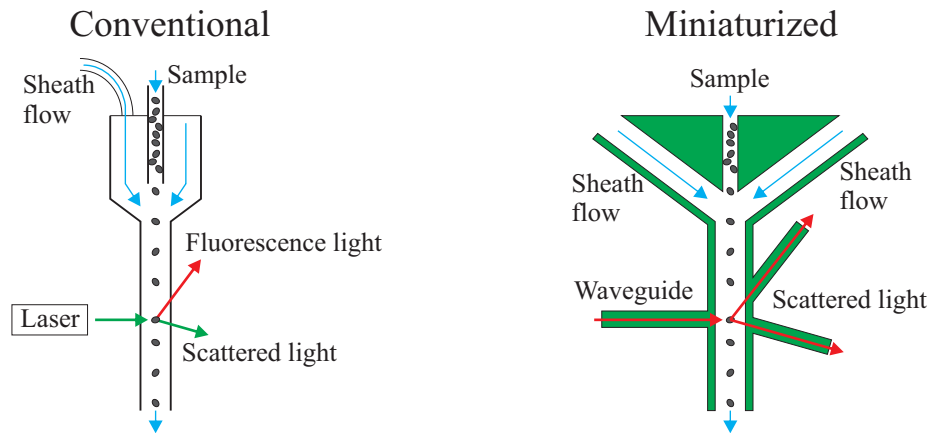
*Figure 1.1: This figure shows a sketch of a conventional and a miniaturized flow cytometer*

A further technical comparison of state of the art miniaturized flow cytometers is found in section Section 6.2.3.

## 1.3 The importance of packaging

It is, today, twenty years ago that the $\mu$TAS field was started. Though this field, already from the start, showed very promising capabilities, the lack of commercial successes is surprising. Keeping in mind that it only took the computing industry about twenty years from the first transistor was made in silicon in 1954 at Texas Instruments to the first computers became available for home usage in 1975. Despite the successes from a few lateral flow immunochromatographic assays (such as the home pregnancy test), the electrochemical glucose meter and the inkjet printers, the big commercial breakthrough seem to be missing still. This concern was recently phrased by George Whitesides [4] as:

*"Many people, myself included, expected that the ability to manipulate fluid streams, in microchannels, easily, would result in a proliferation of commercial LoC systems, and that we would see applications of these devices proliferating throughout science. In fact, it has not (yet) happened."*

What appears to be the barrier between the scientific successes and commercialization, is that the Lab-On-a-Chip concept more than often is reduced to Chip-in-a-Lab. In many cases, the excessive need for external equipment, such as detectors, amplifiers and even microscopes, makes the chips too expensive to commercialize. Furthermore, it must also be acknowledged that the field of microfluidics is much more difficult compared to that of electronics. Roughly speaking, you only have one entity to move around in electronics, the electrons, which all are exactly the same and behave identically. In microfluidics you have to deal with numerous different entities as proteins, cells and particles are suspended in various media. In that context, it is perhaps a bit optimistic to expect the same growth.

As mentioned above (in Section 1.2.2) external equipment is not necessarily a bad thing. But it needs to be well implemented with the chip, which is often not the case. When working with microfluidic (and microoptical) devices, there exists a very difficult balance between spending time on the development of the actual chip functionalities and the chip infrastructure (connections, etc.). By neglecting the development of the chip-to-world interface, a more intensive work effort can be put into optimizing the device performance. The drawback might, however, come as tedious handling of the device, poor reproducibilities and inconclusive results from the otherwise optimized device. An increased effort placed in the chip infrastructure can be seen as an investment that might pay off if the following development of the device is successful. If the development fails, the investment might be lost as new approaches may not be compatible. Finally,it does not make much sense either to develop a device that outperforms all competitors in terms of detection sensitivity only to find it impossible to commercialize due to complex alignment and fittings issues.

In this thesis, two manuscripts are embedded (Sections 6.2 and 7.3), they each describe a different approach to developing an on-chip flow cytometer. The first focuses on the performance of the device, where the second is more oriented towards optimizing the chip infrastructure. Though both chips provide a functional module, they both need further improvement before their implementation into commercial products is realistic. While the performance of the fiber-based module is clearly better than the lens-based, I find it much more likely that the lens-based solution eventually could be commercialized thanks to the much better packaging of the chip. Furthermore, in yet another attempt to improve general chip infrastructure, I took part in a third paper on fluidic connections [5].

## 1.4   Thesis outline

After this introductory chapter, I will start by explaining the basic optical theory in Chapter 2. In Chapter 3, I briefly discuss the concept of ray tracing, and why i had to make my own script-compiler. In Chapter 4, the basic theory behind microfluidics is described. Next in Chapter 5, I will introduce the DetectHIV project and its influence on why and when things were done. Chapter 6 describes the experiments and results obtained with devices based on optical fibers. In Chapter 7, I describe the so-called lens-based devices. Finally, I wrap up in Chapter 8 with a concluding chapter.

# Applied optics

This chapter is devoted to a practical approach to a few selected optical topics. The first part of the chapter discusses optics in general with a focus on geometric optics to show that raytracing is a valid tool for analyzing vast multimode waveguide structures. The second part of this chapter discusses the different types of scattering, such as Rayleigh-, geometric- and, especially, Mie scattering.

## 2.1 Basic optics

When describing the nature of light one typically invokes the Maxwell's equations [6]

$$\text{(I)} \ \boldsymbol{\nabla} \cdot \mathbf{E} = 0, \quad \text{(II)} \ \boldsymbol{\nabla} \cdot \mathbf{B} = 0, \quad \text{(III)} \ \boldsymbol{\nabla} \times \mathbf{E} = -\frac{\partial \mathbf{B}}{\partial t}, \quad \text{(IV)} \ \boldsymbol{\nabla} \times \mathbf{B} = \mu\epsilon\frac{\partial \mathbf{E}}{\partial t}. \quad (2.1)$$

Here $\boldsymbol{\nabla} = (\partial_x, \partial_y, \partial_z)$ and $\mathbf{E}$ and $\mathbf{B}$ are the electric and magnetic field, respectively. We assume the material is homogeneous and free of charge and current, and that both the vacuum permittivity, $\epsilon = \epsilon_r\epsilon_0$ and the vacuum permeability, $\mu = \mu_r\mu_0$ are constant in time and space. By taking the curl of (III) and (IV) it can be shown that $\mathbf{E}$ and $\mathbf{B}$ can be decoupled and that each fulfills the three-dimensional wave equation with a traveling speed of

$$v = \frac{1}{\sqrt{\epsilon\mu}}. \quad (2.2)$$

The ratio between the speed in vacuum and in a given media is called the refractive index denoted by

$$n = \frac{c}{v} = \sqrt{\frac{\epsilon\mu}{\epsilon_0\mu_0}}. \quad (2.3)$$

Due to the complex nature of the permittivity for non-perfectly insulating materials, the refractive index is often defined as $n = m - i\kappa$, where $m$ is real refractive index and $\kappa$ is the absorption (or sometimes extinction) coefficient. We will however neglect the effects of absorption in this thesis unless otherwise noted. Hence, the refractive index reduces to $n = m$.

### 2.1.1   The three fundamental laws of geometrical optics

In the following, we shall study what happens when a single plane monochromatic wave hits the interface to another (non-conducting) medium at an arbitrary incident angle. The only restraint we put on the studied geometry is the position of the interface, which we place in the $xy$ plane at $z = 0$. The incident wave hits the interface at an angle $\theta_I$ relative to the interface normal, here the z-axis (see Fig. 2.1). The incident wave is defined by its electric field as $\mathbf{E}_I(\mathbf{r}, t) = \tilde{\mathbf{E}}_I e^{i(\mathbf{k}_I \cdot \mathbf{r} - \omega t)}$, where $\tilde{\mathbf{E}}_I$ is an amplitude vector independent of space and time and $\mathbf{k}$ is the propagation vector ($|\mathbf{k}| = 2\pi/\lambda$). $\omega = 2\pi c/\lambda$ is the angular frequency. When the incident wave hits the interface it gives rise to a reflected wave and a refracted wave, denoted by $\mathbf{E}_R(\mathbf{r}, t) = \tilde{\mathbf{E}}_R e^{i(\mathbf{k}_R \cdot \mathbf{r} - \omega t)}$ and $\mathbf{E}_T(\mathbf{r}, t) = \tilde{\mathbf{E}}_T e^{i(\mathbf{k}_T \cdot \mathbf{r} - \omega t)}$, respectively. The two new waves leave the interface at the angle of reflection, $\theta_R$, and the angle of refraction, $\theta_T$, respectively.
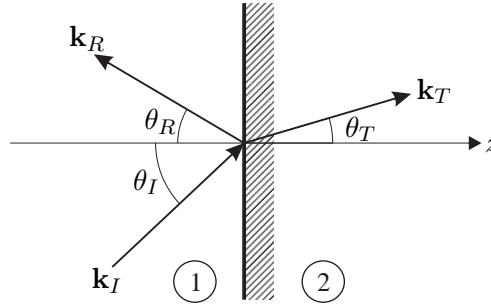


*Figure 2.1: When an electromagnetic wave hits an interface between two media it causes a reflected and a refracted wave*

Since all three waves originate from the same source their angular frequency, $\omega$, must be equal. Hence,

$$|\mathbf{k}_I| v_1 = |\mathbf{k}_R| v_1 = |\mathbf{k}_T| v_2 = \omega \qquad \Rightarrow \qquad |\mathbf{k}_I| = |\mathbf{k}_R| = \frac{v_2}{v_1}|\mathbf{k}_T| = \frac{n_1}{n_2}|\mathbf{k}_T|, \qquad (2.4)$$

where subscripts 1 and 2 refer to the media. The boundary conditions at the interface all share the same overall structure at $z = 0$, given by

$$( \,) e^{i(\mathbf{k}_I \cdot \mathbf{r} - \omega t)} + ( \,) e^{i(\mathbf{k}_R \cdot \mathbf{r} - \omega t)} = ( \,) e^{i(\mathbf{k}_T \cdot \mathbf{r} - \omega t)} \qquad (2.5)$$

where only the exponentials depend on space and time. So, for the fields to match up everywhere on the surface at all times we can conclude that

$$\mathbf{k}_I \cdot \mathbf{r} = \mathbf{k}_R \cdot \mathbf{r} = \mathbf{k}_T \cdot \mathbf{r}, \quad \text{when } z = 0. \qquad (2.6)$$

Since both our x- and y-axis lie at the plane of the interface we may chose to evaluate Eq. (2.6) where also $x = 0$ or $y = 0$. Hence, the $\mathbf{k}$-components can be separated into

$$k_{Iy} = k_{Ry} = k_{Ty}, \quad \text{when } z = x = 0 \qquad (2.7)$$

and

$$k_{Ix} = k_{Rx} = k_{Tx}, \quad \text{when } z = y = 0, \tag{2.8}$$

where the added subscript $x/y$ indicates the $x/y$-component. Since we are free to orient the coordinate system as we like, we can choose to rotate it such that $\mathbf{k}_I$ lies in the xz-plane, thereby defining $k_{Iy} = 0$. Hence, according to Eq. (2.7) $\mathbf{k}_R$ and $\mathbf{k}_T$ also lie in the xz-plane. We have hereby deduced the first law of geometrical optics:

- The incident, the reflected and the transmitted wave form a plane called the 'plane of incidence'. This plane also includes the surface normal [6].

By noting that Eq. (2.4) states that $|\mathbf{k}_I| = |\mathbf{k}_R| = \frac{n_1}{n_2}|\mathbf{k}_T|$ and by using trigonometry to rewrite Eq. (2.8) into

$$|\mathbf{k}_I| \sin \theta_I = |\mathbf{k}_R| \sin \theta_R = |\mathbf{k}_T| \sin \theta_T, \tag{2.9}$$

we deduce the second law:

- The angle of reflection, $\theta_R$ equals the angle of incidence, $\theta_I$.

$$\theta_R = \theta_I. \tag{2.10}$$

And also the third law:

- The ratio of the sines of the angles of incidence and refraction is equivalent to the opposite ratio of the refractive indices.

$$\frac{\sin \theta_T}{\sin \theta_I} = \frac{n_1}{n_2}, \tag{2.11}$$

widely known as Snell's law.

## 2.2  Optical waveguides

If Snell's law is rephrased to $\sin \theta_T = \frac{n_1}{n_2} \sin \theta_I$ and we further note that the value of $\sin(x) \leq 1$, then we can deduce that in the case where $\frac{n_1}{n_2} > 1$ there will be certain values of $\theta_I$ for which it is impossible to find a $\theta_T$ that fulfills Snell's law. Hence, when $\frac{n_1}{n_2} > 1$ the largest possible angle of incidence that results in a refracted wave is called the 'critical angle', $\theta_c$. The critical angle corresponds to $\sin \theta_T = 1$ and is given by

$$\theta_c = \arcsin\left(\frac{n_2}{n_1}\right), \tag{2.12}$$

If we imagine the two media being SU-8 (n=1.59) and air (n=1) where the incident light approaches the interface from the SU-8 side, then $\theta_c = 39°$. This means that for incident angles larger than $39°$ all the intensity from the incident wave is reflected. This is illustrated in Fig. 2.2.
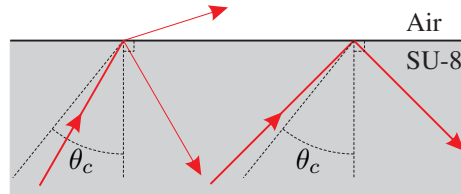
*Figure 2.2: When the incident wave comes from the medium with higher refractive index, it will only be refracted if the incident angle is less than the critical angle*

This phenomenon, where all the intensity is kept within the higher refractive index region, is called 'total internal reflection', often abbreviated 'TIR'. By designing a construction, so that a material with high refractive index is surrounded on all sides by materials with lower refractive indeces, TIR can be exploited to create waveguides and optical fibers.
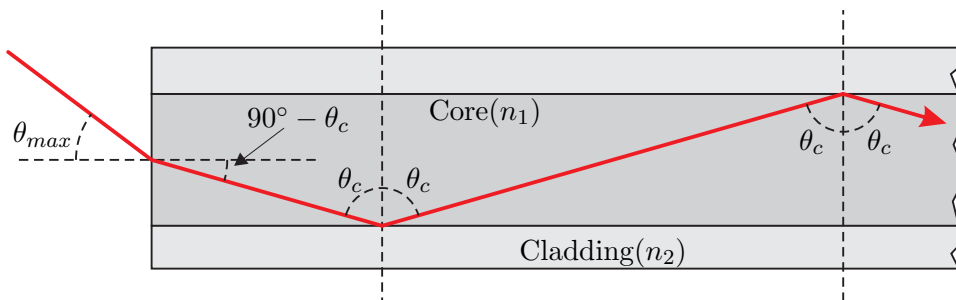


*Figure 2.3: A layered structure of dielectric materials can guide light if the core material has a higher refractive index than the cladding*

This description of waves propagating by total internal reflection is only valid for waveguides with length scales much larger than the guided wavelength. If the width of the waveguide approaches the wavelength and the difference in refractive indices becomes too small, it becomes necessary to solve electromagnetic waveequation, derived from Maxwell's equations, for that particular structure. Thereby finding the solutions corresponding to the different allowed eigenvalues. These solutions are usually referred to as the modes supported by the structure in question. The modes describe the spacial intensity distribution of the actual oscillations in the electric and magnetic fields. But in the case where the waveguide becomes sufficiently large the number of modes[7] and the crosstalk between them becomes so large, that it is sufficient to characterize the waveguide by the critical angle and the refractive index of the waveguide core. Since the waveguides used in this thesis are all approximately 75 $\mu$m high and have a minimum width of 30 $\mu$m, they are vastly multimodal for red light. Hence, this simplification makes it possible to analyse the used waveguide structures using ray-tracing, a concept further explored in Chapter 3.

## 2.3   Types of scattering

When a ray of light hits a particle several types of interactions may occur. In this thesis, we only focus on elastic scattering (redirection of the light) rather than in-elastic events such as Raman scattering [8], fluorescence [9] and absorption [9], where energy is transferred to the particle/molecule. Furthermore, we shall limit the study to homogeneous dielectric spheres. When analysing how light is scattered by a particle the correct approach would be to write up and solve Maxwell's equations. This is, unfortunately, not an easy task as the calculations, in spherical coordinates, are both lengthy and cumbersome. Hence, to ease the mathematics we look for possible shortcuts. To find the shortcuts, we study the size parameter, $\alpha$, defined as

$$\alpha = \frac{2\pi r_p}{\lambda_m}, \tag{2.13}$$

where $r_p$ is the radius of the particle and $\lambda_m$ is the wavelength of the light in the surrounding medium. The physical importance of this parameter relates to the nature of the dipole moment induced in the particle. This allows us to divide the nature of elastic scattering into three domains:

$$\alpha \ll 1 \quad \Rightarrow \quad \text{Rayleigh scattering} \tag{2.14a}$$
$$\alpha \gg 1 \quad \Rightarrow \quad \text{Geometric scattering} \tag{2.14b}$$
$$\alpha \approx 1 \quad \Rightarrow \quad \text{Mie scattering} \tag{2.14c}$$

Since the measurements presented in this thesis concern particles with diameters in the 1 $\mu$m-range using light sources with wavelengths around 635 nm, we fall into the Mie-scattering category.

### 2.3.1   Rayleigh scattering ($\alpha \ll 1$)

The concept of Rayleigh scattering was developed by and named after the British Lord Rayleigh. From the definition of the size parameter in Eq. (2.13), we see that when $\alpha \to 0$ the particle size becomes smaller and smaller compared to the wavelength of the incident light. This means that the entire particle experience the same value of the applied electric field, $\mathbf{E}_0$. Hence, the induced dipole moment, $\mathbf{p}$, is found to be $\mathbf{p} = 4\pi\epsilon_m a\mathbf{E}_0$, where $\epsilon_m$ is the permitivity of the media and $a$ is the polarizability of the particle, defined as

$$a = r_p^3\left[(\epsilon_p - \epsilon_m)/(\epsilon_p + 2\epsilon_m)\right]. \tag{2.15}$$

The periodic oscillations of the induced dipole moment then becomes a source for a secondary electromagnetic wave (the scattered light). The intensity of this scattered wave ($I_{sca}$) can then be calculated [10] as the sum of a wave ($I_\perp$) perpendicular to the source-particle-observer plane and a wave ($I_\parallel$) parallel to the plane:

$$I_\perp = I_{0\perp}k^4 a^2/d^2 \tag{2.16a}$$
$$I_\parallel = I_{0\parallel}k^4 a^2 \cos^2\theta/d^2 \tag{2.16b}$$
$$I_{sca} = I_\perp + I_\parallel = (I_{0\perp} + I_{0\parallel}\cos^2\theta)k^4 a^2/d^2. \tag{2.16c}$$

Where $d$ is the distance to the particle, $k = 2\pi/\lambda_m$ is the wavenumber and $\theta$ is the scattering angle. If the incoming light is unpolarized, then $I_{0\perp} = I_{0\parallel} = I_0/2$ and Eq. (2.16c) becomes

$$I_{sca} = \frac{I_0}{d^2} a^2 \left( \frac{2\pi}{\lambda_m} \right)^4 \frac{1 + \cos^2 \theta}{2}. \tag{2.17}$$

Inserting $a$ from Eq. (2.15) we get

$$I_{sca} = I_0 \frac{8\pi^4 r_p^6}{d^2 \lambda_m^4} \left( \frac{\widehat{n}^2 - 1}{\widehat{n}^2 + 2} \right)^2 (1 + \cos^2 \theta), \tag{2.18}$$

where $\widehat{n}$ is the relative refractive index. From Eq. (2.18) several physical properties of Rayleigh scattering are revealed. The first thing we notice is that if the particle and the medium have the same refractive index then no light is scattered ($\widehat{n} = 1 \Rightarrow I_{sca} = 0$). Secondly, we notice that the scattering intensity is proportional to the particle radius to the sixth power ($I_{sca} \propto r_p^6$). Finally, we notice that the scattering intensity is proportional to the inverse wavelength to the fourth power ($I_{sca} \propto \lambda_m^{-4}$). The proportionality to the inverse wavelength is the effect responsible for the increase in propagation loss in optical fibers and waveguides when going to shorter wavelengths.

Finally, it is noted that Rayleigh scattering from molecules in the atmosphere is causing the sky to appear blue, as the shorter wavelengths are scattered more intensively.

### 2.3.2 Geometric scattering ($\alpha \gg 1$)

When $\alpha \to \infty$ the particle becomes much larger than the wavelength of the incident light. It then becomes reasonable to treat the scattering process using the simpler geometric optics where the wavefronts are substituted with individual rays as shown in Fig. 2.4.
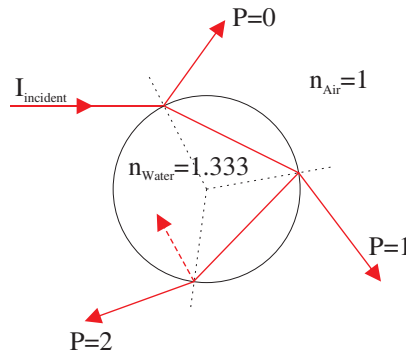


*Figure 2.4: This picture shows a raytrace simulation of a single ray of light hitting a spherical drop of water, the light is both reflected and refracted multiple times. When the particle is much larger than the wavelength it becomes possible to calculate the forward angle scattering with reasonable precision*

The rays scattered from the sphere are enumerated as $P$, where $P - 1$ is the number of internal reflections. By studying the intensity contributions from the different P-rays

it was possible for Descartes to explain the angles of the primary and secondary rainbow. The explanation was later extended by Newton, who included the sequence of the colors. According to [11] it can be shown that geometrical optics provides a very useful tool for forward angle scattering when $\alpha \gg 1$. The derivation is omitted here, as it falls beyond the scope of this thesis. The general concept of raytracing is further discussed in Chapter 3.

### 2.3.3 Mie scattering

In the Mie domain there are no shortcuts to calculate the scattered intensities, Maxwell's equations must be solved, preferably in spherical coordinates. This rather complex task was first solved by German physicist Gustav Mie in 1908 [12]. Since the Mie-solution is comprehensive, it can be applied to all values of $\alpha$. Unlike in the case of Rayleigh scattering, the Mie-solution is far too complex in its final form to immediately reveal any physical properties. To illustrate this point the solution is 'briefly' summarized below closely following the work of M. Kerker [13].

#### 2.3.3.1 The far field solution

Given the geometry shown in Fig. 2.5
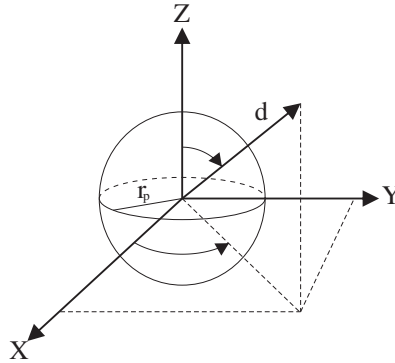


*Figure 2.5: Geometric overview of the scatter geometry. Incident light propagates along the z-axis*

the far field scattered intensity for unpolarized light of unit intensity is found by separation of variables to be

$$I_U = \frac{|S_1|^2 + |S_2|^2}{2k^2 d^2} = \frac{\lambda^2}{8\pi^2 d^2}\left(|S_1|^2 + |S_2|^2\right) \tag{2.19}$$

where the functions $|S_1|^2$ and $|S_2|^2$ are called the intensity functions. These consist of the two amplitude functions $S_1$ and $S_2$ given by

$$S_1 = \sum_{n=1}^{\infty} \frac{2n+1}{n(n+1)}\left[a_n \pi_n(\cos\theta) + b_n \tau_n(\cos\theta)\right] \tag{2.20}$$

$$S_2 = \sum_{n=1}^{\infty} \frac{2n+1}{n(n+1)} \left[ a_n \tau_n(\cos\theta) + b_n \pi_n(\cos\theta) \right]. \tag{2.21}$$

The angular dependent functions $\tau_n(x)$ and $\pi_n(x)$ are based on Legendre polynomials of the first kind, $P_n^{(1)}(x)$, and are defined as

$$\pi_n(\cos\theta) = \frac{P_n^{(1)}(\cos\theta)}{\sin\theta} \tag{2.22}$$

$$\tau_n(\cos\theta) = \frac{\mathrm{d}}{\mathrm{d}\theta} P_n^{(1)}(\cos\theta). \tag{2.23}$$

The so called scattering coefficients $a_n$ and $b_n$ from Eq. (2.20) and Eq. (2.21) are

$$a_n = \frac{\psi_n(\alpha)\psi_n'(\beta) - \widehat{n}\psi_n(\beta)\psi_n'(\alpha)}{\zeta_n(\alpha)\psi_n'(\beta) - \widehat{n}\psi_n(\beta)\zeta_n'(\alpha)} \tag{2.24}$$

$$b_n = \frac{\widehat{n}\psi_n(\alpha)\psi_n'(\beta) - \psi_n(\beta)\psi_n'(\alpha)}{\widehat{n}\zeta_n(\alpha)\psi_n'(\beta) - \psi_n(\beta)\zeta_n'(\alpha)} \tag{2.25}$$

here $\widehat{n}$ is the relative refractive index (and not the absolute value as mistakenly mentioned in [11]). The function $\zeta_n(x)$ is a linear combination of $\psi_n(x)$ and $\chi_n(x)$

$$\zeta_n(x) = \psi_n(x) + \imath\chi_n(x). \tag{2.26}$$

$\psi_n(x)$ and $\chi_n(x)$ are the Ricatti-Bessel functions given by

$$\psi_n(x) = \sqrt{\frac{\pi x}{2}} J_{n+1/2}(x) \tag{2.27}$$

$$\chi_n(x) = -\sqrt{\frac{\pi x}{2}} N_{n+1/2}(x) \tag{2.28}$$

where $J_{n+1/2}(x)$ and $N_{n+1/2}(x)$ are the Bessel and Neumann functions, respectively. In Eqs. (2.24) and (2.25) $\psi_n'(x)$ and $\zeta_n'(x)$ are the derivatives of $\psi_n(x)$ and $\zeta_n(x)$ with respect to $x$. $\alpha$ is our size parameter as already defined in Eq. (2.13)

$$\alpha = \frac{2\pi r_p}{\lambda_m}, \tag{2.29}$$

and $\beta$ is the second size parameter

$$\beta = \widehat{n}\alpha. \tag{2.30}$$

So even though the angular functions only depend on $\theta$ and the scattering coefficients only depend on $\alpha$ and $\widehat{n}$ they are multiplied in Eqs. (2.20) and (2.21) in such a way that it becomes very difficult to predict the effect of varying any one of the parameters.

#### 2.3.3.2 Plotting the Mie-solution

In order to extract the physical meaning from the Mie-solution we have to plot the results for various parameters. Instead of attempting to build my own set of algorithms I decided to use a free software "MiePlot v.4.0.01", developed and used by Philip Laven [14]. The software is available at www.philiplaven.com.

In all the following plots, the refractive index of the medium is set to $n_m = 1.333$ (water). The incident unpolarized light is a plane wave with a vacuum wavelength of $\lambda = 635$ nm, unless otherwise noted. Furthermore, all particles are regarded as non-absorbing, i.e., $n_p$ is real. A scattering angle of zero degrees corresponds to the same direction as the incident light, whereas a scattering angle of 180° corresponds to the direction towards the incident light.

The first parameter we shall examine is the refractive index of the particle. In Fig. 2.6 the scattering intensities of four particles with different refractive index are plotted. The numbers are based on the value of polystyrene ($n = 1.59$) [15] and increments of 0.1. All particles have a diameter of 1 $\mu$m and the incident wavelength is 635 nm.
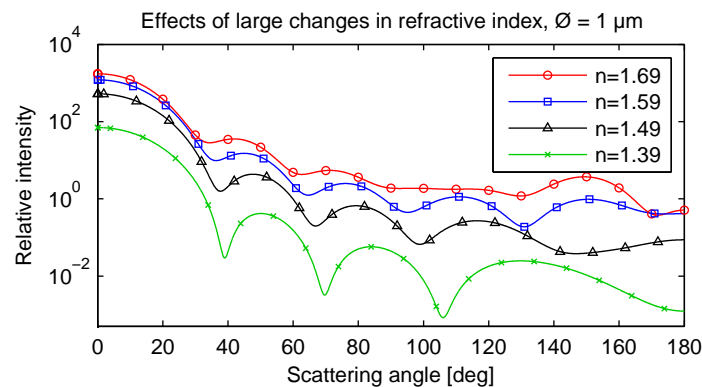


*Figure 2.6: This plot shows the correlation between large changes in the refractive index of the particle and the resulting scatter intensity. Calculated at $\lambda$=635 nm, $n_m$=1.333 and $\emptyset$=1 $\mu m$*

From Fig. 2.6 we clearly see that there is an overall tendency, the larger the refractive index is (compared to the media) the more light is scattered. This makes a lot of sence, as the particle can be considered a perturbation of the system characterized by its (relative) refractive index. It then seems reasonable to expect that the scattering effect induced by the perturbation becomes larger as the perturbation (relative refractive index) increases.

When dealing with refractive indexes in an experimental setting, it is often uncertain what the exact value is. This is due to changes in both temperature and atmospheric pressure, but also due to limitations in the purity of the given material. Hence, to convince ourselves that small changes in refractive index do not critically change the scattering intensity, the calculation was repeated for smaller changes (see Fig. 2.7).
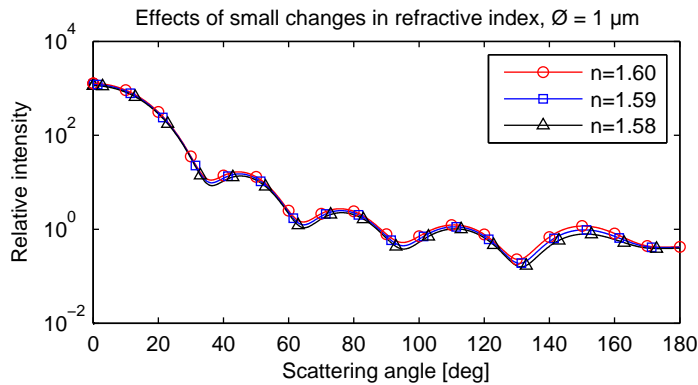
*Figure 2.7: This plot shows the correlation between small changes in the refractive index of the particle and the resulting scatter intensity. Calculated at $\lambda$=635 nm, $n_m$=1.333 and $\varnothing$=1 $\mu m$*

From Fig. 2.7 we see that the changes, induced by slight variations in the refractive index, are smooth and not critical.

The next parameter we look at is the incident wavelength. Here, specified as the vacuum wavelength, $\lambda_0$, and not as the wavelength in the medium, $\lambda_m$. The four wavelengths plotted in Fig. 2.8 correspond to an $Ar^+$(488 nm), doubled-Nd:YAG(532 nm), He-Ne (635 nm) and cheap red diode laser (680 nm), respectively. Actually, a He-Ne laser has a major emission line at 632.8 nm, but the laser mostly used in this work was 635 nm, hence that value is plotted.
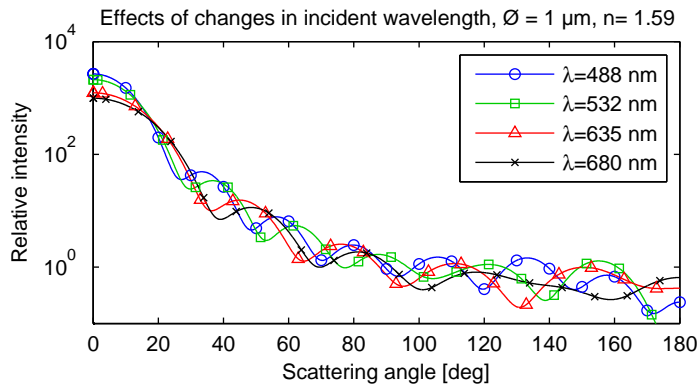


*Figure 2.8: This plot shows the correlation between changes in the incident wavelength and the resulting scatter intensity. Calculated at $n_p$=1.59, $n_m$=1.333 and $\varnothing$=1 $\mu m$*

Looking at the intensities in Fig. 2.8, it generally appears that a smaller wavelength results in a slightly increased scattered intensity. There are, however, certain angles ($\theta \approx 25°$ and $\theta \approx 50°$) where the longer wavelengths scatter more light. This result is potentially critical as it shows that there might be something to gain by choosing the optimal wavelength (which in most cases will be the shorter).

The third parameter we shall examine is the particle size (diameter). In Fig. 2.9 the three sizes mostly used in this work are plotted.
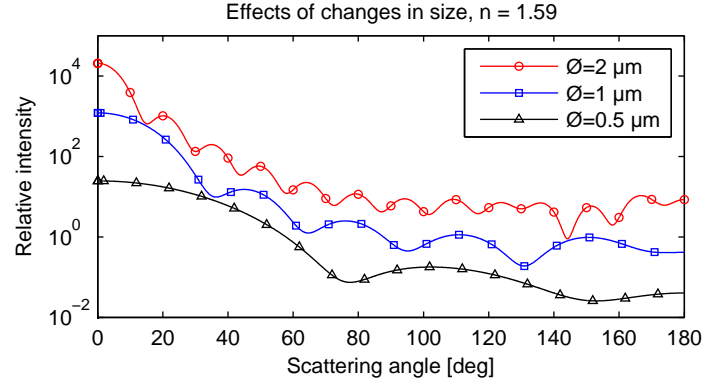


Figure 2.9: *This plot shows the correlation between changes in the particle size and the resulting scatter intensity. Calculated at $\lambda$=635 nm, $n_m$=1.333 and $n_p$=1.59*

It is very clear from Fig. 2.9 that the size of the particle is very strongly affecting the intensity of the scattered light. As in the case with the refractive index, the particle can be regarded as a perturbation of the system, but this time characterized by its size. Hence, it seems only logical that the scattered intensity increases with the size of the particle.

The next parameter of interest is the scattering angle $\theta$. In fact, through Figs. 2.6 - 2.9 we can already see that the intensity varies with the scattering angle. From these figures it is obvious that most light is scattered in the forward direction. Hence, when conducting an experiment where particles are detected by scattered light the optimal approach is to collect light from as small an angle as possible. However, from Fig. 2.9 it is clear that there exist several local minima along the curve. If a measurement is performed where the sampling of scattered light only covers very few degrees this should be taken into account. But if the sampling is done over a wider range of angles (as is the case for the work presented in this thesis) it is assumed safe within the first $\sim 50°$ to regard the intensity as monotonically decreasing with increasing scatter angle. To clearly illustrate the dependence of the scattering angle Fig. 2.10 shows the same plot as Fig. 2.9 but with a linear intensity scale rather than a logarithmic.
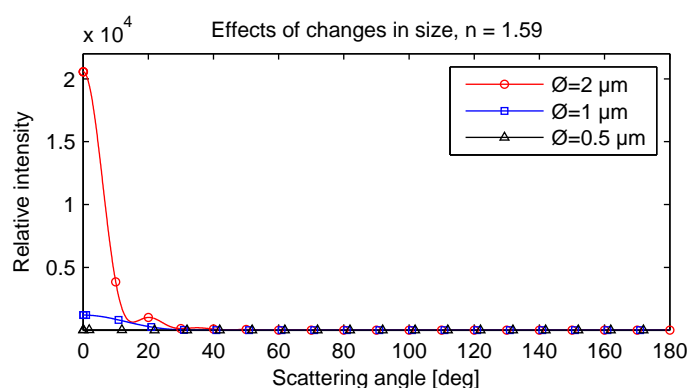
*Figure 2.10: This plot shows the correlation between changes in the particle size and the resulting scatter intensity. This linear plot clearly shows how the scattered intensity decays with increasing scattering angle. Calculated at $\lambda$=635 nm, $n_m$=1.333 and $n_p$=1.59. Notice this plot shows the same data as Fig. 2.9*

### 2.3.3.3   Concluding remarks on Mie-scattering

So, to wrap up on Mie-scattering the general conclusions are summarized below. It has been found that the intensity of Mie-scattered light depends on:

- The scattering angle. The smaller angle the scattered light is measured in, the higher the intensity. Almost all scattered light is found in the forward direction.

- The relative refractive index. The larger the difference in refractive index between medium and the particle the more light is scattered. This is also true when $n_p < n_m$.

- The size of the particles. Larger particles scatter more light than smaller particles.

- The wavelength of the incident light. Generally, Light at shorter wavelengths is scattered more than light at longer.

Finally to verify that the Mieplot software and the Mie solutions in general are correct, we note that the reached conclusions match with the results from [16, 17, 11] and a final plot is presented. The plot in Fig. 2.11 shows the scatter intensities for $\theta = 120° - 150°$ for the four wavelengths corresponding to blue (460 nm), green (520 nm) yellow (580 nm) and red (640 nm) light. The light is scattered by a 1000 $\mu$m sphere of water surrounded by air.
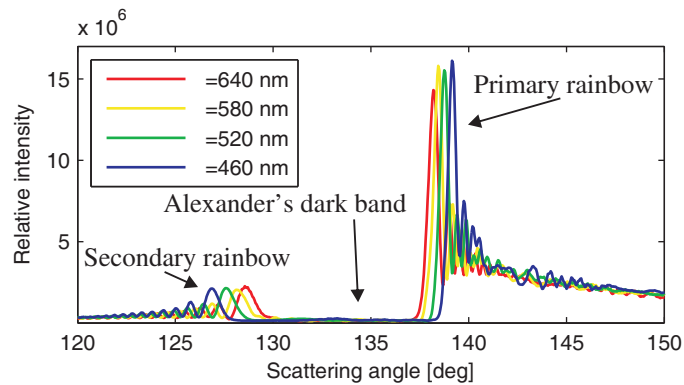
*Figure 2.11: This plot shows that it is possible to use the Mie-solutions to predict the angles of the colors in both the primary and secondary rainbow. Color reprint in Appendix C*

Fig. 2.11 explains the colors (and intensities) of both the primary and secondary rainbow. It also shows the dark band of Alexander between the two rainbows. The angles for the primary rainbow lie within a scattering angle region of $\theta = 138° - 140°$, which corresponds to the $40° - 42°$ stated by Descartes and Newton (measured from the center of the rainbow). As we have already discussed, the angular intensity distribution for the Mie-solution is dependent on the size of the particle. Hence, Mie-theory can be shown to prove that the angles of the rainbow are not completely fixed, but vary slightly with the drop size. This conclusion cannot be reached using only geometric scattering.

# Ray tracing

In Chapter 2 I discussed how it is possible to substitute a propagating electromagnetic wave with a ray, as long as the structures, in which the light propagates, are much larger that the wavelength. This gives us the possibility to use ray tracing software for analyzing the behavior of light within various structures. It is, however, important to be aware that there are two types of ray tracing software. One type servers the purpose of generating photo-realistic 3D images while the other kind, which we shall use, illustrates the path of individual rays through a structure. The software I chose to use during this work was "RAYTRACE" [18]. This software was selected because it is very intuitive to use, very flexible when it comes to designing structures, and it also supports scripting. Furthermore, it was recommended to me by an earlier Ph.D student S. M. Hagsäter [19], and I could inherit his software-license. When using RAYTRACE it is only possible to perform the simulations in two dimensions. This is indeed a limitation to the possible application of this software, but since we only consider structures, in this work, which are invariant in the $z$-direction (except for the cutoffs at the substrate and lid interfaces) and have nice vertical sidewalls it is sufficient to perform the simulations without the third dimension. This also means that the first fundamental law of geometrical optics (see Section 2.1.1) is fulfilled automatically, as everything is projected onto the same plane. The software then makes sure the two remaining laws are satisfied as well. Another limitation to the RAYTRACE software is the lacking implementation of the Fresnel equations [13, Chapter 2], which gives the ratio of the amplitude between a reflected and a refracted ray. Hence, in this program, all rays are assumed to carry the same intensity. This means we cannot allow one ray to be split into two when both reflection and refraction occur as this will increase the total energy. So, to avoid this issue we set the software to only reflect the rays if they are not refracted, or phrased differently from a waveguide point of view, we either have total internal reflection or the light is completely lost through refraction. This may at first seem like a harsh simplification, and in some cases it might be, but for the vast majority of simulations related to this work, the light is either guided within waveguides or hitting interfaces very close to the surface normal. In the case where rays propagate inside a SU-8 waveguide the critical angle is so small, that only rays going more sideways(propagating at angles larger than 45°) than forward, are not entirely reflected. For a straight 60 $\mu$m wide SU-8 waveguide a non-TIR ray will hit the side wall at least once every 50 $\mu$m or more than 100 times for a 5 mm long waveguide (typical length in this work). Hence, if

these rays loose just a small amount of their intensity each time they hit an interface they quickly attenuate. In the cases where rays intentionally cross interfaces between media, it will be at fairly low angles where the Fresnel equations simplify to

$$R = \left(\frac{n_1 - n_2}{n_1 + n_2}\right)^2, \qquad\qquad \theta_I \approx 0 \qquad\qquad (3.1a)$$

$$T = 1 - R = \frac{4n_1 n_2}{(n_1 + n_2)^2}, \qquad\qquad \theta_I \approx 0 \qquad\qquad (3.1b)$$

where $R$ and $T$ are the coefficients of reflection and transmission, respectively, and $n_1$ is the refractive index of the medium holding the incident ray. For an SU-8/air interface this gives an intensity transmission close to 95 % and for a SU-8/water interface it is above 99 %. So, there will be some minute reflections backtracking through the system, but these we ignore.

In the following sections I describe how the typical work flow has been during the various design phases of this project. First, I outline the work flow, and the associated problems, as this was prior to the development of the geometry-compiler "RayLab", and then explain how the work flow improved afterwards. I then describe how RayLab is structured and how it works. Finally, I present and discuss a few ray trace simulations.

## 3.1   Work flow

To perform a ray tracing simulation on a given geometry, the geometry must first be defined. This can be done in two ways: If the geometry of the structure is very simple the easiest approach is to draw it using the tools available in RAYTRACE; however, once the geometry begins to be slightly complex the tools for drawing quickly become inadequate and one should use scripting instead. Scripting is especially an advantage if we wish to track the effects of varying a single or a set of parameters. Since objects in RAYTRACE do not lock to each other, each one must be adjusted individually if scripting is not utilized. Even though the scripting language is well documented in the RAYTRACE manuals, it is very basic and therefore quite cumbersome to use. As an example hereof the following code calculates the semiminor axis of an ellipse (used as a lens) for a given eccentricity and semimajor axis.

```
                         RAYTRACE
1   .0.5
2   .=> ecc
3
4   .0.5
5   .=> semimajor
6
7   .ecc
8   .^2
9   .+/-
10  .+ 1
11  .sqrt
12  .* semimajor
13  .=> semiminor
```

Hence, it takes two lines to assign a value to a variable, and seven lines to solve the fairly simple equation $b = a\sqrt{1 - \varepsilon^2}$, as each mathematical operator must be applied individually line by line. As a consequence, the script files quickly become very long and difficult to read. However, once the script is completed it can easily be loaded and the geometry examined. If the design does not perform as expected, it is easy to go back to the script and adjust the concerning parameters (for example the eccentricity of an elliptic lens) and then reexamine the geometry.

Once satisfied with the geometry it needs to be converted into a mask suitable for photolithography. Since the geometry cannot be exported from RAYTRACE and L-Edit [20] (the software used for mask designing) does not support the RAYTRACE script-files, it was necessary to modify the scripts so that all important coordinates were listed on-screen. Using these coordinates it was then possible to reconstruct the geometry in L-Edit and order the final mask. This work flow is illustrated in Fig. 3.1.

Early work flow

- RAYTRACE Scripting
  huge time consumption
- RAYTRACE
  minor time consumption
- Extract coordinates
  minor time consumption
- Rebuilt using CAD
  big time consumption
- L-Edit
  minor time consumption
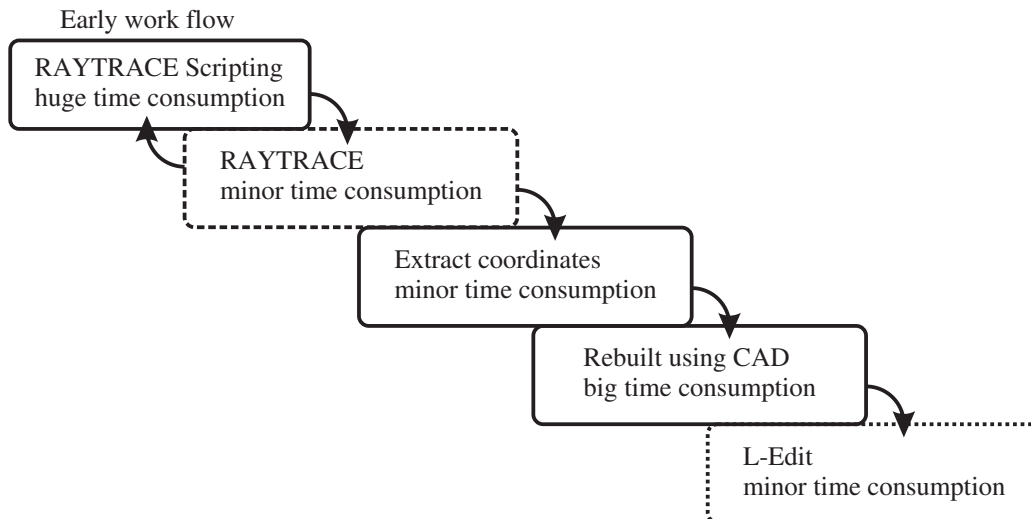
*Figure 3.1: This figure shows the early work flow in the chip design phase. The low level scripting language and the lack of possibilities to export the geometry made this process very tedious*

After completing the design of the first mask (2nd generation) it was obvious that this work flow was much too lengthy and complicated. I therefore got the idea to develop the program called "RayLab", that would make it possible to use the same script, or translations thereof, in both RAYTRACE and L-Edit.

With the development of this new software the work flow became greatly simplified. As I favor the MatLab-language including the COMSOL commands I decided to use that as the main scripting language. Hence, the design would be scripted as any two dimensional COMSOL geometry. The Matlab script was structured such that all the design coordinates were (this time automatically) saved in a text file. Loading the coordinate text file into RayLab would then automatically translate it into a script file for RAYTRACE and into a CAD command script. The geometry could then immediately be loaded and analysed

with RAYTRACE. Once the geometry was approved, the CAD script could be executed and saved as a DXF-file, which then could be imported to L-Edit. The final work flow is illustrated in Fig. 3.2.

Finalwork flow

Matlab/COMSOL scripting
big time consumption

RayLab
30 sec operation

RAYTRACE
minor time consumption

CAD - convertion
30 sec operation

L-Edit
minor time consumption
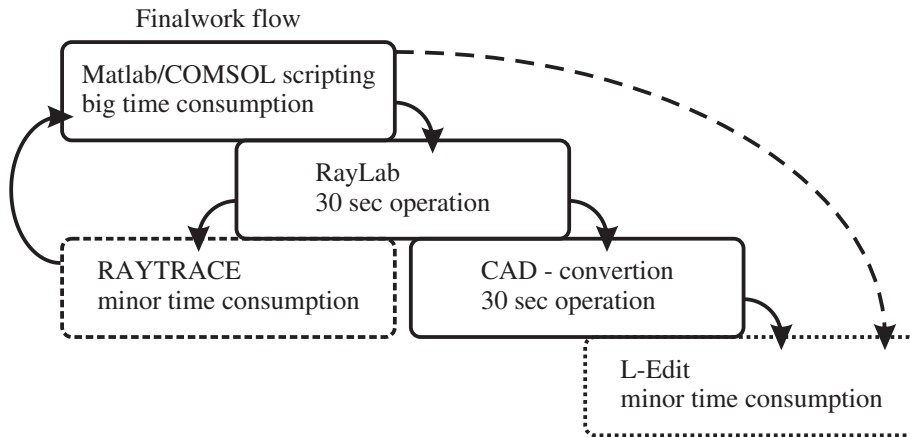
*Figure 3.2: This figure shows the final work flow in the chip design phase. With the development of RayLab the geometry scripting was moved from the RAYTRACE language to the much easier Matlab/Comsol language. This allowed the developed geometry to be immediately loaded into both RAYTRACE and L-Edit. The dashed line indicates a method discovered very late during this Ph.D period, that makes it possible to skip the CAD software step etirely*

When the two work flows are compared against each other, we find that in the initial scripting phase, the job is much easier and faster using the high level language of Matlab. Even though the scripting phase, is by far, the most time consuming step in both work flows, it is made a lot easier with Matlab, as regular plotting and mathematical functions can be utilized. The next step is to evaluate the geometry using RAYTRACE. Except for the need to first run the RayLab program, which only takes a few seconds to execute, this step is exactly the same for both work flows. The largest difference in these two approaches comes once the geometry is verified and must be transferred to L-Edit. In the early work flow, the transfer of the geometry would take almost as long as the initial scripting step, whereas the process of transferring the geometry is already completed by the RayLab program, thus performing the transfer in a few minutes.

Finally, it should be noted that very late in this project it was realized that it is possible to save the geometry in the DXF format directly from the Matlab/Comsol script, thus eliminating the need to include CAD software. The step going directly from script to L-Edit is marked with the dashed arrow in Fig. 3.2.

## 3.2 RayLab

RayLab is basically a text compiler. It takes one text file as input, and then basically translates each line into two other languages and finally saves the result as two new text files. The development of RayLab started early in 2008 and the program has been continually improved throughout the duration of the project. The purpose of RayLab is to significantly shorten the work flow of the chip design phase (see Section 3.1). Though it may seem bizarre to develop a text compiler in LabVIEW, I decided to do so for two reasons. The main reason LabVIEW was chosen was to improve my skills and knowledge regarding LabVIEW programming. At this point, I was already using LabVIEW in the laboratory to record data and I was already running into problems getting the program to behave as intended. The second reason to select LabVIEW was the ability to create a graphical user interface (GUI) in a very simple way. Finally, it was not expected that the program would require a lot of computational power, so finding the optimal language and code structure was not prioritized.

### 3.2.1 Matlab scripting

In order for RayLab to work, the input file must be formatted correctly. Hence, this puts some restraints on the way the script can be written. The RayLab input file is generated using the `diary()` command in Matlab, which saves everything written in the command window to a text file. It is therefore very important that only the necessary outputs are written in the command window and everything else is suppressed by terminating the lines with a semicolon (;). In general, there are only four functions that are allowed to express their output. These are `rect2()`, `ellip2()`, `circ2()` and `GetCoords()`. The three first functions are the standard two dimensional COMSOL geometry functions. When very simple structures are needed, these can be used. Since the output from these functions is very simple and contains all the necessary information about the object it can by used directly. The output from the line

```
--- Matlab/Comsol ---
1  r1=rect2(1000,2000,'base','corner','pos',[1000,-3000])
```

results in

```
--- Matlab command window ---
1  Rectangle solid object
2  lx: 1000.0
3  ly: 2000.0
4  p:  (1000.0,-3000.0)
5  base: corner
```

The functions `ellip2()` and `circ2()` provide a similar output.

However, when more advanced geometries are needed these functions are no longer sufficient. There are basically two ways of creating more complex objects, one is by combining simple shapes using the `geomcomp()` command, the other is to define a polygon as an array of curves using `curve2()` and `geomcoerce()`. It is also possible to combine the two methods. It is very important that the created objects are combined rather than

**25**

just overlap each other. If overlapping structures with refractive indices $n_1$ and $n_2$ are loaded into RAYTRACE the resulting refractive index becomes

$$n_{1+2} = 1 + (n_1 - 1) + (n_2 - 1) \tag{3.2}$$

The RayLab-generated `GetCoords()` function is used to extract the coordinates from the complex objects. `GetCoords()` takes three arguments. The first is the object to be processed, the second is the number of points to put on each segment, and the last is the refractive index of the object. The number of points on each segment is only important if the segment is curved. All three arguments can be given as arrays to simultaneously process several objects. The output from `GetCoords()` basically consists of three lists. The first list contains the sequence of the polygon segment (which often is non-trivial), the second list contains all the x-values, while the third list contains the y-values.

Finally the printout of each geometry must be terminated by the line

```
 ──────────────── Matlab command window ────────────────
1 │ - - - - - - - E N D - - O F - - G E O M - - - - - - -
```

This line is automatically added when `GetCoords()` is used. The refractive index of each object can be specified on the last line prior to the termination-line or through the `GetCoords()` arguments. If no refractive index is specified, RayLab will insert a default value.

### 3.2.2 The graphical user interface

When the RayLab program is started the graphical user interface (GUI) will appear as depicted in Fig. 3.3. The GUI is divided into three columns. The left most column contains the `Load File`-button, the control for the default value of the refractive index, and the status indicators. The middle columns controls the type, position and orientation of the light source. The third column contains buttons to create the `GetCoords()`-script and some demonstration scripts. Finally, the box in the lower right corner warns the user of parameters that will cause either RayLab or RAYTRACE to fail.
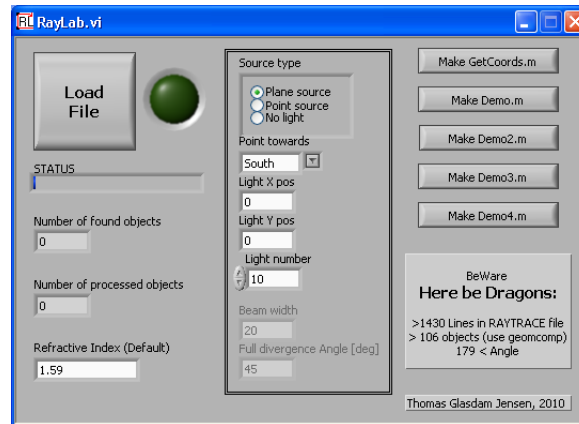
*Figure 3.3: This figure shows the graphical user interface of RayLab. The compilation is started by clicking the 'Load File'-button. The controls in the middle constitute an easy tool for adding a light source to the scene. Help-files in form of the 'GetCoords()'-script and Matlab code examples can be generated by the buttons on the right*

### 3.2.3   Output files

When RayLab has finished compiling the selected file the result is saved as two new files. The two new files are placed in the same directory as the input file, and they will have the same name except for the prefixes `RAY_` and `CAD_`. The file name extensions are `.RCS` and `.SCR`, respectively. Since all the mathematics behind generating the geometry is not transferred from the initial Matlab script to any of the output files it becomes rather difficult to change the geometry by editing the output files. It is, however, possible to edit the refractive index from the RAYTRACE script or to delete objects entirely, but the safest way to implement any changes, is to do this in the initial Matlab script.

A further description of the RayLab program is found in Appendix B

## 3.3   Ray tracing examples

When light is sent across the channel, the optimal shape it can take is as thin a plane as possible (with a normal parallel to the channel). Confining the light gives several advantages. One advantage is that the contrast of the scattered intensity will be higher. Secondly, the measured scatter angle will be much better defined. A thin light plane is, however, not easy to achieve, as it requires the light to be both collimated and to originate from a small source. If the light originates from an optical fiber the rays will diverge at various angles depending on the acceptance cone of the fiber and will therefore not be collimated. Once the light is coupled to the on-chip waveguides, we can use a few different tricks to improve the quality. One method is to add a lens to the end of the waveguide; this is, however, only efficient when the light is already sufficiently collimated. As shown in Fig. 3.4, light hitting a lens at two different angles will not share the focal point.
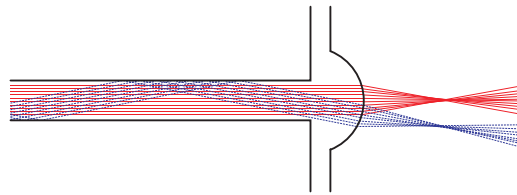
*Figure 3.4: When light propagates with different angles a single circular lens cannot bring all rays to a common focal point*

So, in order to benefit from lenses we must first improve the collimation of the light. A simple method to improve the collimation is to taper the waveguide. By tapering the waveguide the propagation angle of the rays is altered every time they hit the sides of the waveguide. This way, the least collimated rays are effected most. In Fig. 3.5, the effect of three differently tapered waveguides is illustrated. In all three examples the waveguide carrying the incident light is 1 cm long and subjected to identical light sources. At the input end, all three waveguides are 60 $\mu$m wide. In the examples depicted in Fig. 3.5 the waveguides are tapered to half the width, not tapered, and tapered to double the width, respectively.
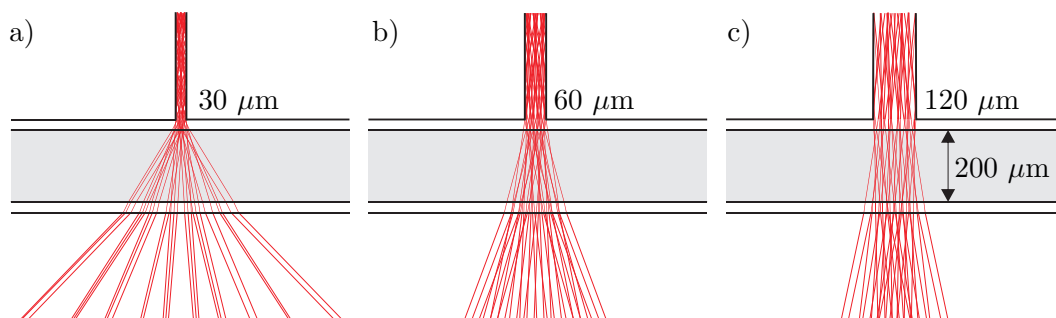


*Figure 3.5: This figure illustrates the effects of using tapered waveguides. All waveguides are 1 cm long and 60 $\mu$m wide in the top, they are all subjected to the same light source. The waveguide in panel a tapers in to only 30 $\mu$m resulting in a large increase in the divergence angle. The waveguide in panel b is not tapered. The waveguide in panel c tapers up to a width of 120 $\mu$m, giving a much more collimated light but also a very broad source*

By examining these three examples it is obvious that, when tapering the waveguide to a larger width, the light does become more collimated. It does, however, come at the cost of the resulting beam width, which severely increases. In the case depicted in Fig. 3.5a, the initial width of the beam is very thin, but due to the tapering of the waveguide the angle of divergence makes the beam broaden too much. Hence, we can conclude that tapering of the incident waveguide can only help us to either obtain a collimated beam or a very small source, but not at the same time.

One other way to achieve a smaller light source (seen from the channel) is simply to use a smaller waveguide. The size of the waveguide is, however, restricted by the size of the used optical fiber. The fiber that has been used throughout this project is the "FVP050055065" from Polymicro Technologies. This was the smallest available fiber, which had an outer diameter of approximately 65 $\mu$m. To physically be able to insert the fiber, the waveguide layer, and thereby also the waveguide had to be made 75 $\mu$m high. Hence, to maintain structural stability the width was kept to a minimum of 30 $\mu$m. So, it would be possible to just couple the fiber to the smaller waveguide, but since the core of the fiber is 50 $\mu$m in diameter a lot of power will be lost if using smaller waveguides. Another and smarter method is to couple the light to a 60 $\mu$m waveguide and then include splitters to achieve several smaller waveguides. Two examples of such splitters are shown in Fig. 3.6a and b. The efficiency of these structures is strongly related to the refractive index of the materials, as it requires a critical angle well below 45°.
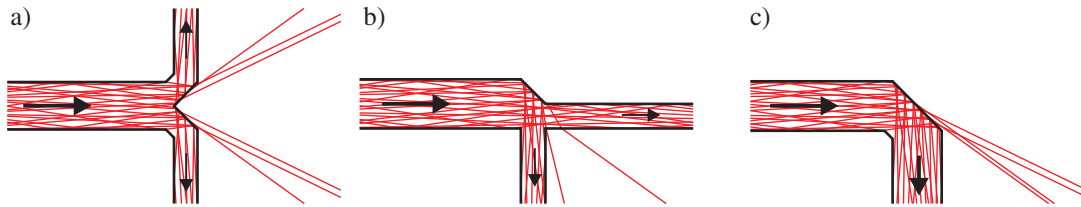


*Figure 3.6: This figure shows ray tracing simulations of three different SU-8 structures. Though all of these appear to be lossy, it is important to note that only the highly divergent light is lost*

The simulations in Fig. 3.6 show that for SU-8/air waveguides both split and bend structures do result in some loss. This loss is, however, not a bad thing. It logically follows that most of the lost light is the least collimated light. Also, by remembering that these simulation show a ray as totally refracted even though in reality it will be partially reflected, the loss of power is less than it appears. The same thing goes for the sharp 90° bend shown in Fig. 3.6c. Structures similar to this bend have been shown by Zauner *et al.* [21] to give losses of about 0.3 dB. Hence, by using these splitters and bends we can improve both the size of the source and the collimation of the light, at the expense of power. Should the lack of power eventually be a problem, there is noting to prevent us from just using a more powerful laser source.

# Microfluidics

Much in the same way as the description of electromagnetic waves can be simplified when they propagate in structures much larger than their characteristic length scale (wavelength), can the description of a fluid be simplified as well. Since a fluid consists of a (very) large number of individual molecules the characteristic length scale is in the order of 1 nm. Hence, when the fluidic structures under consideration are defined by much larger length scales it becomes reasonable to treat the fluid as a continuum, rather than treating the individual fluctuations at molecular level. The 'fluid particles' are assumed large enough to contain enough molecules, such that molecular fluctuations average out. In order to avoid specifying the volume of a 'fluid particle', fluid dynamics is usually described in terms of physical properties per volume, such as mass density, $\rho$, and force density, $\mathbf{f}$. According to [22] the characteristic length scale of a fluid consisting of 'fluid particles' is in the order of approximately 10 nm. Hence, for much larger fluidic systems ($\approx 10\,\mu$m) the continuum hypothesis is assumed valid.

A common approach when dealing with fluid dynamics is to adopt an Eulerian description rather than the Lagrangian description often used in classical mechanics. In the Lagrangian description each particle is traced such that a property is described as $\mathbf{v}(\mathbf{r}(t), t)$. In the Eulerian description one studies the properties at a specified position, such that the spacial coordinates are independent of time, $\mathbf{v}(\mathbf{r}, t)$. This description makes more sense in fluid dynamics, since the fluid particles are present everywhere (within the specified region).

When studying fluid dynamics, there are two particular important equations to evaluate. These are the 'Continuity equation' and the 'Navier-Stokes equation'. The two following sections describe these equations, and in the remainder of the chapter the two equations will be used to explain and evaluate various fluidic properties of the microfluidic structures used in this work.

## 4.1 Continuity equation

The first equation that governs fluid dynamics is the 'Continuity equation'. This equation is derived from the principle of mass conservation (we assume no relativistic effects occur). By looking at the mass inside an infinitesimal volume, it can be deduced that changes over

time to the volume integral of mass density must equal the negative surface integral of the mass flowing in and out of the volume. Hence, by using Gauss's theorem to change the surface integral into a volume integral, the continuity equation can be derived as

$$\partial_t \rho + \boldsymbol{\nabla} \cdot (\rho \mathbf{v}) = 0. \tag{4.1}$$

If the flow rate in the considered systems is much lower than the speed of sound in the liquid the fluid may be considered as incompressible. In this thesis, the maximum flow velocity is in the order of 0.1 m/s, whereas the speed of sound in water is approximately 1500 m/s [23]. This means that the mass density, $\rho$, is a constant and that Eq. (4.1) simplifies to

$$\boldsymbol{\nabla} \cdot \mathbf{v} = 0. \tag{4.2}$$

The consequence of this formula is that flow lines (or stream lines) may never cross nor touch each other. This argument will later be used to explain particle trajectories.

## 4.2  Navier-Stokes equation

The second equation that is important in fluid dynamics is the Navier-Stokes equation. Basically the Navier-Stokes equation is a rephrased version of Newton's second law of motion ($m\mathbf{a} = \sum_i \mathbf{F}_i$). As mentioned earlier, in fluid dynamics a physical property is often given per unit volume, hence ($\rho \mathbf{a} = \sum_i \mathbf{f}_i$), where $\mathbf{f}$ is the force density. However, since in fluid dynamics we use the Eulerian description, we notice that $\mathbf{a} \neq \partial_t \mathbf{v}$, instead we must use the material time-derivative, $D_t$ given by

$$D_t = \partial_t + (\mathbf{v} \cdot \boldsymbol{\nabla}). \tag{4.3}$$

Normally, we have to consider force density contributions due to viscous stress, pressure differences, hydrostatic pressure, gravity and external electric fields. In this thesis, we shall, however, only consider the contributions from pressure differences and viscosity, as the gravitational contribution is canceled by normal forces, and since we do not have any charges nor an external electric field (ignoring the detection beam) the electric term disappears as well. Hence, the Navier-Stokes equation for an incompressible fluid becomes

$$\rho D_t \mathbf{v} = \rho \left[ \partial_t + (\mathbf{v} \cdot \boldsymbol{\nabla}) \right] \mathbf{v} = -\boldsymbol{\nabla} p + \eta \nabla^2 \mathbf{v}, \tag{4.4}$$

where $\eta$ is the viscosity of the liquid. The Navier-Stokes equation is a non-linear 2nd order differential equation, and therefore very difficult to solve analytically, except for a few special cases.

The Navier-Stokes equation can be made dimensionless by introducing the characteristic length scale $L_0$ and velocity $V_0$ such that

$$\mathbf{r} = L_0 \underline{\mathbf{r}}, \quad \mathbf{v} = V_0 \underline{\mathbf{v}}, \quad t = \frac{L_0}{V_0} \underline{t} = T_0 \underline{t}, \quad p = \frac{\eta V_0}{L_0} \underline{p} = P_0 \underline{p} \tag{4.5}$$

where the underline indicates a dimensionless number. By inserting these four identities and collecting all dimension-carrying quantities on the left hand side the equation becomes

$$Re \left[ \underline{\partial}_t + (\underline{\mathbf{v}} \cdot \underline{\boldsymbol{\nabla}}) \right] \underline{\mathbf{v}} = -\underline{\boldsymbol{\nabla}} \underline{p} + \underline{\nabla}^2 \underline{\mathbf{v}}, \tag{4.6}$$

where $Re$ is the dimensionless 'Reynolds number' defined as

$$Re = \frac{\rho V_0 L_0}{\eta}.$$   (4.7)

Depending on the Reynolds number any given flow belongs to one of the following three flow domains

$$Re > 2000 \quad \Rightarrow \quad \text{Turbulent flow} \quad (4.8a)$$
$$Re < 2000 \quad \Rightarrow \quad \text{Laminar flow} \quad (4.8b)$$
$$Re \ll 1 \quad \Rightarrow \quad \text{Creeping flow} \quad (4.8c)$$

Due to the small dimensions turbulent flow is very rarely encountered in microfluidic systems. In cases where the flow is within the creeping domain the non-linear left hand side of the Navier-Stokes equation can be neglected. The laminar nature (depicted in Fig. 4.1) of both the laminar and the creeping domain is a very well known feature of microfluidic systems that we shall further investigate in Section 4.5.
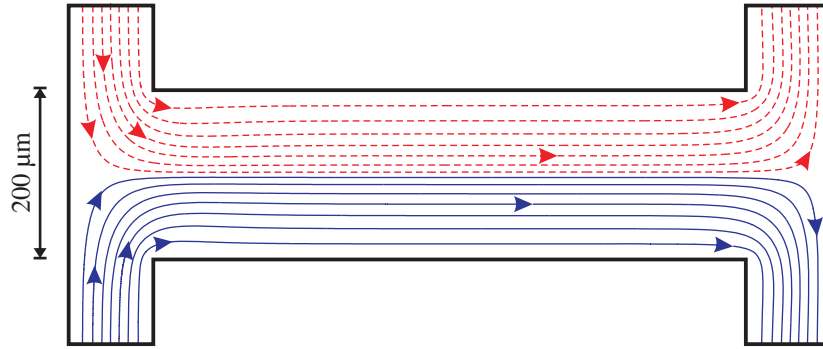


*Figure 4.1: This plot illustrates the nature of laminar flow. The plot shows the flow lines from an infinite plate simulation (2D). The Reynolds number is 36*

## 4.3   Pressure driven flow

There are several methods to drive a flow through a microfluidic system. Among these are electro-osmosis (which can be used to drive electrolytes), capillary action (which exploit the hydrophilic surface of certain materials) and systems, which are driven by centrifugal forces. However, the simplest and often used method is pressure driven flow. To obtain (and sustain) a pressure driven flow there must be a difference in pressure between the in- and outlet of the microsystem, often separated less than 5 cm. The most simple way to achieve this pressure difference is to introduce a height difference between the in- and outlet and then drive the chip using hydrostatic pressure. This is, however, rarely used in microfluidic systems as it often requires too large a height difference to be practical. Another simple solution is to use a syringe pump to inject liquid into the system at a specified flow rate. During this work, the vast majority of flows have been driven using

syringe pumps, so this is assumed unless otherwise noted. A laminar pressure driven flow is often called a Hagen-Poiseuille flow and have a characteristic parabola-shaped flow profile created by the 'no-slip' boundary condition. The no-slip condition is caused by the friction between the outermost fluid layer and the non-moving channel walls. The parabolic shape can be analytically derived for a translation invariant cylindrical channel or for an infinitely wide channel. The flow velocity for an infinitely wide channel (i.e. slit flow) is given by

$$v_x(z) = \frac{\Delta p}{2\eta L}(h - z)z, \qquad (4.9)$$

where $h$ is the height of the channel. The flow profile is illustrated in Fig. 4.2a. To compare this "un-physical" 2D solution to more physical 3D solutions, the flow profile, $v_x(z)$, is plotted (solid line) for three different channels widths. Figs. 4.2b-d correspond to channel widths of $w_b = 200$ $\mu$m, $w_c = 100$ $\mu$m and $w_d = 10$ $\mu$m, respectively. All channels are 100 $\mu$m high, and subjected to a pressure drop of 100 Pa over 1 mm. The fluid is water ($\eta = 0.001$ Pa s, $\rho = 1000$ kg/m$^{-3}$). The maximum flow velocity is found for the infinitely wide channel to be 12.5 cm/s (see Fig. 4.2a). The dotted line in panel b-d gives the 2D flow profile for easy comparison. To clearly illustrate the shape of the flow profile, the dashed line in panel d corresponds to the flow profile at 30 times higher pressure difference. From looking at panel d, it is obvious that we must be very careful when stating that pressure driven flows have parabolic flow profiles, as this is not the case for all directions in narrow channels.
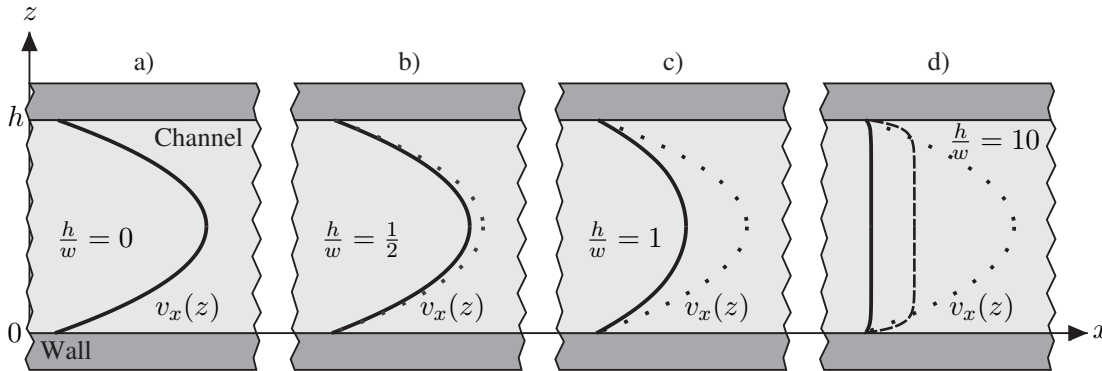


*Figure 4.2: Pressure driven flow profiles (see text for more details)*

Following [22] the analytical expression for the flow velocity in a rectangular channel is given by

$$v_x(y, z) = \frac{4\,h^2\Delta p}{\pi^3\eta L} \sum_{n,odd}^{\infty} \frac{1}{n^3}\left[1 - \frac{\cosh\left(n\pi\frac{y}{h}\right)}{\cosh\left(n\pi\frac{w}{2h}\right)}\right]\sin\left(n\pi\frac{z}{h}\right). \qquad (4.10)$$

However, when the system is driven using syringe pumps it is difficult to use this expression in practice, as the pressure difference ($\Delta p$) is unknown. So, to be able to calculate the velocity we utilize our knowledge of the total flow rate $Q$ (adjusted by the pump settings).

Following [22] Eq. (4.10) can be integrated over the channel cross section to give the flow rate. Hence,

$$Q = \frac{h^3 w \Delta p}{12 \eta L} \left[ 1 - \sum_{n,odd}^{\infty} \frac{192\,h}{n^5 \pi^5 w} \tanh\left( n\pi \frac{w}{2h} \right) \right]. \qquad (4.11)$$

By rearranging the terms we can calculate the unknown parameters as

$$\frac{\Delta p}{\eta L} = \frac{12\,Q}{h^3 w} \left[ 1 - \sum_{n,odd}^{\infty} \frac{192\,h}{n^5 \pi^5 w} \tanh\left( n\pi \frac{w}{2h} \right) \right]^{-1}. \qquad (4.12)$$

By inserting Eq. (4.12) into Eq. (4.10) we are now able to calculate the flow velocity inside our microfluidic system. It is very important to know the flow velocity in the main channel, as it tells how fast the suspended particles pass the detection region.

## 4.4   Lens extrusion effects

When designing the microfluidic flow cytometer, the fluidic influence of the focusing lens was subject to many considerations. In the original design (see Section 6.1.1), a single lens at the end of the incident waveguide extrudes into the channel. Such a perturbation of the channel wall must obviously influence the flow profile in the adjacent channel. In order to evaluate the influence of such perturbations a series of simulations was conducted using the commercially available finite-element software COMSOL. Since the shape of the lens does not vary along the z-axis (height of the channel), and since the lens is positioned sufficiently far from any other upstream features, we assume that its valid to only simulate the two-dimensional case. All the simulations are done at approximately $Re = 10$. In Figs. 4.3a-c, the results are shown for three different lens configurations. In panel a, the lens shape is added to the top channel wall. In panel b, a lens is also placed at the bottom wall in order to improve the collection of light. In panel c, both lenses have been pulled back so they line up with the channel wall. The background surface plot illustrates the y-component of the flow velocity, $v_y(x,y)$, at a given point. The color-scale is identical for all panels. The white horizontal lines are streamlines illustrating the direction of the flow. The fluctuation at both the in- and outlet are numerical artifacts caused by the boundary conditions and should just be neglected, as their effect dies out long before the lens effects start. In all three cases the inlet is to the left and the channels are all 140 $\mu$m wide (as this width was used for some of the 2. generation chips, see Section 6.1.2), and 1 mm long. All lenses are elliptic, 40 $\mu$m wide and extruding 14 $\mu$m out from the channel wall. According to the simulations, a maximum flow velocity of 0.128 m/s, 0.134 m/s and 0.126 m/s is obtained for the geometries in panel a, b and c, respectively. It does not come as a surprise to find the highest velocity in the most narrow channel, and the lowest velocity in the widest channel. But, what is surprising is that the maximum flow speed only increases by 6.8 % when the width of the channel is reduced by 20 %. If we look at the y-velocities, we find the maximum value of panel a, b and c to be -0.014 m/s,

±0.015 m/s and ±0.0045 m/s, respectively (ignoring the in- and outlet zones). Hence, it is obvious that geometry c results in the smallest disturbance of the flow.
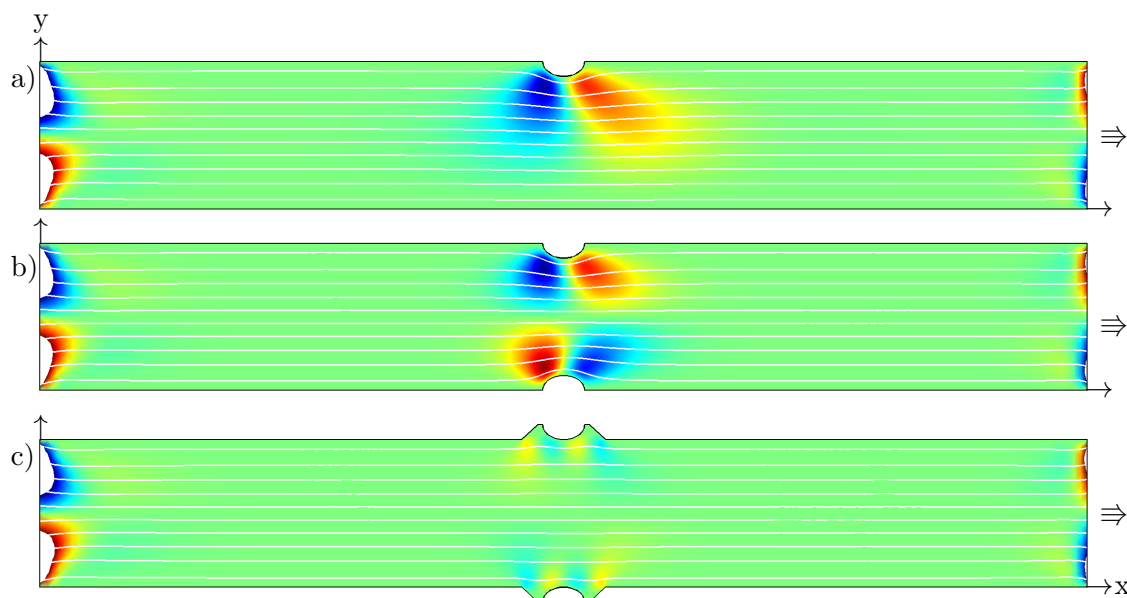


*Figure 4.3: Results of flow simulations with three different geometries. The white horizontal lines are streamlines illustrating the direction of the flow. The background surface plot shows the y-velocity amplitude. The channels are all 140 µm wide, while Re ≈ 10. The value fluctuations at the in- and outlets are numerical artifacts and should be neglected. The maximum plotted value of $v_y$ is ± 1.5 cm/s*

Since the positions of the particles no longer concern us once they have passed the detection beam, we only have to worry about the upstream effects of the lenses (towards the left side). The flow disturbance is, however, located very close to the lens structure, so it is very limited how much the particle trajectories (streamlines) are actually influenced. In the case of geometry a, the incoming beads will be pushed slightly closer to the channel wall opposite the lens. In the case of geometry b, the incoming particles will be pushed towards the center of the channel. In the last case c, the particles closes to the channel walls will wobble slightly. The particles closer to the channel center will hardly be affected.

If the Reynolds number is considerably increased, vortices will start to appear downstream of the extruded lenses and in the grooves next to the retracted lenses. But as we shall discuss in Section 4.5 below, we intend to make use of hydrodynamic flow focusing. This means that the part of the fluid that might get caught in the rolls will not contain any particles. Hence, we need not worry about the exact onset of the roll formation.

## 4.5   Hydrodynamic flow focusing

Given the two dimensional nature of the optical design, the detection beam is also focused in two dimensions. Hence, the width and therefore also the intensity of the beam will vary depending on which of the streamlines in Fig. 4.3 a particle follows. To avoid this from causing variations in the recorded data, the path of the particles has to be restricted to the middle part of the channel. This is done by exploiting the laminar flow to set up a double sided two dimensional hydrodynamic flow focusing (see Fig. 4.4). To achieve flow focusing, one or two secondary flows are pushed into the main channel. Because of the laminar flow the different streams will not mix together but propagate side by side. This technique is often used to manipulate the position of particles in microfluidics. If we assume that the suspended particles have the same density as the liquid and that the Reynolds number is sufficiently low, the particles will follow the streamlines. The density of the polystyrene particles used in this work is very close to that of water, just slightly larger. If suspended in a stationary water solution, 2 $\mu$m particles will sediment within a few hours and 1 $\mu$m particles will sediment within one or two days, while 500 nm particles stay suspended for several months, possibly because of Brownian motion. Furthermore, the Reynolds numbers are kept well below 10. Hence, we assume that the particles are not influenced by gravity and that they follow the streamlines fairly close. In Fig. 4.4, the three incoming flows are separated at the interfaces illustrated by the streamlines. Hence, any particles coming from the middle inlet will be restricted to approximately the middle third of the channel.
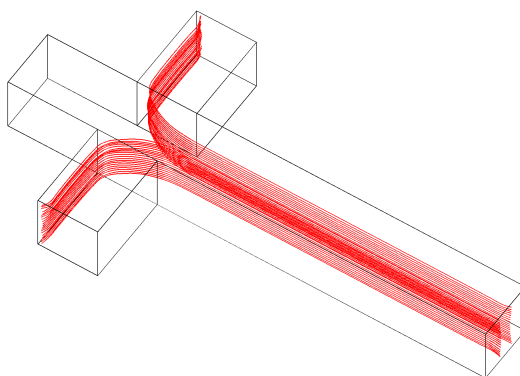


*Figure 4.4: This figure shows a flow simulation that illustrates how 2-D hydrodynamic flow focusing can confine the flow from the middle inlet to the center of the channel. The driving pressure is equal for all inlets. All channels measure 100 $\mu$m by 100 $\mu$m; Re = 11*

This type of flow is very easy to implement and was used for the first two chip generations (Section 6.1.1 and Section 6.1.2).

However, as earlier discussed, a pressure driven flow is subject to the no-slip boundary conditions. As a consequence, the particles flowing very close to the channel walls travel at much lower velocities than those in the center of the channel. Even with 2D focusing there are still particles near the top and bottom of the channel. This gives us several problems

when detecting and counting the particles. In order to be able to reliably detect and count the suspended particles they must pass the detection beam one by one. When the particles travel at different speeds there is a large chance that one particle will overtake another within the detection beam. A consequence of two particles passing the beam simultaneously could be that the resulting scattering intensity might appear as had we measured a single large particle passing. Hence, the event might be counted as one large particle rather than two small particles, leading to a incorrect result. Another problem with the high velocity dispersion is that two identical particles give rise to different measurement signatures if passing with different speeds. This is due to the fixed frequency of the data sampling that causes a slow particle to result in a wider peak than a fast particle. Even though the amplitude of the two detected peaks is the same, the difference in width can cause problems during the subsequent data treatment and cause one of the peaks to be falsely categorized. Furthermore, the optical system is optimized to collect light from the center of the channel, so particles passing at different positions will result in less intensive signals. To conclude, three dimensional focusing needs to be implemented to avoid these issues.
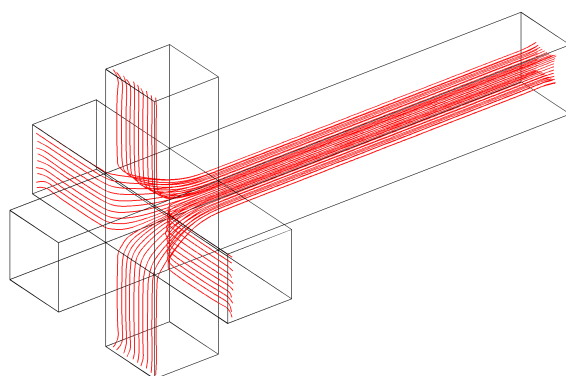


*Figure 4.5: This figure shows a flow simulation that illustrates how 3-D hydrodynamic flow focusing can confine the flow from the middle inlet to the center of the channel. The driving pressure is equal for all inlets. All channels measure 100 µm by 100 µm; Re = 12*

In Fig. 4.5, a flow simulation shows how the flow from the main inlet is confined to the center of the channel. This way, all particles are pushed away from the channel walls. To achieve three dimensional flow focusing, two additional channels are added to the two dimensional flow focusing configuration. Assuming the 2D focusing is performed in the horizontal plane, the two new channels are added in the vertical direction. In Fig. 4.5, the vertical channels are added to the same part of the main channel as the horizontal ones. This is not strictly necessary. The order of the channels and their relative position can be arbitrarily chosen. While the channel layout in Fig. 4.5 is simple and efficient, it is very difficult to implement, as truly three dimensional microfluidic systems are difficult to fabricate. Hence, from Section 6.2 and forth we shall use a two layered approach instead.

## 4.6   Stokes drag vs competing forces on particle

The final topic we shall briefly discuss in this chapter is the Stokes drag on the particles. The Stokes drag is the force a surrounding fluid exerts on a suspended particle due to friction. The drag force is given by [22]

$$\mathbf{F}_{drag} = 6\pi\eta r_p \mathbf{v} \tag{4.13}$$

where $\mathbf{v}$ is the relative velocity between the particle and the fluid. To grasp an idea of the order of magnitude of this force, we insert numbers typical for the systems in this thesis. Hence, $\eta = 10^{-3}$ Pa s, $r_p = 1$ $\mu$m and $|\mathbf{v}| = 0.01$ m/s results in $|\mathbf{F}_{drag}| = 200$ pN. This number is interesting because of the possibility that the optical intensity gradient will trap or push the particles as they pass the focused beam. According to [24], a typical trapping force, achieved in specialized [25] as well as in high-end commercial [26] optical trapping systems, is also in the order of 200 pN. However, these optical trapping systems use very powerful lasers, capable of delivering approximately 1 W to the specimen plane. Hence, as our laser output power is only 5 mW and the beam is only focused in two dimensions, it seems very unlikely that we will experience any problems related to optical trapping.

# DetectHIV

This Ph.D project has been a part of, and funded through, the EU-project DetectHIV (#037118). The DetectHIV project was supported by the Sixth Framework Programme and started in January 2007, while I started in May 2007. In addition to the initially planed three years, the project was approved for a half year extension, hence the project ended in June 2010. Throughout the duration of the project, meetings between all collaborators were held every sixth months to discuss achievements and plan the future strategy. Besides these biannual meetings, several technical meetings were held between project partners whenever a closer collaboration was required. Three of these technical meetings, and the outputs thereof, are further detailed later in this chapter.

I have chosen to include this chapter, as being part of the DetectHIV-project has had a great influence on the overall structure of my work. Being part of a larger collaboration meant that the work within certain topics, such as, fabrication technology and chip design had to be adapted.

This chapter starts with a brief overview of the intentions behind the DetectHIV project, including the various work packages and the responsible partners. I then discuss the three technical meetings and how they influenced my work. Finally, I will describe the assembling process of the prototype chips.

## 5.1 General concept

The overall intention of the DetectHIV project was to create a platform for early diagnosis of HIV. The goal was to achieve a device with a sensitivity one to two orders of magnitude higher and one order of magnitude faster than a standard ELISA test. This was to be achieved with a reasonably priced, desktop-sized instrument based on disposable microfluidic chips. This way the instrument itself would be small and cheap enough to have in every doctor's office, and through the disposable chips, each test would become cheap enough to be performed with regular intervals on healthy clients and make it feasible to continually test and monitor the effect of the treatment of an infected patient. Furthermore, the cheap disposable chip would make the device interesting to developing countries.

The main principle of the detection scheme is illustrated in Fig. 5.1. Magnetic particles,

coated with p24-antibodies, are retained by a magnetic field while the blood serum passes through them. If the HIV-specific p24-antigen is present in the serum it will bind to the antibodies on the magnetic particles, causing the particles to form doublets. The particles are then released and pass by an optical detector, which by means of scattering detects the amount of doublets and thereby the presence of the p24 antigen.
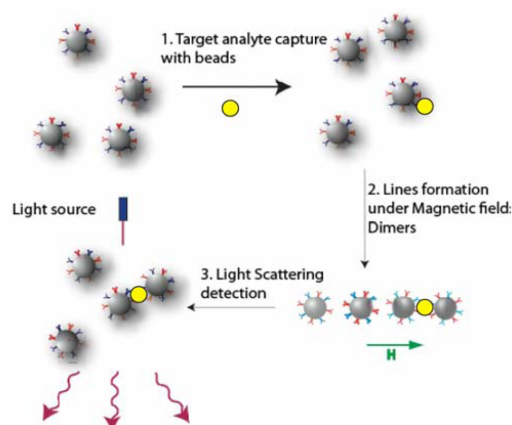


*Figure 5.1: Schematic diagram of how magnetic particles coated with p24 antibodies agglutinate under a magnetic field in the presence of the p24 antigen before being detected by scattered light. Figure obtained from the DetectHIV technical annex*

To lower the number of particles passing through the optical detector, an intermediate magnetic separation device was to be implemented to remove most of the singlet particles.

## 5.2   Work packages and partners

To achieve these goals the work load was distributed over several work packages, which in turn where distributed among the project partners. The distribution roughly took the following shape:

**Particles and assay conditions:**
The French company Ademtech and the group of Jérôme Bibette from ESPCI were responsible for the development and the initial testing of the magnetic particles, including the surface modifications and antibody protocols. The initial idea was to use 200-500 nm particles, and the main objective was to obtain a monodisperse particle population and avoid unspecific agglutination.

**Magnetic retention and separation:**
The group of Martin Gijs from EPFL in Switzerland was responsible for the development of the magnetic retention and separation modules. The goal here was to be able to catch the injected particles in a magnetic field, and hold them while washing the serum through, then release them while diverting the singlets and doublets into different channels.

**Optical detection module:**
The group of Jörg Kutter from DTU in Denmark was responsible for the development of the optical detection module. The goal of this module was to be able to detect and count the number of singlets compared to the number of doublets by means of scattered light.

**Instrument prototype:**
The French company Bertin Technologies was responsible for the development of the instrument prototype. Since the goal of the project was to conduct clinical tests, a user friendly instrument was required.

**Chip prototype:**
The development of the chip prototype was divided between the groups of EPFL, DTU, Bertin and ESPCI. The chip components were to be fabricated at Bertin, DTU and EPFL and assembled at DTU, then finally tested at ESPCI.

**Clinical tests:**
The group of Marc Van Ranst from KUL in Belgium was responsible of conducting the final clinical test using the prototype system. Unfortunately, the project never reached this state.

## 5.3   Technical meeting 1: Choice of technology

In November 2007, the first technical meeting involving my part of the project was held. The purpose of the meeting was to discuss the different fabrication technologies used to make the magnetic and optical modules. As it was planned to implement all three modules (retention, separation and detection) in the same chip, it was necessary to use, if not identical, then at least compatible fabrication processes.

At the time of the meeting the three modules were all fabricated using different techniques (see Fig. 5.2). The magnetic retention system was made by spin coating a glass substrate with SU-8, and then patterning the SU-8 by photolithography and finally sealing the channels with a second layer of SU-8. The magnetic separation system was made on a glass and PDMS chip, where the recesses for channels and magnetic poles were made in the PDMS part using a mould with a SU-8 insert. The optical detection module, which at this state was in the 2nd generation, was made by spincoating SU-8 onto a silicon substrate, patterning by photolithography and sealing the channels by a PDMS layer.

Magnetic retention    Magnetic separation    Optical detection

☐ Glass    ▨ SU-8    ☐ PDMS    ■ Silicon
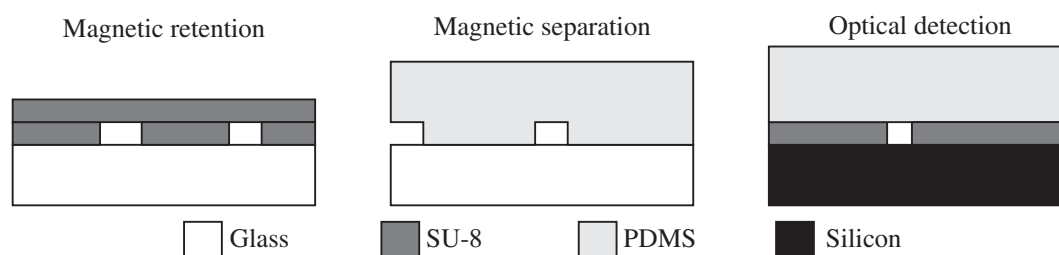
*Figure 5.2: This figure shows a sketch of the three fabrication technologies used prior to the first technology meeting. It was agreed that a layered glass/SU-8/PDMS structure would be a good compromise for all partners*

The first aspect that was discarded was the use of silicon as a substrate. In order to be able to inspect the chip with inverse microscopy it would be necessary to have a transparent substrate. Hence, we decided on glass as a substrate. Secondly, the required index steps for the waveguides made it necessary to abandon the double SU-8 layer approach, as we worried that it would become too tedious to fabricate. The same problem with missing index step would occur if we based the chips only on PDMS. We therefore decided to build the chips from three layers: glass, SU-8 and PDMS (n=1.46, n=1.59, n=1.4-1.45 respectively). This way both magnetic systems could be made with the already verified PDMS approach used for the separation system. It was assumed that the SU-8 would not introduce any problems nor issues, so the magnetic modules could simply keep using the PDMS approach. For the optical module, this change of technology meant we had to switch from using silicon as substrate and use glass instead. At the time this was assumed to only be a minor change; however, it would turn out that we ended up facing a lot of problems related to the adhesion of SU-8 to glass. The adhesion issue was eventually fixed by spin coating the glass substrates with AP300 (see Appendix A.1 for the fabrication protocol).

## 5.4   Technical meeting 2 - Operation protocol

The second technical meeting took place in October 2008. The purpose of this meeting was to establish an operation protocol for the combined chip modules. According to the plan of the DetectHIV project, the various modules were to be connected and tested during the third technical meeting, held two months later in December 2008. So, before the chip modules could be connected (and later integrated in the same chip) it was necessary to make sure that an operation protocol could be established. At this stage of the project, the system for magnetic separation was not working and its overall design was so uncertain that it was decided not to include the separation module in the integrated chip. The method used to operate the magnetic retention module was by pipetting particles into a reservoir and then pull them through the system using a syringe pump connected to the fluidic outlet of the module. The driving method used for the optical module (which at this point was in the 3rd generation) was to inject a solution of particles with a syringe

pump while focusing the flow with several other syringe based inlets. Hence, the main goal of this technical meeting was to figure out how these two methods could be combined. In principle both modules should be able to operate with both modes; however, there were a few complications. The method of driving the flow by suction was causing problems for the detection module, as the low pressure would drag air through the PDMS thereby disrupting the flow. The method of pipetting particles and (eventually) sample into a reservoir seemed to be a much better solution from an end user's view point, rather than injection from a syringe. So, in order to keep both methods it was suggested to proceed with a valve based solution that would allow us to initially operate the retention system by pulling, then switch the valves and operate the detection module by pushing. At this stage, it was uncertain if on-chip valves could easily be implemented. So, it was decided to use external commercially available valves for the December test, while we (the DTU group) was appointed to fabricate a simple pinch valve, which eventually could be integrated on chip.

### 5.4.1   Pinch valve

The basic idea behind the developed pinch valve is to exploit the elasticity of PDMS. Hence, by basically compressing the PDMS the underlying channels will collapse. By making the valve in PDMS it would be straightforward to implement it in the integrated chip as we had already decided on a PDMS top part. The basic operation of the valve is illustrated in Fig. 5.3. At the valve location a 2 mm deep recess with a diameter of 5 mm is made in the 3.2 mm thick PDMS, thereby leaving an approximately 1 mm thick membrane to cover the underlying channel. The membrane is actuated by a 4 mm blunt steel pin. The minimum diameter of these valves have not been characterized, the chosen diameter is simply based on the worry that too narrow a pin would puncture the PDMS rather than compress it. To achieve a better performance of the valve the channels should be placed in the PDMS layer rather than in the SU-8 layer. This way, the channel side walls will also be compressible.
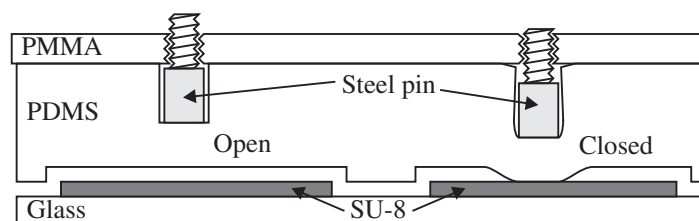


*Figure 5.3: This sketch illustrates the working principle of the pinch valve. By turning the screw, the steel pin deforms the PDMS membrane and closes the fluidic channel. Due to the elastic nature of the PDMS, the membrane returns to its original shape when the screw is loosened*

By adding a screw on top of the steel pin, the amount of compression could easily be controlled by the number of screw rotations.

The prototype of the pinch valve was fabricated by micromilling a mould from Poly[methyl methacrylate] (PMMA). The mould was made in three layers (see Fig. 5.4a). The lower part is pocketed to a depth of 200 $\mu$m exposing the negative channel structure. For this valve, a 3-way channel system was made with 200 $\mu$m wide channels. The middle part of the mould is simply a 3 mm thick frame. The top layer contains the three inlets and the corresponding O-ring cavities and holes in each corner to inject PDMS and let air escape. The top layer also contains a 5 mm hole for inserting a pin to create the recess above the membrane. The PDMS throughholes were made by inserting 1 mm steel pins. The three mould parts are fixed by six screws prior to filling. The final size of the valve-part measured 2 cm by 4 cm, including inlets.
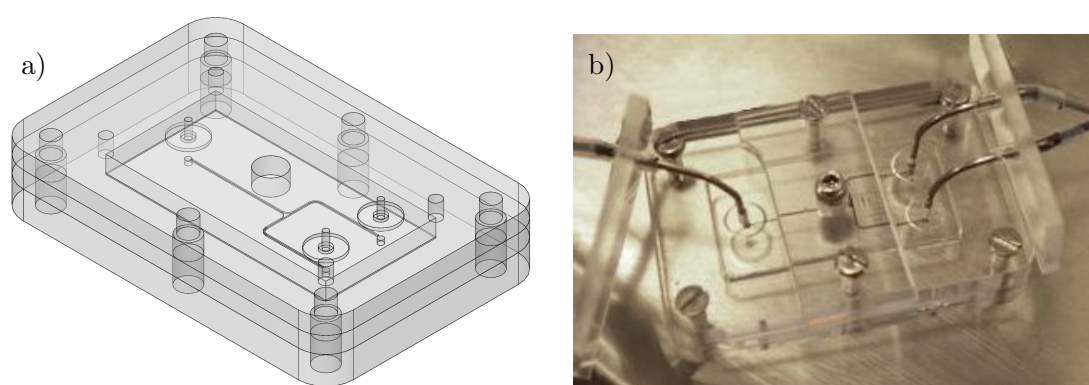


*Figure 5.4: Panel 'a' shows a 3D model of the PDMS mould. The mould consists of three layers. The lower part defines the channel extrusions and the upper part defines the O-rings. Panel 'b' shows a picture of the pinch valve prototype. The channels are filled with black ink for illustrative purposes*

The valve was tested by replacing the upper and lower part of the mould. The lower part was substituted with a completely flat part and the top part was replaced with a similar piece except for the removed O-ring recesses. Hence, the 3.2 mm thick PDMS part was compressed to 3 mm. Because of the O-rings, the PDMS is even more compressed around the in and outlets. An extra PMMA plate fitted with a M4 threaded hole to hold the screw for controlling the valve was mounted on the top plate (see Fig. 5.4b).

The pinch valve prototype was tested by injecting black ink, while visually observing if any ink could pass the closed valve. When increasing the pressure, it was found that the fluidic connections would fail before the valve. Furthermore, the performance of the valve seemed unchanged after numerous successive openings and closings. Hence, the quality of the valve was assumed sufficient, as the required on-chip pressure would be far less than during this test.

## 5.5   Technical meeting 3: The Integrated chip

The third technical meeting was held in December 2008. The purpose of this meeting was to connect and test the magnetic retention and the optical detection modules. This test would show whether the operation protocol from the previous meeting would work. Based on the experiences obtained from the conducted experiments, a preliminary design of the integrated chip was to be devised.

After getting rid of the initial difficulties related to combining and setting up the two modules, the test was successful. It was possible to inject particles into the magnetic module and catch them in the magnetic field and hold them while the volume representing the serum was pulled through. The external valves were then switched and the particles were sent to the optical module, where they were detected.

Even though this test was regarded as a success, there were several issues related to the combined setup. The long tubes, which were necessary to connect the two modules were very difficult to clear from bubbles, and the long flow path made it difficult to time the recording of the optical detection data. Also, air bubbles disrupted the 3D focusing. So, even though we did not manage to record the signal and hence count the particles, we could see from the live data display that the particles were passing the detector. As most of the problems were assumed to be related to the two modules being placed on separate chips, the test was regarded as a success.

This meant that it was possible, with the addition of valves, to operate the two modules using the combined push/pull operation protocol. Consequently, the design of the integrated chip could begin. The first thing to be decided was the overall size of the chip. By making the chip 6 cm by 2 cm it would give plenty of space on the chip, while three chips could be fitted on a single four inch wafer. It was decided from the start to separate the various components as much as possible while defining their connections very exactly. This way, the design becomes very flexible, as each component can be improved and redesigned without implicating the design and position of other components. By dividing the chip into 12 squares of 1 cm$^2$ the components were easily spread out as shown in Fig. 5.5.
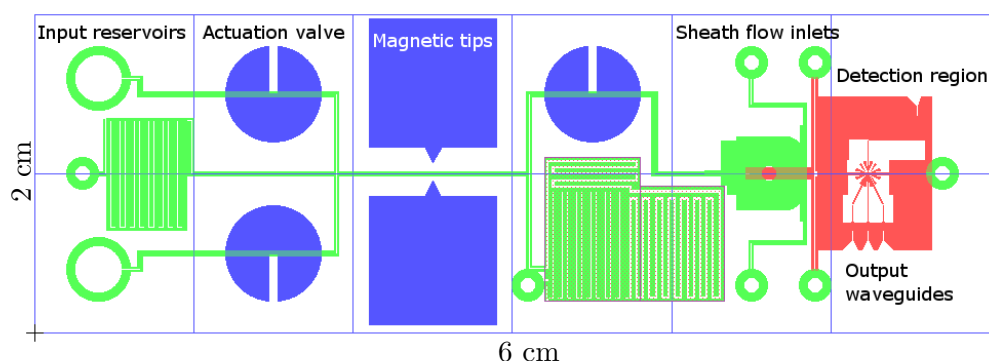
*Figure 5.5: This figure shows the layout of the integrated chip containing both the magnetic retention and the optical detection modules. The green structures represent the PDMS layer, while red represents structures in SU-8. The blue parts indicate the three pinch valves and the magnetic tips. Color reprint in Appendix C*

The components in the figure are divided into three categories. The components depicted in blue are external objects to be inserted later. It is, however, necessary to create recesses for them to fit inside. The green structures were to be created in the PDMS layer while the red structures were in SU-8. In fact, the entire chip is covered by SU-8, but only the structured part is shown. The 3rd generation of the optical module was initially inserted in the layout of the integrated chip, but the plan was to replace it later by an optimized version. The long meander channels in the PDMS are added to prevent contamination of the external syringes and tubing. The circular shaped green structures represent various inlets and outlets, the two bigger circles are the pipetting reservoirs. Together with the drawing in Fig. 5.5 a document was created stating the exact coordinates of the various components and the location of their connections. Based on the performance of the pinch valve prototype it was decided to include a total of three valves on the chip. On the final chip the PDMS channel would be even smaller ($\approx 100\,\mu$m) so they should collapse even more easily while the amount of displaced liquid also would be much less.

## 5.6   Assembly of the integrated chip

From the tests conducted during the December meeting it became clear that the alignment of the optical fibers was one of the least user friendly parts of the setup. Especially the input fiber was difficult to handle. As the upper right corner of the chip is only used by the optical detection module, it would be easy to implement changes made in the SU-8 structure. It was therefore decided that DTU would have until 1st of April 2009 to investigate if it would be a better solution to implement an incoupling lens rather than using an optical fiber. The deadline was necessary as Bertin had to delay the prototype design until it was clear which method to implement. It was finally decided to go for the lens based approach. The production of the various components could then begin. The final assembly of the integrated chips required six different components:

- The glass/SU-8 chip containing the optical module

- The PDMS part containing the magnetic retention systems and the pinch valve membranes

- The PMMA case, consisting of an upper and lower part

- Six bolt-spacer-nut sets

- Two magnetic tips

- Two optical fibers

After having tested the issues regarding the incoupling lenses, the latest design of the optical module (the 5th geneation) was adapted from its former 20 x 20 mm$^2$ to the 60 x 20 mm$^2$ of the integrated chip. To make the chip equally thick everywhere the entire chip was covered in SU-8, but only patterned in the right end. In Fig. 5.6 the finished glass/SU-8 chip is shown. The main channel intersection is seen in the center of the chip. The incoupling lens in located in the upper left corner (but cannot be seen in the figure).
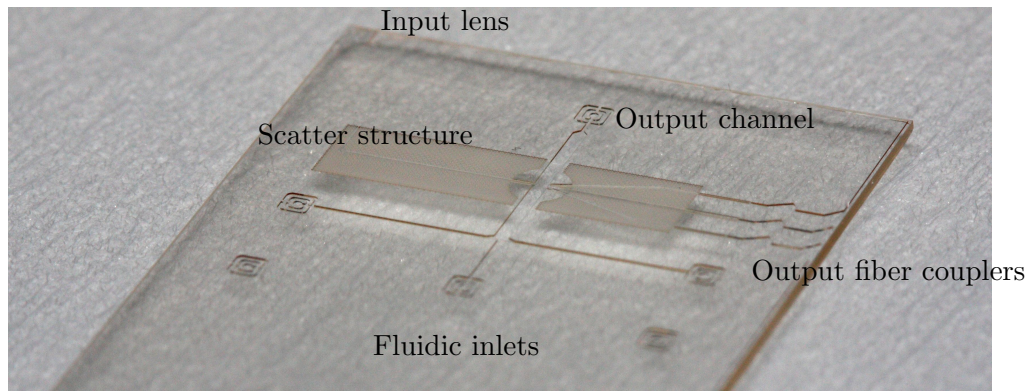


*Figure 5.6: The glass/SU-8 part of the integrated chip. The fiber couplers for the optical outlets can be seen in the right side of the picture*

The PDMS part was produced at EPFL. The PDMS was casted in a plastic mould. In order to obtain the very small channel structures and magnetic alignment grooves, a patterned silicon substrate was placed in the bottom of the mould. By patterning the silicon substrate using SU-8 it was possible to make features smaller than 50 $\mu$m in the PDMS cast. The PDMS part was made in two different versions, one including the meander shaped channels shown in Fig. 5.5 and one without it. The PDMS part shown in Fig. 5.7 is with the meander channel. The depicted part is facing upwards. Hence, the glass/SU-8 chip is to be placed on top of the PDMS part with the SU-8 facing the PDMS.
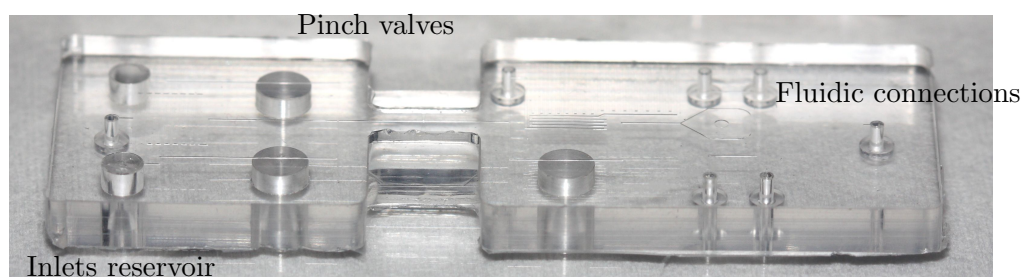
*Figure 5.7: A photo of a PDMS piece facing upside down. The three large circular features near the middle of the chip are the pinch valves. The two slightly smaller circular features near the left of the chip are the pipetting inlets for both beads and sample. The remaining holes are fluidic inlets*

The case was produced by Bertin. The case consisted of two parts; an upper and lower part. Both pieces were fabricated using micromilling. The case serves four purposes. Most importantly to apply even and constant pressure to the PDMS to ensure a proper and reproducible sealing of the chip. The second purpose of the case is to guide the alignment of the chip when placed into the instrument prototype so the incident laser beam actually hits the on-chip incoupling lens. The third task is to complement the fluidic connector so that all fluidic connections can be made simultaneously. Finally, the fourth purpose of the case is to protect the chip from rough handling. Even though the case offers very good protection, the magnetic tips and the optical fibers are extending outside of the case. Hence, the chip-in-a-case assembly must still be considered as very fragile. The empty case is shown in Fig. 5.8.



*Figure 5.8: The micromilled case is here shown without the chip inside. The metallic cylinders seen around each screw are the spacers. These spacers ensure that the PDMS is compressed in a very reproducible manner*

The upper and lower case is fixed in position with six bolts. By placing spacers, which are slightly thinner than the total glass/SU-8/PDMS chip, between the two parts the bolts

can easily be tightened to obtain the same compression for all chips. The metallic spacers can be seen in Fig. 5.8.

The magnetic tips were manually inserted into grooves in the bottom layer of the PDMS; thus, they were laying on top of the SU-8 in the same level as the PDMS channels. Even though the insertion of the tips was done by hand under a microscope, there were several issues that made it difficult. For one, the PDMS wall between the magnetic tip and the channel is only 40 $\mu$m wide, so it is very easily ruptured. Secondly, the process of sliding the tip along the PDMS is far from smooth as the PDMS sticks to the tips. Hence, the position of the magnetic tips is not always the same. In Fig. 5.9 the position of three sets of magnetic tips is shown. In all three cases the magnetic tip in the bottom of the picture is correctly positioned. However, only in the right picture is the position of the other tip correct as well. The position of the upper tip in the center picture is only slightly off, and this chip would possibly still be working. In the left picture the position of the upper tip is clearly far off.
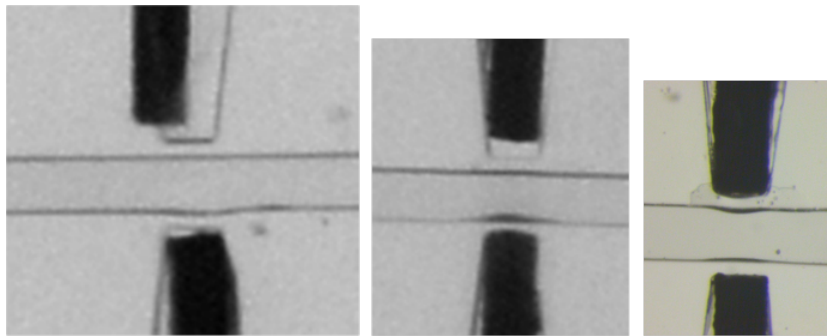


*Figure 5.9: This figure shows the position of three sets of magnetic tips. In all three cases the magnetic tip in the bottom of the picture is correctly positioned. However, only in the right picture is the position of the other tip correct as well. The position of the upper tip in the center picture is only slightly off, and this chip may still be working. In the left picture the position of the upper tip is clearly far off*

The final step of the assembly was to insert the two optical fibers. Though this step was not difficult (possibly due to years of practise) it was very time consuming as the fibers had to be polished before use and handled very carefully. Both the magnetic tips and the optical fibers were dipped in UV-glue (Norland Optical Adhesive 68) before insertion. After the position had been verified the glue was cured. Fig. 5.10 shows an optical fiber that has been fixed with glue. The fiber is inserted from the right and the SU-8 waveguide continues out to the left. The two menisci to the right side are formed by the surface tension of the glue.
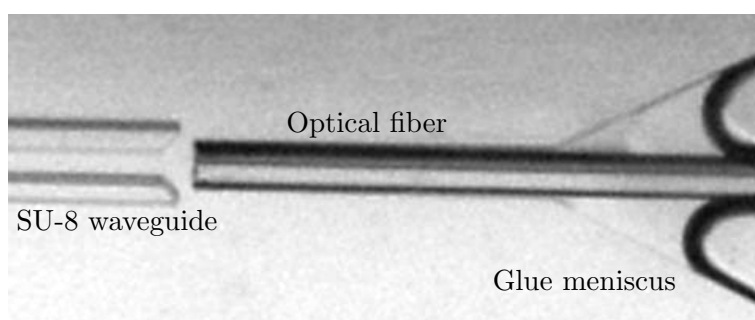
*Figure 5.10: This figure shows an optical fiber that has been fixed with UV-glue. The fiber is inserted from the right and the SU-8 waveguide continues out to the left. The two menisci to the right are formed by the glue. Notice the sharp interface change at the end of the fiber, this indicate the fiber is clean and well positioned*

After the final assembly, the integrated chips (see Fig. 5.11) were ready for the final quality check. To check if the chip was correctly assembled the positions of the magnetic tips and the optical fibers were verified under a microscope. Then the chip was placed in a specially fabricated optical setup to verify the alignment of the assembly and the quality of the fibers. The test was performed without liquid in the chip and the optical output from each fiber was recorded. The chips were then shipped to ESPCI in Paris for testing in the prototype.
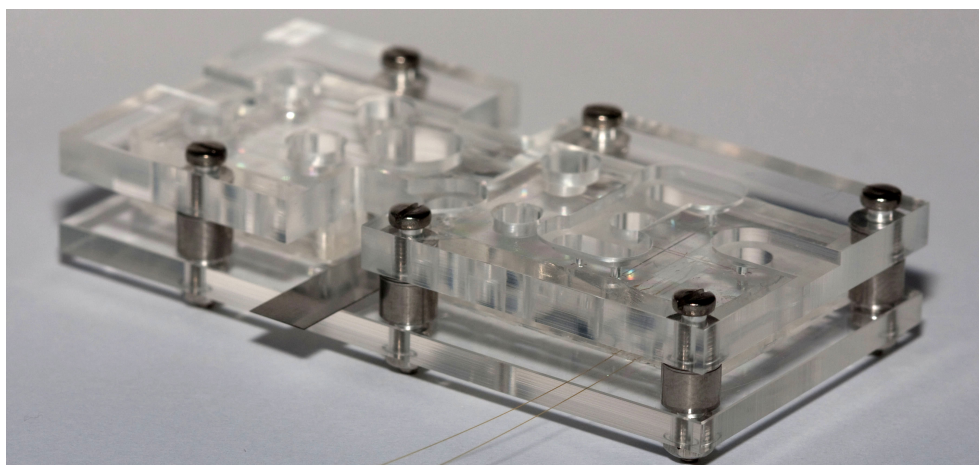


*Figure 5.11: A photo of the final integrated chip. Both the magnetic tips and the two optical fibers can be seen emerging from the case*

## 5.7   Final remarks

After the very first integrated chip had been assembled, it became clear that there was a mismatch between the PDMS and upper case components (see Fig. 5.12).
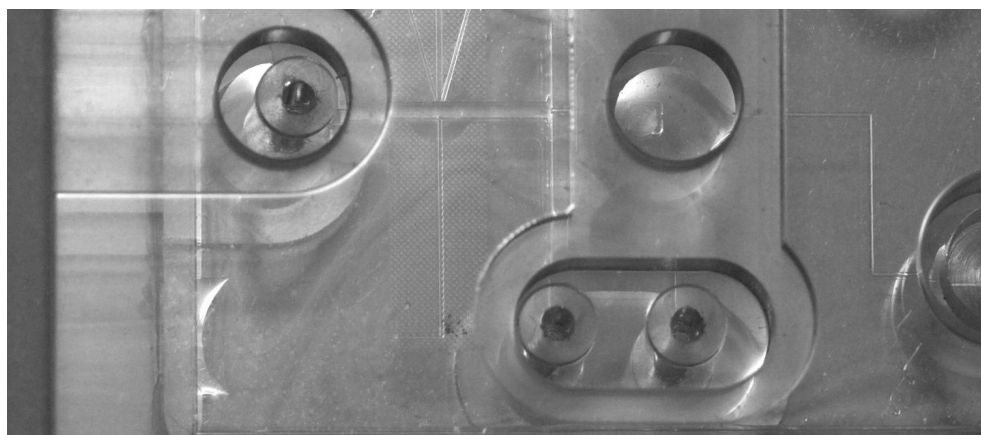
*Figure 5.12: A photo of the very first integrated chip. By careful examination it can be seen that the PDMS O-rings are not concentric with the holes in the upper PMMA case. Furthermore, one inlet is completely missing from the PDMS part. The incoupling lens is seen in the lower left corner*

The O-ring extrusions from the PDMS were not positioned at the correct location relative to the complementary PMMA holes or vice versa. Another issue was the fact that one of the inlets were missing from the PDMS part. As a result of this mismatch both the PMMA case and the PDMS mould had to be redesigned before any chips could be produced, hence resulting in a substantial delay. After rebuilding the components, no further issues were observed.

Because of the fragile optical fibers the packaging of the chips was very tricky, but by using double-sided tape to secure the fibers we managed to ship the chips from DTU to ESPCI without too many losses. Unfortunately, the optical quality measurements were poorly reproduced in the prototype setup. This indicates that either the alignment between the DTU setup and the prototype was not good enough, that the alignment of the chips was lost during shipment, or that the PMTs used were not performing equally well.

Due to the fabrication delay and several complications with the prototype setup, no real tests were achieved before reaching the project deadline. The two integrated modules were found able to retain and detect particles, but with rather poor quality, due to the retention only being sufficient at too low flow rates, and the bad alignment of the optical module.

The prototype setup is shown in Fig. 5.13
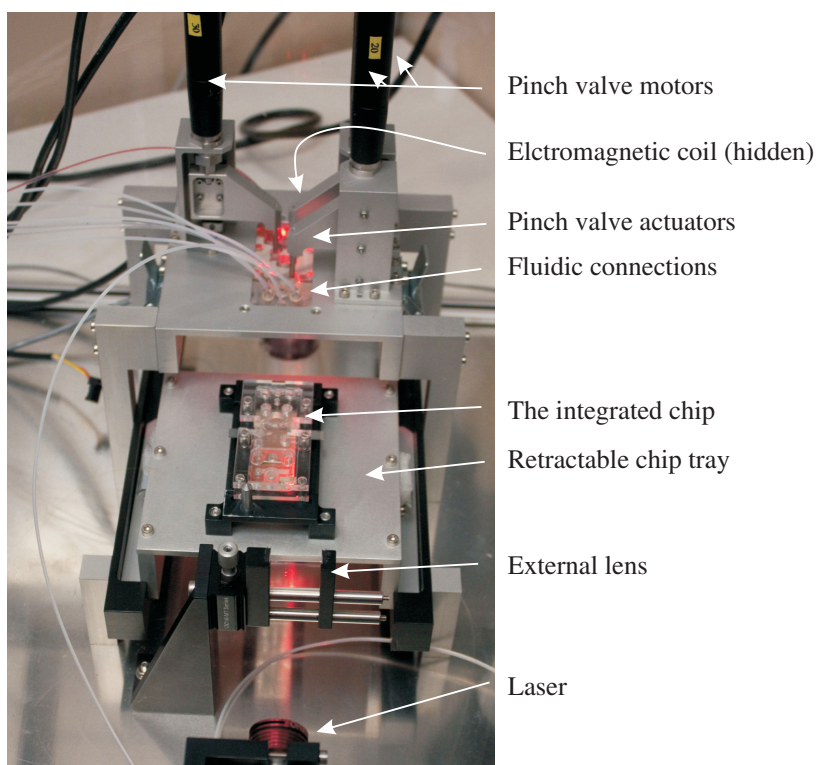
*Figure 5.13: A picture of the final DetectHIV prototype. The laser is seen in the bottom of the picture, pointing towards the external lens. The integrated chip is placed in the retractable tray. In the top of the picture the pinch valve motor are located.*

# Fiber Based devices

Before the DetectHIV project started, a former Ph.D student named Zhenyu Wang [27] did a successful on-chip cytometry experiment, where he managed to count particles at various sizes between 3 $\mu$m and 10 $\mu$m[28]. Based on his success the aim of my Ph.D project was to improve the method and push the detection limit towards sub-micrometer sized particles.

## 6.1 Preliminary experiments

### 6.1.1 1st Generation

When I joined the DetectHIV project in May 2007, it had already started. Guest researcher Santeri Tuomikoski had at this stage already obtained the photolithography mask used by Zhenyu Wang and had fabricated the first batch of chips. Since we were only able to obtain the masks and not the designs, we did not know the exact dimensions of these chips. The chips consisted of a 90 $\mu$m thick SU-8 layer on a silicon substrate. When I joined, the installation of the setup had only just started. The objective of this stage of the project was to attempt to recreate Zhenyu Wang's results, and then based on the obtained experiences we would create our own design and hopefully improve the results.

#### 6.1.1.1 Setup

The 1st generation of the setup can be divided into two parts; a fluidic and an optical one (see Fig. 6.1). The fluidic part consists of two syringe pumps (Harvard Apparatus, PHD 2000). One pump was fitted with a single syringe containing the particle solution, the other pump would hold two identical syringes, both containing 0.22 $\mu$m filtered water used to setup the two dimensional hydrodynamic focusing. The syringes were connected to the chip using a combination of teflon and silicone tubing. The fluidic output of the chip was collected in a an external waste reservoir.

The optical part of the setup started with a 5 mW laser diode (Coherent, 31-0144-000), from which red light, with a wavelength of 632 nm, was focused through a microscope objective. The light was focused at the end face of an optical fiber (Polymicro Technologies,

FVP050055065), which was slightly extending from a fiber alignment platform. The alignment was controlled by adjusting the x/y/z-stages under both the microscope objective and the fiber platform. Once the light was coupled to the fiber it could be guided to the chip. The optical output of the chip was collected in an optical fiber and guided into a photo multiplier tube (Hamamatsu, H5784-06). From the PMT, the signal was recorded on a computer and monitored on an oscilloscope. A sketch of the setup is shown in Fig. 6.1.
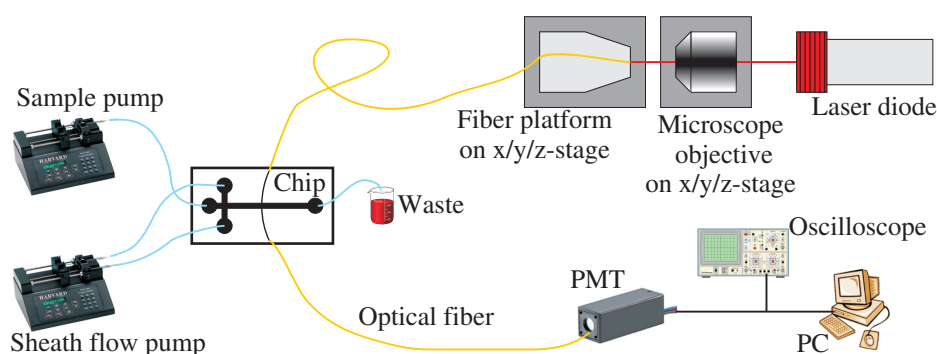


*Figure 6.1: A sketch of the first generation setup*

#### 6.1.1.2   Chip connections

The optical connections to the chip were made using the V-shaped grooves in the SU-8 layer at the ends of the waveguides. The chips were sealed by clamping a PDMS layer on top of the SU-8. The optical fibers were fixed between the PDMS and silicon substrate. The PDMS lid was made in a petri dish with a thickness of approximately 4.8 mm (the same as a M6 nut). The PDMS was then cut to fit the chip and throughholes were cut by pushing syringe needles through the PDMS. On top of the PDMS a PMMA substrate was placed. By tightening the black screws in Fig. 6.2 the PMMA would compress the PDMS and seal the chip. Steel tubes, made from the same syringe needles as used to make the PDMS holes were then inserted, through drilled holes in the PMMA, into the PDMS to act as fluidic connectors.
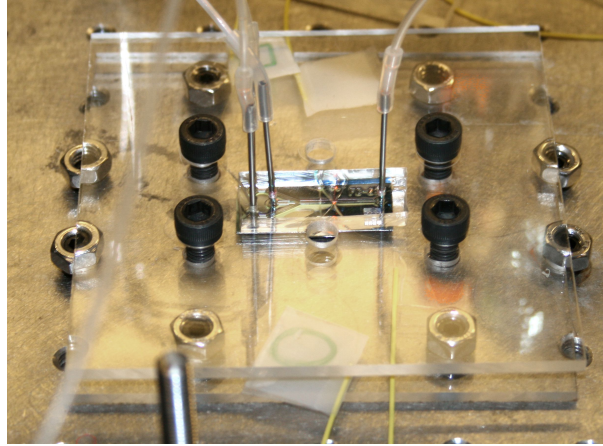
*Figure 6.2: The 1st generation chip located in its holder. Syringe needles are used to make fluidic connectors, and the optical fibers are covered with yellow sleeves. The four black screws are used to adjust the amount of pressure used to compress the PDMS. The eight M6 nuts are added to prevent deformation of the PMMA lid and a resulting uneven compression of the PDMS*

### 6.1.1.3  Structural issues

While testing the chips, two severe problems, related to the structural design of the chip, were encountered. In order to obtain a non-leaking seal between the SU-8 layer and the PDMS, a slight force has to be exerted on the PDMS. This would, however, often result in a collapse of the optical waveguides. Since the waveguides are much taller than wide, they tended to twist and collapse as shown in Fig. 6.3.
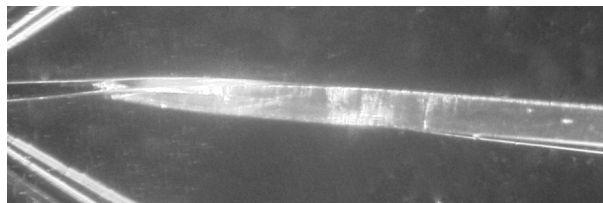


*Figure 6.3: An optical waveguide has collapsed due to the load on the PDMS. The load is necessary to avoid leakage between the SU-8 layer and the PDMS lid. The increased loss or total destruction of the twisted waveguide made many of the chips useless*

The twisting of the waveguides was very difficult to avoid as they were about 1 cm long and did not have any surrounding structures to help carry the load from the PDMS. As a result of the twisting, the waveguides exhibited very high losses or broke completely. This rendered most of the chips useless.

The second problem, which was encountered with these chips, was also related to the compression of the PDMS. When a force was applied to the PDMS it would compress in the regions where the chip was covered by SU-8 (channel walls, waveguide, etc.). But, in

the areas which are not covered by SU-8, the PDMS would begin to bulge out. This is, of course, a logical consequence of the compression, but when the bulging occurs inside the main fluidic channel it becomes problematic. The main chip described in the work of Zhenyu Wang was made in approximately 90 $\mu$m thick SU-8 and had a main channel which was 1 mm wide. This chip was reproduced and tested, but with a main channel more than 10 times wider than deep, the bulging of PDMS was found to have large implications on the performance. In many cases, the bulging PDMS would extend all the way down to the silicon substrate, thereby both blocking the flow and the laser beam. Even in cases where PDMS would not reach the bottom of the channel, it was still found to influence both light and flow patterns. With chips where the channel width was only about 100-200 $\mu$m this effect was much less pronounced and it was possible to run the tests.

### 6.1.1.4 Results

After switching to the chips with the smaller channel, it became possible to detect the presence of 5 $\mu$m particles. The data sample shown in Fig. 6.4 illustrates the typical performance of the chips with 100 $\mu$m wide channel. The data was collected at 10 kHz from a waveguide positioned such that light scattered around an angle of approximately 35° was collected.
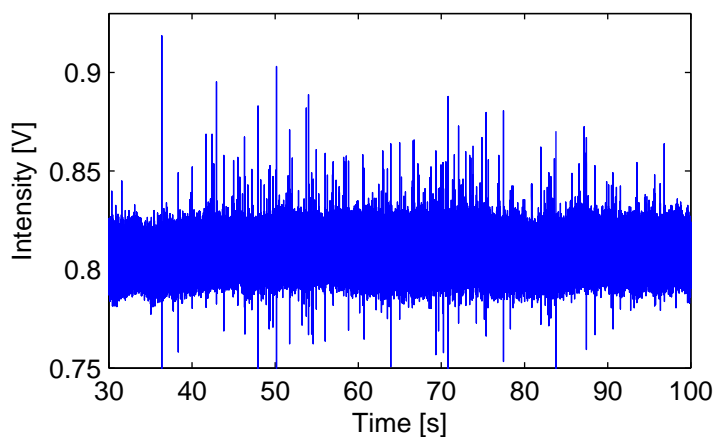


*Figure 6.4: This plot shows a typical data set obtained with a narrow channel chip. Though their presence is clearly detectable, the 5 $\mu$m particles cannot be accurately counted, due to the high noise level*

The data set presented in Fig. 6.4 shows that the presence of 5 $\mu$m polystyrene particles is easily detected. However, the low signal to noise ratio of approximately 2:1 makes it impossible to actually count the particles, as many peaks are lost in the noise.

### 6.1.1.5 Conclusions

Though it was not possible to recreate the results of Zhenyu Wang, 5 $\mu$m polystyrene particles were successfully detected and it was confirmed that the two dimensional flow fo-

cusing was working as anticipated. Based on the experience gained from these preliminary tests, it was concluded that, in order to prevent the PDMS from bulging into the fluidic channels, the width of the main channel would have to be closer to 100 $\mu$m than to 1 mm. It was also found necessary to put supporting SU-8 structures next to the waveguides in future designs to assist these in carrying the load from the PDMS lid, thus avoiding collapsing waveguides.

### 6.1.2   2nd Generation

The goal of the second generation chip was to fabricate and test a chip similar to the narrow channel (100 $\mu$m) 1st generation chip, but this time with a well defined design. The chips were again made in SU-8 on a silicon substrate and a PDMS lid was used to seal the channels. The second generation chip is shown in Fig. 6.5, the chip measures 30 mm by 16 mm.
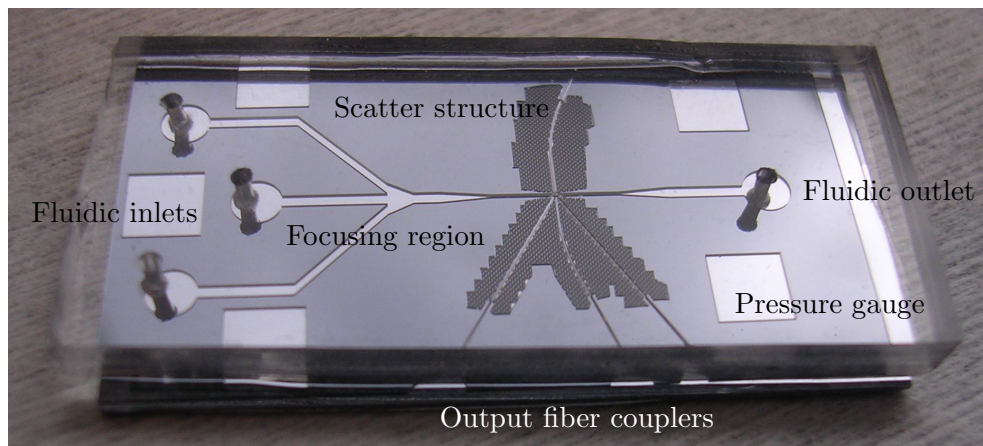


*Figure 6.5: This figure shows a photo of the second generation chip, including the PDMS lid. The chip measures 30 mm by 16 mm, with 20 mm from the center inlet to the outlet. On the chip, we clearly see the five square pressure gauges, the flow focusing intersection and the scatter structure surrounding the waveguides in the middle of the chip*

Since the outer diameter of the optical fiber available was roughly 65 $\mu$m, the thickness of the SU-8 layer was lowered from 90 $\mu$m to 75 $\mu$m, so that the waveguide-to-fiber coupling at the outputs would be more efficient (the fabrication procedure is described in Section A.1). By making the SU-8 layer 10 $\mu$m thicker than the fiber, it was possible to insert the fiber into the chip after the lid was positioned. By greatly expanding the outermost part of the fiber aligning V-grooves, thereby creating a Y-shaped groove, the bulging of the PDMS can be exploited to fix the optical fiber once pressure is applied to the lid. This way, the Y-grooves both serve to align the fiber to the waveguide but also to keep the fiber from moving or vibrating.

The five squares seen in Fig. 6.5 are areas without SU-8, or cavities between the PDMS and substrate. The squares measure 3 mm x 3 mm and are used as primitive pressure

sensors. Once the pressure is applied to the lid, the PDMS starts to bulge. When the bulging PDMS reaches the substrate in the middle of these areas there is a clear and distinctive color change. This way, the size of the contacting area can be seen as a local measure of the pressure on the PDMS. So by visually comparing the area of contact at the five different positions, an even pressure distribution could be obtained across the entire chip. Since the squares are by far the largest structures on the chip, the bulging effect will be much more pronounced here than anywhere else. Though the inlet and outlet holes with a diameter of 2 mm also suffer from the bulging, the effect can be neglected as long as the structures are not blocked.

#### 6.1.2.1 The scatter structure

To prevent the fibers from collapsing (as discussed in Section 6.1.1.3), all "unused" areas the of second generation chip were covered with SU-8. A gap of approximately 50 $\mu$m is kept at both sides of the waveguides. Covering the entire chip in SU-8 practically helps sealing the channels, as the channel walls in this case basically extend the entire width of the chip. Hence, dust particles, trapped between the PDMS lid and the channel wall, are less likely to lead to critical leaks. When looking at the chip in Fig. 6.5 a rough/darker surface is seen next to the optical waveguides. This is the scatter structure. The scatter structure consists of a pattern of I-shaped SU-8 pillars. The pattern is based on a unit cell design of 10 x 10 blocks. The design of the unit cell is shown in Fig. 6.6a.
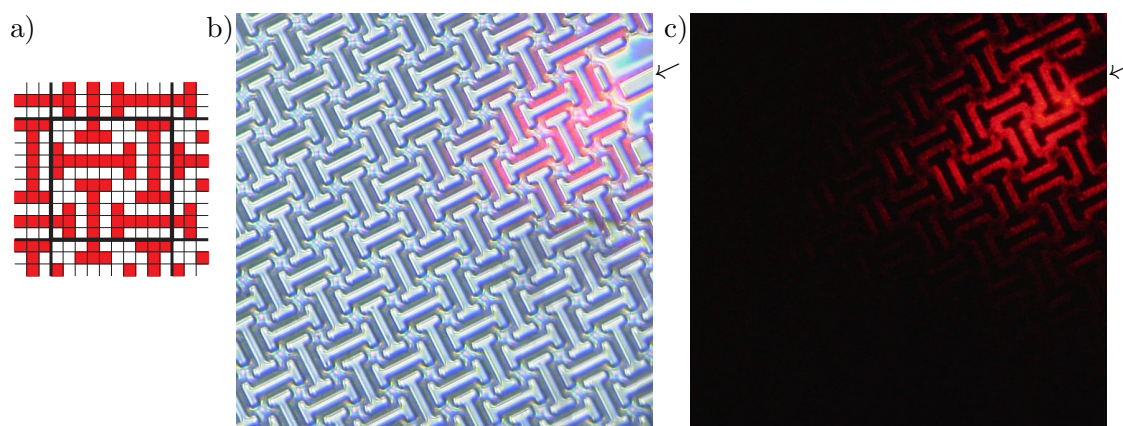


*Figure 6.6: Panel a shows the design of the scatter structure unit cell. The structure consists of alternating horizontal and vertical I-shaped SU-8 pillars. The unit cell measures 200 x 200 $\mu m^2$. Panels b and c show a microscope image of the scatter structure and the position of the test waveguide is indicated by the arrow. Each image measures 1 mm x 1 mm*

For the chips presented in this thesis the block length was set to 20 $\mu$m. The design is made in such a way that light propagating in any direction will pass through as many interfaces as possible. Since the fabricated interfaces are not optically perfect, a small portion of the light will be scattered out of the chip plane at each interface. Hence, the

scatter structure can be used to eliminate stray light. By adding this structure next to light sensitive areas of the chip, it is possible to prevent unwanted light from entering the area. Furthermore, the scatter structure also prevents lost light from for example the fiber to waveguide coupling region from reaching other parts of the chip. To illustrate the application of this structure a simple test chip was constructed. The test-chip was fabricated on the same wafer as the 2nd generation chip, hence the fabrication procedure was the same. The test-chip basically consists of a waveguide with a Y-groove at one end, and the other end leading into the middle of the scatter structure. Hence, this configuration exemplifies the worst possible loss of light that can occur in these chips (except for the laser pointing directly at the chip). In Fig. 6.6b and Fig. 6.6c, microscope images show the end of the waveguide on the test-chip. The position of the waveguide is indicated by the small arrow. These two figures each cover an area of 1 mm x 1 mm. By comparing the two images the penetration depth of the emitted light can be estimated to less than a millimeter.

### 6.1.2.2 Lens design

Since the design proposed by Zhenyu Wang [28] was discarded in favor of a design with a much smaller main channel, the design of the on-chip optics had to be re-done. To prevent the light from diverging when crossing the channel, an elliptic lens would still be added to the input waveguide. To collect the un-scattered light in the center output waveguide an elliptic lens was added here as well. In order to prevent the lens extrusions from interfering with the flow in the 140 $\mu$m wide channel (as discussed in Section 4.4), it was decided to retract the lenses into the channel wall. The two detection waveguides were placed at an forward scattering angle of 35°, which was chosen due to its similarity to the 1st generation chip. The dimensions of the optical components were found through ray trace simulations. The input waveguide was made 35 $\mu$m wide and the three output waveguides were 55 $\mu$m wide. The lenses were made only slightly elliptical, the input lens was made with a 24 $\mu$m semimajor axis and a 19 $\mu$m semiminor axis. The output lens was made a little bigger, with axes of 24 $\mu$m and 28 $\mu$m, respectively. In Fig. 6.7, the result of a ray trace simulation is compared to a microscope image of the actual chip. The only region in which the two slightly differ is very close to the output lens. Here, the actual beam seems to be better focused than predicted by the simulation. This is most likely due to the intensity profile of the light in the waveguide, which in the ray trace simulation is assumed evenly distributed over the selected angle range, where the light in reality probably has a more Gaussian shaped distribution. Hence, the simulation indicates a slightly higher intensity in those least collimated rays. Another source for the variation could be fabrication imperfections. The microscope image was obtained by filling the channel with dye, under normal operation the beam is not visible inside the channel.
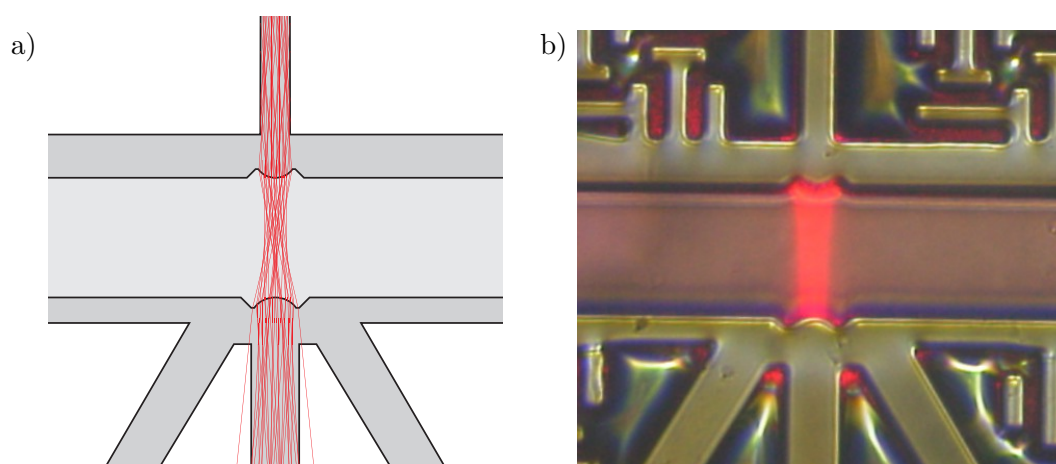
*Figure 6.7: This figure shows how the ray trace simulation in panel 'a' compares to the actual beam shape shown in panel b. The beam is made visible by filling the channel with dye. The slight difference is possibly due the to even intensity distribution used for the simulation, whereas a Gaussian distribution would have been more accurate. The scatter structure is seen in each of the corners of panel b*

### 6.1.2.3 Results

While testing the 2nd generation of chips, it became obvious that the concept of retracting the lenses into the channel walls was flawed. The probability of air bubbles getting stuck in the recesses next to the lenses was huge. These bubbles were found to severely interfere with the measurements, and therefore had to be removed or avoided. In order to decrease the level of random electrical noise in the measurements a low-pass filter was added to the setup between the PMT and the computer. With the combination of the new chip and setup improvements it was possible to push the detection limit down to 1 $\mu$m particles. The data sample shown in Fig. 6.8 shows an example of 1 $\mu$m polystyrene particles being detected using the upstream/right waveguide. The flow rate of both the sample and each sheath flow was 25 $\mu$L/hr. The data was acquired at 1 kHz after passing a 300 Hz low-pass filter. Though the presence of the particles could be detected, it was again very difficult to count them as the resulting peak heights would vary from a particle specific maximum value down to minimum value below the noise level, thereby making it impossible to separate them from the noise. This was the case for all particle sizes.
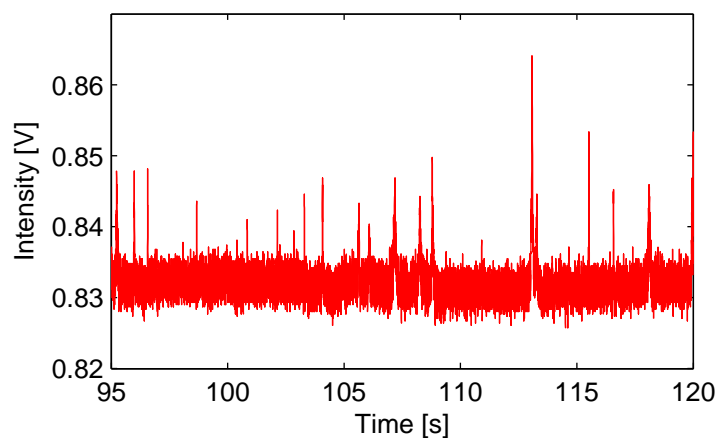
*Figure 6.8: This plot shows a sample of data recorded at 1 kHz after passing a 300 Hz low-pass filter. The presence of 1 µm particles is clearly detected, but difficult to count as the peak heights vary too much*

## 6.2   3rd Generation

Based on the preliminary results it was realized that three dimensional focusing would be necessary to accurately count particles. The work and results are explained in the article manuscript embedded below.

A revised version of this manuscript has been published (see List of Publications on page xix).

———————————— Start of manuscript ————————————

# Detection of Unlabeled Particles in the low Micrometer Size Range using Light Scattering and Hydrodynamic 3D Focusing in a Microfluidic System

Thomas G. Jensen, Guisheng Zhuang, Jörg P. Kutter*
These two authors contributed equally to this work.
*To whom correspondence should be addressed;

DTU Nanotech - Dept. of Micro and Nanotechnology, Technical University of Denmark (DTU), Buliding 345 east, DK-2800 Kgs. Lyngby, Denmark.

email: joerg.kutter@nanotech.dtu.dk
Fax: +45 4588 7762
Tel: +45 4525 6312

### 6.2.1  Abstract

In this paper, we describe a microfluidic device composed of integrated micro optical elements and a two-layer microchannel structure for highly sensitive light scattering detection of micro/submicrometer sized particles. In the two-layer microfluidic system, a sample flow stream is first constrained in the out-of-plane direction into a narrow sheet, and then focused in-plane into a small core region, obtaining on-chip three-dimensional (3D) hydrodynamic focusing. All the micro optical elements, including waveguides, micro lens, and fiber-to-waveguide couplers, and the in-plane focusing channels are fabricated in one SU-8 layer by standard photolithography. The channels for out-of-plane focusing are made in a polydimethylsiloxane (PDMS) layer by a single cast using a SU-8 master. Numerical and experimental results indicate that the device can realize 3D hydrodynamic focusing reliably over a wide range of Reynolds numbers (0.5<Re<20). Polystyrene particles of three sizes (2 $\mu$m, 1 $\mu$m, 0.5 $\mu$m) were measured in the microfluidic device demonstrating the feasibility of this approach to detect particles at or below 1m in diameter. To our knowledge, this is the first time unlabeled particles in the 1 $\mu$m range have been measured by on-chip light scattering detection.

### 6.2.2  Keywords

cytometry, light scattering, particles, hydrodynamic focusing, microfluidics.

### 6.2.3  Introduction

Flow cytometry is the registration and measurement of optical phenomena (fluorescence, scattering, absorption, etc.) occurring when particles flow past a laser beam. The resulting variations in the measured light intensities are then used to obtain information about the passing particles, most importantly size, but also type or viability, in cases where cells are concerned instead of particles.

Flow cytometry has shown to be a powerful tool for high-throughput characterization of particles and cells in genetics, clinical marker identification, biochemistry and developmental embryology [29, 30, 31, 32]. However, entities smaller than cells (such as bacteria, viruses or molecular assemblies) have great importance and widespread applications in medical diagnostics and therapeutics, and efforts are therefore underway to bring the power of cytometry also to this size domain [33, 34].

Rapid monitoring of size as well as counting of micro/nanoparticles could, for instance, be used to evaluate the functionality of ligands based on the agglomeration of particles with specific ligands immobilized onto the surface, thus rendering this technique a powerful tool for many future biomedical applications.

Commercial benchtop flow cytometers are large laboratory instruments operated by specially trained technicians. Even though these instruments have high performance and sensitivity [35] the associated price tag is often too high for research laboratories. To make the application of flow cytometry more practical, affordable and accessible, more miniaturization, automation, and reduction in production costs are necessary. Miniaturized flow cytometry using microfluidic principles provides an excellent detection platform

with reduced sample consumption and represents an inexpensive alternative for bioparticle sizing [36] and scattered light analysis [37]. Recently, with the help of microfabrication technology, flow cytometers have been miniaturized for bioparticle detection or cell sorting and quantification based on various techniques [38, 39, 40, 41, 42, 37, 43, 44]. However, because these and many similar systems depend on fluorescent detection (or other labeling approaches), they are limited to certain types of applications.

Label-free detection, such as using scattered light, is a more universal approach. The size of particles that can be detected by scattering is, however, currently limited to the micrometer range, typically around 20 $\mu$m down to about 3 $\mu$m [40, 28, 45, 46]. This is mainly due to the fact that the intensity of the scattered light dramatically diminishes with the particle size. Miniaturization, and the possibility to integrate several crucial functionalities on the same microchip, present a way to overcome the detection challenges and thus enable chip-based detection of particles in the lower micrometer range or even in the submicrometer range.

For accurate analysis of particles in a micro flow cytometer, two features are very important. Firstly, it is essential that there is a good flow focusing capability so that the particles will pass one after another through the detection region at almost the same position within the parabolic velocity profile, and thus, ideally, with identical velocities. This notwithstanding, traditional planar micro channel networks generally only provide a two-dimensional hydrodynamic focusing by an in-plane lateral compression of the sample stream from both sides. Cells or particles in the focused sample stream still experience a distribution in the out-of-plane direction. Clearly, there is great interest in developing a microfluidic device that is capable of focusing the sample stream in both, the in-plane and out-of- plane directions. Up to now, only very few 3D hydrodynamic focusing systems have been reported in the literature. Often, these approaches either require tedious fabrication processes [47], only work well within a limited Re range (<5), or focus the cells near one of the walls [48]. Recently, Mao et al.[49] developed a microfluidic drifting technique to enable 3D hydrodynamic focusing within a single-layer planar microfluidic device. While it is much easier to fabricate than previous designs, it only works well at rather high Re (>50).

Secondly, all the particles should pass through the same region of the detection beam if more than simple counting of passing particles is important (size, viability etc.). So far, most micro systems still use bulk optics for the optical measurements, but a trend towards more integrated micro optical systems has become evident in the past years. In micro optical systems planar optical waveguides and micro lenses are monolithically integrated with microfluidic channels to enable precise optical alignment [28, 50], in some cases even featuring configurable optics [51][52]. With both optical configurations (bulk optics or integrated optics) the detection beams are usually obtained from a laser and typically have a two-dimensional Gaussian intensity profile. Hence, particles passing in different flow paths will give rise to different scattering signatures. It is therefore essential that the 3D focusing confines all particles to a small path through the detection region where the laser intensity can be regarded uniform. In our group, micro optical elements have previously been integrated with microfluidic channels, both being defined on a single layer of SU-8 (photoresist) by UV photolithography [53].

In this paper, we present a microfluidic device with integrated micro optical elements and a novel two-layer micro channel structure for highly sensitive light scattering detection of particles in the lower micrometer size range. The simple two-layered micro channel structure enables a 3D hydrodynamic focusing, which is stable over a wide Re range (0.5-25). Waveguides with bends up to 90° and scattering structures (to suppress stray light) are integrated to make the chip compact and to improve the signal-to-noise ratio for the detected signals.

The chip presented in this paper is inspired by work published by Wang et al. [28]. Several modifications, such as 3D focusing, significantly smaller channel dimensions and a redesigned optical detection region have been implemented in order to reliably detect much smaller particles.

### 6.2.4   Experimental Sections

The sketch in Fig. 6.9 shows the design of the micro flow cytometer. The two critical regions are marked on the figure. These regions are the focusing region with a two-layer micro channel structure for 3D hydrodynamic focusing, and the optical detection region with waveguides, channel and a micro lens.
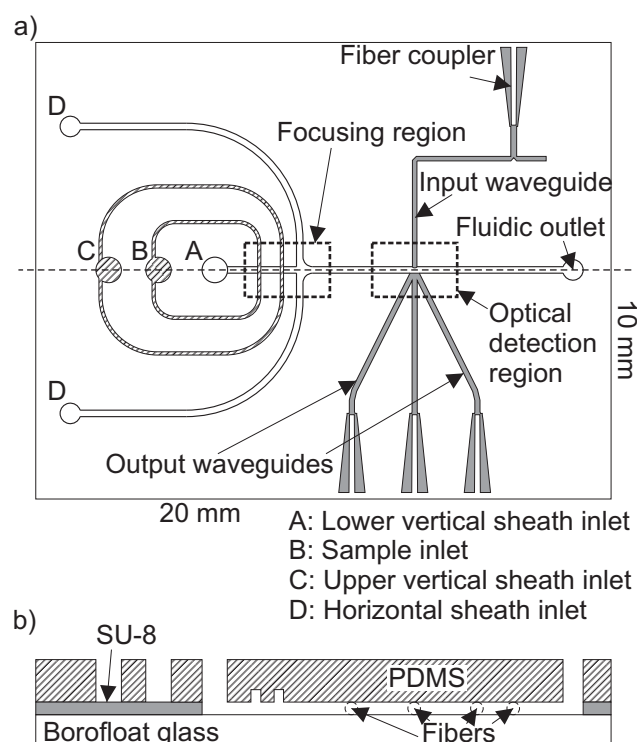
*Figure 6.9: a) Schematic diagram of the microchip flow cytometer with integrated micro optical elements and a two-layer microchannel structure. The SU-8 channels are shown in white containing the in-plane focusing channels and the main channel. The optical parts (also in the SU- 8 layer) are marked with gray. The hatched areas show the fluidic channels present in the PDMS layer. The dashed line going along the main channel indicates the position of the cross section shown in Fig. 6.9b. b) Cross section of the chip, showing the different layers (glass substrate, SU-8 and PDMS)*

The system is driven using two syringe pumps (Harvard Apparatus, PHD 2000). One pump, holding the syringe containing the sample, is connected to the sample inlet of the chip using 0.2 mm ID teflon tubing (Bola, s 1810-01). The second pump holds four syringes containing MilliQ-water used to set up the focusing flow. As the four syringes are all actuated by the same piston it is possible to vary the ratio between the focusing flows by changing the syringe diameter. In this work, we used 2x20 ml and 2x2 ml (B.Braun, Luer Lock Injekt, 4606736V and 4606701V) for the in-plane and the out-of-plane focusing, respectively. By using LabVIEW based pump control software the flow rate can easily be set.

### 6.2.4.1  Three-dimensional hydrodynamic focusing

Following on recently published work [54][55][56], we designed and fabricated a similar two-layer channel structure (consisting of PDMS and SU-8 on a glass substrate, see Fig. 6.9b) to

enable 3D hydrodynamic focusing, while, at the same time, allowing for the possibility to integrate micro optical elements. For rapid evaluation of the 3D focusing using fluorescent based confocal laser scanning microscopy, a non-auto-fluorescent PMMA prototype was fabricated using micromilling technology [57]. Since SU-8 is itself fluorescent it cannot be used for the flow evaluation measurements. Fig. 6.10 shows the details of the geometry of the proposed 3D focusing system and a concentration isosurface of the focused stream obtained by numerical simulation. Fig. 6.10a shows the schematic diagram of the 3D focusing system, where 'B' denotes the sample stream and 'A', 'C' and 'D' denote the focusing flows. Two smaller channels are fabricated in the upper layer (B and C, 200x200 $\mu m^2$) and two larger channels (A and D, 400x400 $\mu m^2$) are fabricated in the lower layer (the relatively large dimensions were imposed by the chosen prototyping fabrication method). Fig. 6.10b presents a COMSOL 3.4 finite element simulation for the proposed architecture indicating successful 3D focusing. The sample stream is first focused out-of-plane into a narrow sheet, and then shaped in-plane to a rectangular cross-section.
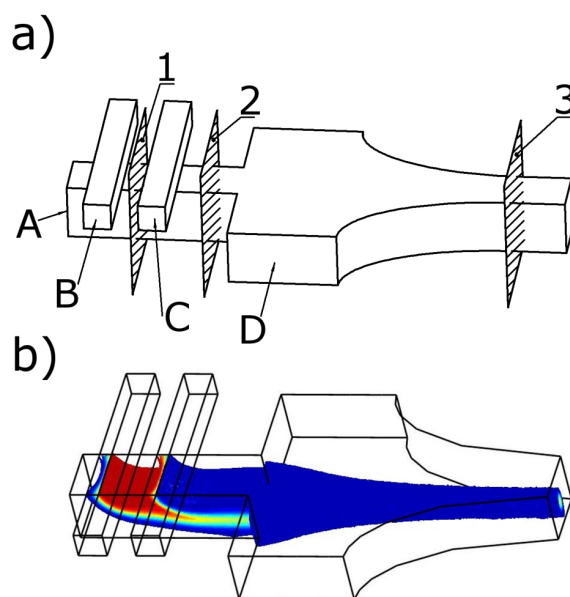


*Figure 6.10: a) Sketch showing the two-layer structure for 3D focusing, b) A concentration isosurface of the focused stream obtained by numerical simulation for the proposed 3D architecture, operating at a Reynolds number of 20. Here $Q_A = Q_B = Q_C = Q_D = 576$ $\mu L/hr$*

To (visually) verify the 3D focusing abilities, a solution of fluorescein was used as sample. Thus, confocal laser scanning microscopy could be employed to obtain cross sectional images of the sample distribution.

Fig. 6.11 shows the comparison of the simulation result and an experimental image obtained by confocal laser scanning microscopy of the cross-sectional profile in three positions along the main channel, namely positions 1, 2 and 3 as shown in Fig. 6.10a.
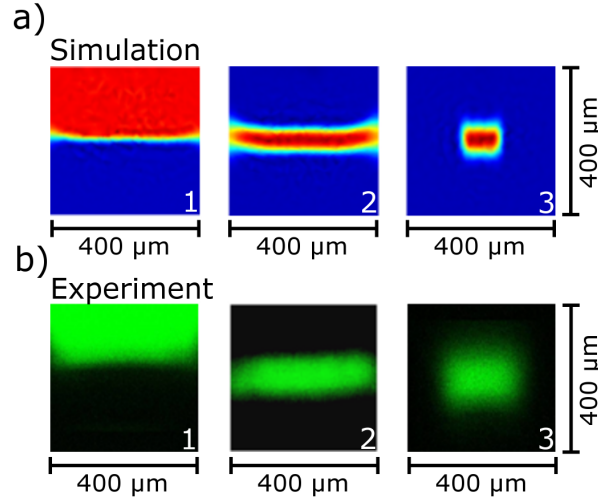
*Figure 6.11: Numerical simulation and experimental image using confocal laser scanning microscopy of the cross-sectional concentration profile of the focused stream in three positions as shown in Fig. 6.10a. Panels a 1-3) shows simulation results obtained through COMSOL. Panels b 1-3) shows experimental images obtained by confocal laser scanning microscopy*

From Fig. 6.11 it is seen that the similarity is close to excellent. Any remaining deviations can probably be accounted for by the fact that diffusion was not taken into consideration in the simulation.

After verifying that the flow system worked as intended in the PMMA prototype, the simulations were repeated, this time based on a channel structure with 100 $\mu$m wide SU-8 channels (A & D, Fig. 6.10) and 50 $\mu$m wide PDMS channels (B & C, Fig. 6.10), all 75 $\mu$m deep. These new simulation indicated that 3D hydrodynamic focusing also can be realized in smaller systems with similar quality (results not shown). Hence, we can safely assume that the flow focusing approach is valid for the SU-8 based chips with the smaller channels even without direct experimental confirmation. All chips used in this paper were designed according to the simulations with the smaller channel structures.

### 6.2.4.2   Optical detection region

The optical detection takes place at the centre of the chip, as shown in Fig. 6.9. To provide the cytometer with light, the beam from a 635 nm 5mW CW laser (Coherent, 31-0144-000) is focused at the tip of a multi mode optical fiber (Polymicro Technologies, FVP050055065) using a collimation lens (Thorlabs, F220SMA-B). This multi mode fiber has a large 50 $\mu$m i.d. core, which makes the laser to fiber coupling easier and less sensitive to vibrational noise.

The light is transferred from the fiber to the 60 $\mu$m wide and 75 $\mu$m high SU-8 waveguide via butt coupling. Due to the multi-mode nature of both fiber and waveguide it is possible to couple light from a circular to a rectangular geometry. Furthermore, specially

structured V-shaped fiber grooves in the SU-8 layer make the alignment of the fiber easy and precise (See Fig. 6.9).

Once the light from the incident fiber is coupled to the SU-8 waveguide, it can easily be guided from the coupling structure to the detection region. To prevent unguided light, (e.g., originating from the coupling interface) from reaching the detection region, the coupling structure is shifted sideways relative to the optical detection region. Due to the relatively high refractive index of SU-8, n=1.57, the critical angle for total internal reflection is below 40°. Hence, a 90° bend of the waveguide can be achieved using a 45° corner as a mirror surface [21]. By exploiting this feature, the waveguide can be fitted on a smaller chip area relative to a curved waveguide. Furthermore, according to raytrace simulations (see Fig. 6.12) the 90 degree bends add less divergence to the guided light than the curved waveguides do. This makes it easier to maintain the ligth as collimated as possible.
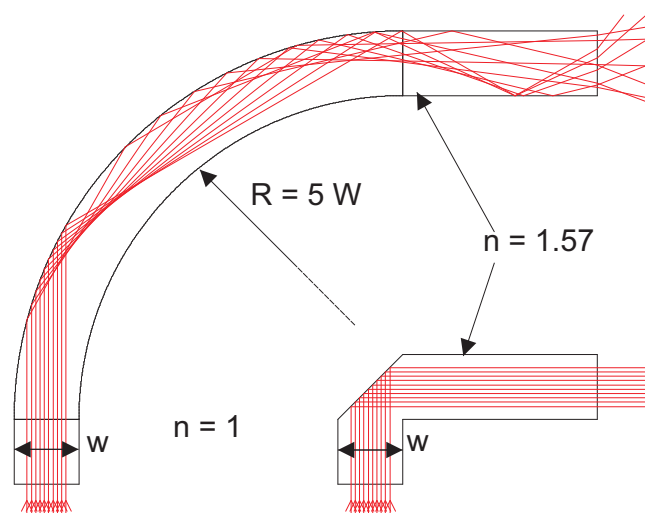


*Figure 6.12: A sketch of two differently curved waveguides. The sharp corner maintains the collimation of the light, whereas the wider curve adds angular dispersion. Hence, the sharp corner is preferred*

The 60 $\mu$m wide incident waveguide is split into two 30 $\mu$m waveguides (as shown in Fig. 6.9), each carrying approximately half the intensity. One 30 $\mu$m waveguide leads to the optical detection region, while the other is leading excess light out of the chip. The idea is that future generations of the chip will correlate data from two adjacent detection regions, thereby improving the signal-to-noise ratio. However, this feature has not yet been implemented here.
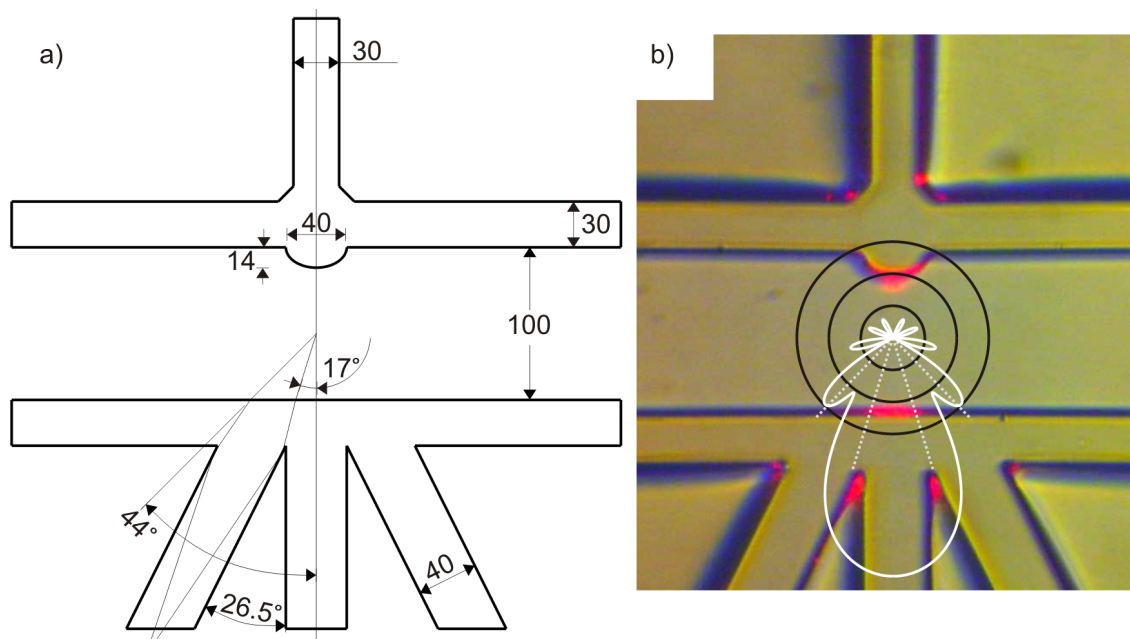
*Figure 6.13: a) Schematic of the geometry of the optical detection region. All units are in μm. The incoming light is focused by a 40x28 μm elliptical lens. The centre output waveguide serves as a beam dump, while data is recorded from the two tilted waveguides. Tilting these by 26.5° enables a sampling of forward scattered light between 17-44°. b) Photograph of the optical detection region captured through a microscope. Superimposed on the picture is a logarithmic plot showing the intensity of light scattered from a 1 μm particle (calculation was made with MiePlot v4.0.01). The concentric circles indicate factors of ten. The dotted lines show the scattering angles ±17° and ±44° between which light is collected*

Fig. 6.13 shows the geometry of the optical system in the central part of the microchip. The input waveguide ends perpendicularly to the main fluidic channel. At the intersection point the channel wall is 30 μm wide. Since both waveguides and channel wall are made in SU-8 they simply merge. To prevent the light beam from diverging when crossing the channel an elliptical lens is extruded 14 μm from the channel wall into the 100 μm wide channel. This results in a probe volume < 0.2 nL. Disregarding the volume of the sheath flows the probe volume can be reduced by up to a factor of 100 to 2 pL. As expected for a laminar flow setting, the lens extrusion was not seen to detrimentally influence the flow characteristics.

The waveguide directly across the channel from the incident waveguide is 40 μm wide. When detecting particles in the 1 μm range this waveguide simply acts as a beam dump. Only when dealing with much larger particles can any attenuation in the signal collected from this waveguide be measured. On each side of the center waveguide another 40 μm waveguide is located aimed towards the center of the channel (where the actual scattering will occur). The waveguide offset of 26.5° is based on Snell's law and geometric restrictions.

According to Mie theory most light scattered off a spherical object with a diameter slightly larger than the incident wavelength is scattered in the forward direction [14]. This is why the geometry is designed in such a way as to collect light from a forward scattering angle as small as possible, without collecting too much direct (non-scattered) light. All non-scattered light should be collected in the centre waveguide, while only scattered light (scattered at angles between 17° and 44°) is being simultaneously collected in the two adjacent waveguides.

The two output waveguides are coupled to optical fibers using the same kind of alignment grooves as for the input waveguide/fiber. The output intensities of the fibers are measured using two small (22 x 22 x 60 mm$^3$) photo multiplier tubes (PMT, Hamamatsu, H5784-06). The signal is passed through a 10 kHz, 12 dB low-pass filter (Stanford Research Systems, SR560) and then routed to a National Instruments DAQ card (National Instruments, SCB-68) and continuously recorded at a 10 kHz sampling rate. Both, data acquisition and the control of the syringe pumps are performed by a program written in LabVIEW ver.8.2 (National Instruments Inc.).

### 6.2.4.3 Materials

Three different sizes of polystyrene particles were used in separate experiments: 2.06±0.1 $\mu$m (Polysciences Inc, 19814-15) were used at a concentration of 0.9x10$^6$ particles/ml, 1.05±0.03 $\mu$m (Polysciences Inc, 07310-15) at 7.3x10$^6$ particles/ml and 489±15 nm (Polysciences Inc, 07307-15) at 0.6x10$^6$ particles/ml, respectively. These beads were diluted in MilliQ water to a suitable concentration in order to achieve reasonable count rates. SU-8 2075 photoresist was purchased from MicroChem (Newton, MA, USA). Polydimethyl-siloxane (PDMS, Sylgard 184) was purchased from Dow-Corning (Corning, USA) and used according to the manufacturer's instructions with a 10:1 mass ratio of base to curing agent.

### 6.2.4.4 Fabrication of the device

The device consists of two structured layers, a PDMS layer and an SU-8 layer. The main fluidic channels for in-plane focusing as well as the micro optical elements were fabricated in a single SU-8 layer by standard photolithography. A similar fabrication process has been described previously [53]. However, to enhance the adhesion between the negative photoresist SU-8 and the glass substrate, treatment with a solution of organic titanate in isopropyl alcohol, called AP300 (Silicon Resources, Inc.), was added to the fabrication procedure. Briefly, the glass wafers were cleaned in a "Piranha" solution ($H_2O_2$: $H_2SO_4$ = 1:3) for 10 min and subsequently dehydrated in a 250 °C oven for 10 h. After the wafers had cooled, AP300 was spun onto the wafers at a speed of 2500 rpm. Then, a 75 $\mu$m SU-8 layer was spun onto the wafers at the same speed and soft-baked on a hotplate (15 min at 60 °C, and 20 min at 90 °C, temperature ramp 7 °C min$^{-1}$). The wafers were cooled on the hotplate to room temperature and exposed by UV lithography, followed by a crosslink bake (10 min at 60 °C, and 15 min at 90 °C, temperature ramp 7 °C min$^{-1}$, cooled on hotplate). The final SU-8 structure was obtained after development. The out-

of-plane focusing channels and the sample channel were fabricated in PDMS. An SU-8 master was created using the above described microfabrication procedures. The master was placed into the bottom of a mold, and pins with a diameter of 1 mm were positioned on the master as place holders for the fluidic inlet and outlet cavities. Then, the PDMS was poured on top to make a layer of approximately 2 mm thickness. After curing and removing the pins, the PDMS was peeled from the master. Finally, the flow channels were sealed in a non-permanent fashion by stacking the two pieces on top of each other and gently compressing the PDMS in the chip holder.

### 6.2.5   Results and discussion

To test the performance of the micro flow cytometer, polystyrene particles with three different sizes (2 $\mu$m, 1 $\mu$m and 0.5 $\mu$m) were employed in three separate experiments. The tests were performed at a flow rate of 10 $\mu$L/min containing 1-10 % v/v particles. Based on results from numerical simulations these flow rates allowed 3D focusing. The corresponding maximum linear velocity can be calculated to about 4 cm/sec. Data was recorded at 10 kHz (due to hardware limitations). Combining sample frequency with the linear velocity and a 30 $\mu$m wide probe region, a resolution of 5-10 data points per particle was achieved. This resolution should in theory allow us to count up to 500 particles per second. However, the particle solution will never be perfectly uniform, so to avoid false signals caused by several particles passing the probe region simultaneously we used fairly low concentrations to achieve a much lower count rate during our series of test experiments.

Before plotting the data, the baseline offset was averaged out for both data sets (one set from each output waveguide), thereby pulling the baseline down to zero. Both data sets were then smoothed using a triangular averaging window five data points wide. The two data sets were then multiplied element-wise, thus greatly improving the signal-to-noise ratio. This is another advantage of our design, where several integrated waveguides can be used simultaneously, for improved signal-to-noise ratios or coincidence measurements. To detect the weaker signals from the smaller particles and to counteract differences in fiber coupling quality, the level of amplification in the PMTs was adjusted between experiments. Therefore, each of the combined data sets has been scaled to bring the peak heights to values around 5 to 10 (arbitrarily chosen).

Fig. 6.14a shows that the 2 $\mu$m particles were easily detected as the corresponding peaks clearly rise far above the noise level. Furthermore, we notice that all of these peaks are roughly of the same height indicating only particles of similar size passing. Thus, we assume that all events represent individual particles (no agglomeration). From the peak height histogram in Fig. 6.14b, it is clearly seen how the peak heights fall into two separate populations. The main population (in terms of counts) is originating from background noise; the second largest population represents the scattered light detected. The data shown in the histogram was collected over 60 seconds. A total of 295 particles were detected, giving an average count rate of almost 5 particles per second.

*Figure 6.14: a) Light scattered by 2 μm particles (the values are scaled to lie between 0 and 10). The highest data point of each peak (between two local minima) is marked with a cross. b) Histogram of the peak height for the entire 60 second measurement. Notice the number of counts for the noise population extents to 59049. During the measurement the total flow rate was 10 μL/min of which only 0.5 μL/min was sample solution, the rest was focusing buffer*

Fig. 6.15a shows a data sample from a measurement on 1 μm particles. In this case, the peak height varies more and lies closer to the noise level (which is also clearly seen in the histogram in Fig. 6.15b). From Fig. 6.15b, it can again be seen that the peak heights fall into two separate populations. However, the separation is much smaller in this case. Again, the main population is originating from background noise, while the other represents the detected light scattered from particles. Even though the peak heights still fall within a single population, this is now broader and less well defined than in the case of the 2 μm particles. In general, the variation in peak height is a bit larger than one would like to have for simple unequivocal identification. One possible cause could be that the increased diffusivity of the smaller particles counteracts the 3D focusing making the particles pass the laser sheet over too large a cross section, and thus experiencing different incident light intensities. Within the 60.6 seconds of recording 467 particles were detected, giving a count rate of 7.7 particles per second.

*Figure 6.15: a) Light scattered by 1 µm particles (the values are scaled to lie between 0 and 10). The highest data point of each peak (between two local minima) is marked with a cross. b) Histogram of the peak height for the entire 60.6 second measurement. Notice the number of counts for the noise population extents to 107843. During the measurement the total flow rate was 10 µL/min of which only 0.1 µL/min was sample solution, the rest was focusing buffer*

The third and final data sample, shown in Fig. 6.16a, is from a measurement conducted with 0.5 µm particles. From Fig. 6.16a it is evident that while clear events are registered the signals vary a lot and are now much closer to the level of the background noise. In fact, from the histogram in Fig. 6.16b it is seen that it is, in this case, no longer possible to separate the peaks into a noise- and a particle population without invoking more advanced statistical tools and selection distinction criteria. The results shown in the histogram imply that the intensity of the light scattered off individual particles varies with more than one order of magnitude, making a clear distinction impossible. For particles of this size to be detectable and to be distinguishable from the background a much tighter hydrodynamic focusing seems to be necessary. Under the chosen focusing conditions the diffuse movement of the nanoparticles is not sufficiently suppressed and hence the particles experience slightly different velocities going through the beam, but even worse, they are exposed to different parts of the Gaussian intensity profile of the incident laser sheet. A tighter focusing should alleviate this problem and yield more uniform signal intensities. However, this becomes very challenging, as it either requires a very low sample flow rate or very high flow rates for the focusing solutions. In the present realization of the system, optical detection of submicrometer-sized particles is possible, but a clear identification of particulate events is not yet possible due to the limited hydrodynamic focusing. To obtain at least an estimate of the particle count we choose to set a threshold at a peak height equal to 1, which resulted in a count of 365 peaks at 5.9 Hz for the measurement depicted in Fig. 6.16a.
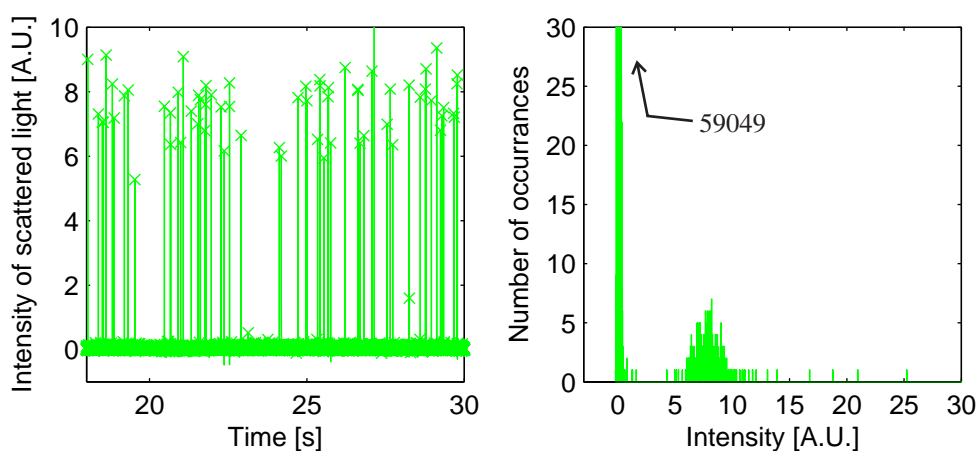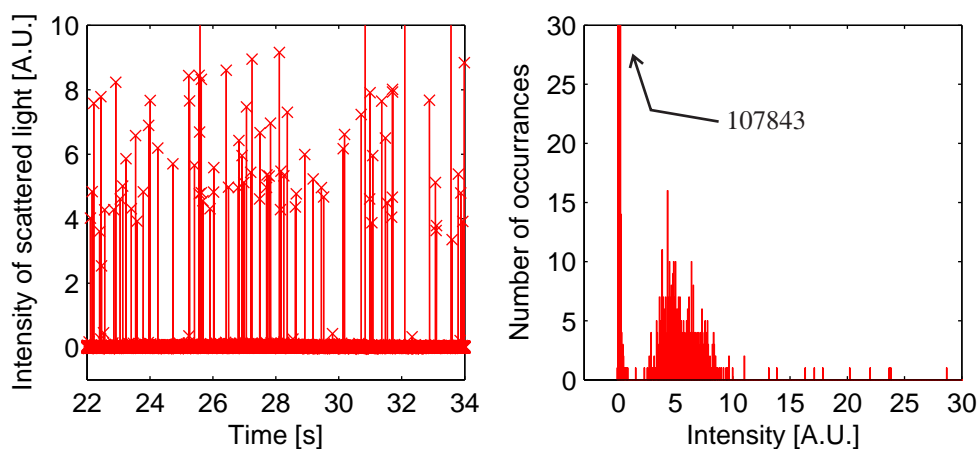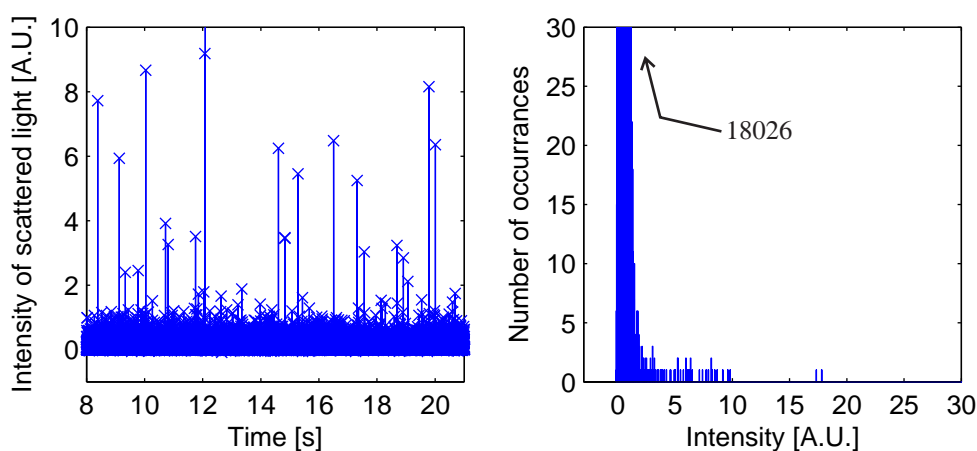
*Figure 6.16: a) Light scattered by 0.5 μm particles (the values are scaled to lie between 0 and 10). The highest data point of each peak (between two local minima) is marked with a cross. b) Histogram of the peak height for the entire 62 second measurement. Notice the number of counts for the noise population extents to 18026. This measurement was conducted at a total flow rate of 10 μL/min of which 1 μL/min was sample solution, the rest was focusing buffer*

It is noted that in all of the experiments only about 2/3 of the injected particles are accounted for. The lower counts can possibly be explained by a combination of sedimentation, particles sticking to channel walls and other losses. In all three measurements, a small number of peaks are much higher than all others (see, e.g., the histograms). These peaks are assumed to originate from agglomerates or clusters of polystyrene particles, as well as from dust particles. It is also possible that several particles passed simultaneously. Even though both 2 μm and 1 μm particles could be detected separately, the large dispersion in peak height makes it, at the current state, unfeasible to perform measurements on solutions containing a mixture of both size particles.

### 6.2.6   Conclusion and Outlook

We have shown that a micro flow cytometer can be designed and fabricated that is capable of detecting and counting unlabeled particles down to a size of 1 μm at a rate of at least 5 Hz. To our knowledge, this is first time that unlabeled particles down to 1 μm have been detected by light scattering in a micro flow cytometer using integrated micro optical elements and 3D hydrodynamic focusing system. The main channels for in-plane hydrodynamic focusing and the micro optical elements including waveguides, a micro lens, scatter structures and fiber-to-waveguide couplers were defined in a single SU-8 polymer layer by standard photolithography. The out-of-plane focusing channels and the sample channel were fabricated in a PDMS layer copied from an SU-8 master. Both numerical and experimental results indicate that the two-layered structure facilitates efficient 3D hydrodynamic focusing performance over a fairly wide Reynolds number range. Solutions of polystyrene particles, of three different sizes, were tested individually to evaluate the

performance of the device. The presented device clearly demonstrates that the application of microchip flow cytometers can be extended into the 1 $\mu$m or even the sub-micrometer size domain, even though fully quantitative counting of sub-micrometer-sized particles is not yet possible.

In order to enable differentiation of particles in mixed solutions, the spread in the scattered light intensity must be minimized. It is suspected that the key issue to be addressed is an improvement of the stability of the hydrodynamic focusing by lowering the total compliance of the system.

Further efforts are necessary to fully extend the application of the microchip flow cytometer to nanometer-sized particles and thus render it an intriguing detection tool for a range of biochemical assays involving submicro/ nanoparticles.

### 6.2.7 Acknowledgements

———————————— End of manuscript ————————————

## 6.3 Additional materials

In the last section of this chapter, I will describe two major changes to the setup. Neither of the changes had a direct influence on the performance of the chip, but they both helped to improve the overall handling of the device.

### 6.3.1 Improved fiber coupling

As shown in Fig. 6.1, up to this point in time the light was coupled to the fiber using a microscope objective and a fiber alignment platform, both placed on 3 axis microstages. This setup does, however, come with several disadvantages. With the fiber extending from the fiber platform, like a small cantilever, it was very sensitive to setup vibrations and even to minute air flows. Furthermore, the two microstages do not allow for angular corrections, making it much more difficult to align all the components properly. These issues were managed by reconfiguring the setup. Now, the laser diode was placed on a 3-axis stage and the microscope objective was replaced by a collimation lens (Thorlabs, F220SMA-B) fixed in an 2-axis angular-adjustable microstage. The optical fiber could then be attached to the lens using a bare fiber connector. Fig. 6.17 shows the improved setup.
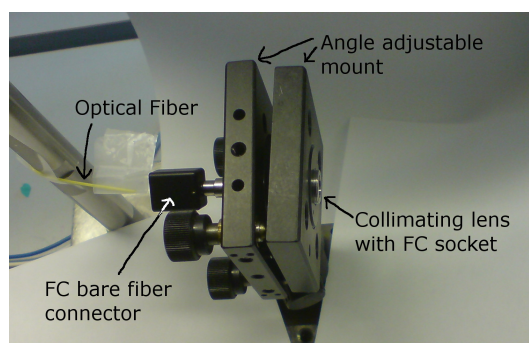
*Figure 6.17: This photo shows the collimation lens placed in 2-axis angular-adjustable microstage. On the left side of the lens the optical fiber is attached with a bare fiber connector. The laser is placed outside the picture to the right*

The ability to translate the laser in 3 directions makes it possible to hit the collimation lens very accurately. By being able to rotate the collimation lens in two directions, both orthogonal to the beam direction, makes it possible to accurately adjust the position of the focal point. With the use of the bare fiber connector, the position of the fiber end was fixed relative to the lens, thereby reducing the detrimental effect of vibrations. Since the fiber connector was made for standard 125 $\mu$m fibers, the only 65 $\mu$m wide optical fiber could not be removed and repositioned with enough accuracy to avoid realigning the lens angle. Due to the spring lock mechanism in the fiber connector the resulting tension in the fiber makes it position itself seemingly randomly in the connector hole. Hence, the optimal focal point may shift by approximately 60 $\mu$m.

The installation of this new light coupling setup did not improve the performance of the device as such, but the entire fiber handling procedure was made much more user friendly. This improved setup was definitely worth the costs of the collimation lens and the angular-mount.

### 6.3.2   Chip holder design

As the 3rd generation chip would require 3D focusing, several extra fluidic inlets were needed. In order to avoid the cumbersome manual insertion of the many needles a new holder was designed. The general concept of the new chip holder was to turn the chip upside down, such that the fluidic connection would come from below rather than above, while still passing through the PDMS layer. For the 3rd generation chip, the substrate had been substituted from silicon to glass in order to meet the integration-requirements from the DetectHIV project (Section 5.3). This gave the great advantage of being able to see through the substrate when doing microscopy. Since the fluidic connections all were moved away from the top of the chip, no needles or tubing would get in the way of the microscope. The main plate of the holder is shown in Fig. 6.18a. The plate measures 50 mm x 50 mm x 4 mm and was made in polycarbonate (PC). By building the plate in PC it was possible to use ethanol to clean it. In the center of the plate a 0.5 mm deep pocket was milled to fit the shape of the PDMS part. In the bottom of the pocket inlet holes

were drilled and 500 $\mu$m channels were milled to connect the drilled holes to the PDMS
through-holes. When the PDMS part is inserted into the pocket it aligns itself, and seals
the channels in the plate. The side channels were manually drilled after the micromilling
was completed. The chip was then placed on top of the PDMS with the SU-8 facing
down. After inserting the optical fibers, the chip was finally compressed by adding the
top PMMA part (Fig. 6.18b) and tightening the four screws.
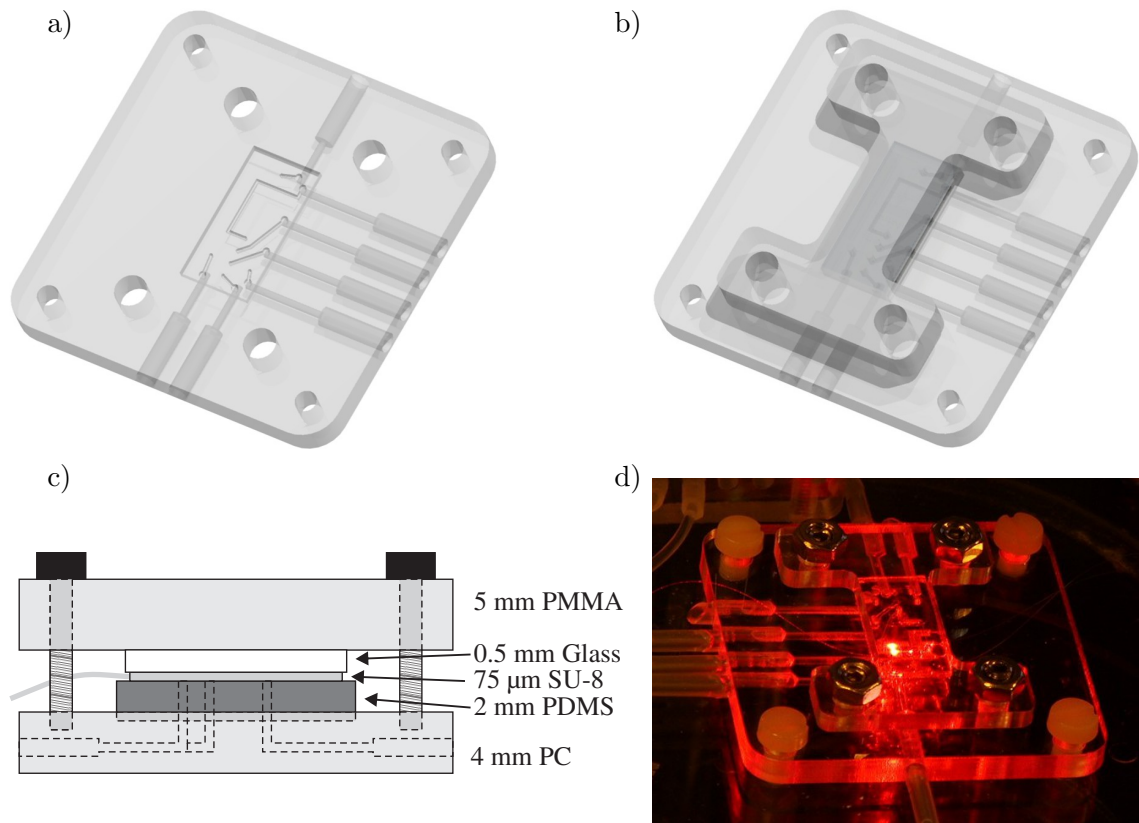


*Figure 6.18: Panel 'a' shows the main PC plate featuring both alignment pocket and
channels. Panel 'b' shows the PMMA top part used to compress the PDMS to obtain a
good seal between both PDMS/chip and PDMS/holder. Panel 'c' shows a sketch of the
holder cross section. Panel 'd' shows a long exposure photography of the assembled holder*

A cross section of the chip holder is shown in Fig. 6.18c. The interconnections between
tubing and the PC plate are described in [5] as "Needle-tubing press-fit"-connections.
Fig. 6.18d shows a long exposure photography of the assembled holder. The entire holder
was built to fit the microscope stage so that the chips could be easily examined during
operation. To illustrate that three dimensional flow focusing could be achieved on the chip,
the microscope picture in Fig. 6.19 was obtained by replacing the particle sample with a
concentrated dye. The two smaller channels (B & C) in the left part of the figure reside in
the PDMS layer and are therefore closer to the microscope. Notice that all channels have

the same depth. The dye is injected simultaneously from the two B-channels. Clear water is injected from the A-, C- and D-channels; this can be seen by the dye not spreading to these channels. At the first intersection, where the A-channel runs underneath the two B-channels, the dye appears even darker than in the B-channels as the absorption path at this channel intersection is approximately 1.5 channel height, as the dye extends into the underlying A-channel. In the channel between the first and second intersection the dye is seen to extend from side wall to side wall, while being clearly brighter compared to channel B. In the channel between the C- and D-channel the dye is, as expected, still extending across the full channel width, but, again, the dye appears brighter as it is laminated into an even thinner layer. When the dye reaches the D-channels it gets focused in the in-plane direction.
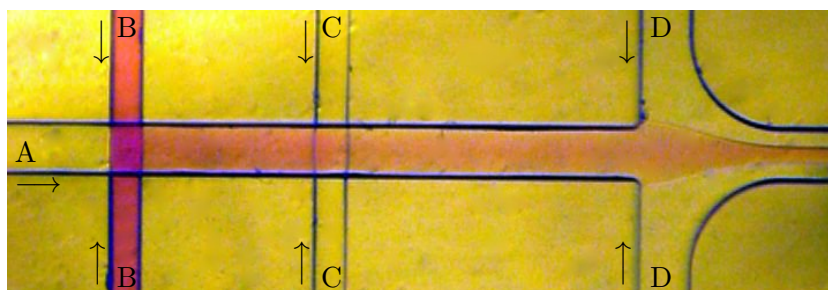


*Figure 6.19: This figure shows how the dye solution injected into both B-channels gets focused by the buffer flows. First the dye is focused in the out-of-plane direction and then in the in-plane direction. As the flows do not mix, and diffusion can be neglected, the color intensity of the dye can be used as a measure of layer thickness. Hence, the layer of dye is thinner between C and D, than between B and C. Color reprint in Appendix C*

Even though this does not prove without any remaining doubt that three dimensional flow focusing is actually achieved, it is a very strong indication.

# Lens based devices

During the experiments with the 3rd generation chip, I realized that there were several fundamental issues that needed to be addressed concerning the overall chip design. The most critical issue was related to the use of optical fibers. Even though optical fibers were successfully employed in the presented chips, I find it very unlikely that optical fibers will ever be successfully implemented in a commercialized disposable microchip. Even during the experiments large fluctuations in coupling quality were seen whenever a chip or a fiber was replaced, thereby limiting the reproducibility. The goal of the DetectHIV project was to eventually produce a chip and an instrument that could be used by non-experts (medical doctors). For a non-expert to be able to use a disposable chip it must be fairly durable and easy to align. As the chip was constructed in its third generation the fibers needed both careful insertion into the chip and into the collimation lens or the PMTs. The insertion of the fibers into the chip could be fixed during the fabrication process by gluing the fibers to the chip. This way the fibers only need to be connected to the instrument before use. This is, however, still too large of a challenge, as it requires the user to understand the alignment procedures and also to be able to judge when the alignment is good enough. Furthermore, the quality of the fibers may drastically change if the end of the fiber becomes dirty or damaged. Both dirt and damage may only be visible with high power microscopy, hence a possible end user cannot be expected to inspect the fiber ends before use. Finally, the idea of having a chip of only a few square centimeters with 20-30 cm long fibers extending from its sides is a packaging nightmare, as the fibers are by nature very fragile and cannot be bent too much without breaking. Based on these concerns, I decided to focus my work on examining the possibility of coupling light in and out of the chips using lenses rather than optical fibers. The goal was to approach a very simple "plug-and-play" functionality.

## 7.1 Generation 4 and 5

When the results for the 3rd generation chip and the concerns about the use of fibers were presented at the DetectHIV-meeting in January 2009, it was decided I would have until the 1st of April to implement, test and determine whether the DetectHIV project should aim for a fiber or a lens based approach. Leaving me with only two months decisions

had to made fast. This meant that all tests with the 3rd generation chip were stopped as the equipment, lab-space and time would be used for the new chip. The smart solution at this stage would have been to have two parallel setups, but as I was expecting the new setup to perform better (or at least equally well) and be easier to handle, the 3rd generation setup was retired. Secondly, the lack of time meant that I decided to initially focus on the in-coupling of light and leave the issue of out-coupling to later chip iterations. This decision was based on the fact that the connection of the output fibers to the PMTs was almost alignment free and much less critical than the input fiber, which besides the connection must be realigned every time.

The principal concept of the new design was to skip the input fiber alltogether and just point the laser at the end face of the input waveguide instead. However, in order to optimize this a few tricks were applied, including the addition of two lenses to the setup. One lens was made on-chip (the design of the on-chip lens is discussed in Section 7.3) the other was a bulk plano-convex cylindrical lens. In the setup, the laser is placed in a carefully designed holder, which would make sure the laser was perpendicular to the front face of the chip and in roughly the same vertical plane. For this setup, it was VERY important that the laser did not rotate relative to the chip. Translations up to a few millimeters were acceptable. Between the laser and the chip a plano-convex cylindrical lens was placed in order to focus the laser beam in the vertical direction (see Fig. 7.1b).
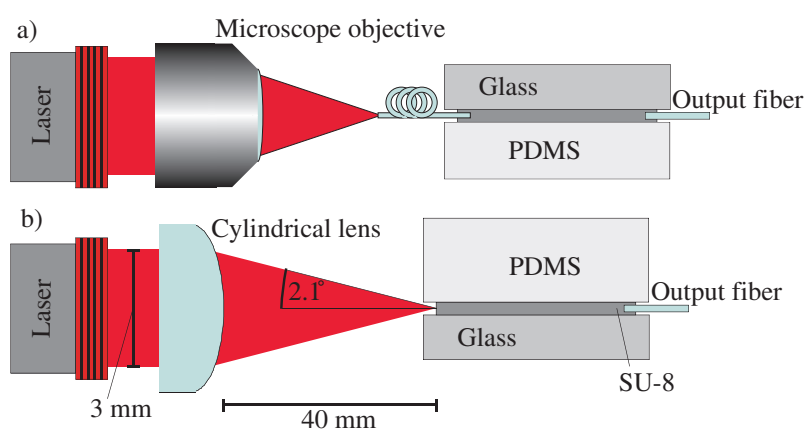


*Figure 7.1: This figure illustrates the differences between the fiber based coupling approach (Panel a) and the lens based approach (Panel b)*

By focusing the laser in the vertical direction a much larger part of the laser light hits the chip on the front face. This should ideally increase the collected light intensity by approximately one order of magnitude. Furthermore, the addition of this external (relative to the chip) lens helps reducing effects of vertical translations of the laser compared to the lens. Since all light hitting the external lens is focused to the same (vertical) point, moving the laser does not move the point. The angle of incident at the focal point, however, does change. A good thing about this translational freedom of the laser is that vibrational noise is reduced.

As shown in Fig. 7.1 the chip layers have been flipped to suit the common technology imposed by the DetectHIV project. Since the sample and the particles are supposed to be added by pipetting the glass substrate has to be on bottom.

### 7.1.1    Chip-in-a-case

Another big change from the 3rd to the 4th generation was the packaging of the chip. So far the various parts of the chip would be prepared and stored separately, until they would be assembled in the setup immediately before use. This meant that starting an experiment could take several hours, and the chip would take hours to replace if it broke. To avoid this, it was decided to assemble the chips during the fabrication process and keep them as a chip-in-a-case until they were to be tested. This would also make it much easier to ship the chips and remove a lot of manual work from the end user.

To seal the chip, provide means of alignment, and to accommodate the fluidic connector the chip with the PDMS lid was placed inside a case (see Fig. 7.2). The case around the chip consists of a 5 mm thick PMMA bottom part, and a 2 mm thick aluminium top part. The two parts are separated using a 4.5 mm thick PMMA spacer in each corner. It was decided to make the top part in aluminium rather than PMMA in order to have a small thickness while maintaining a sufficiently high stiffness.
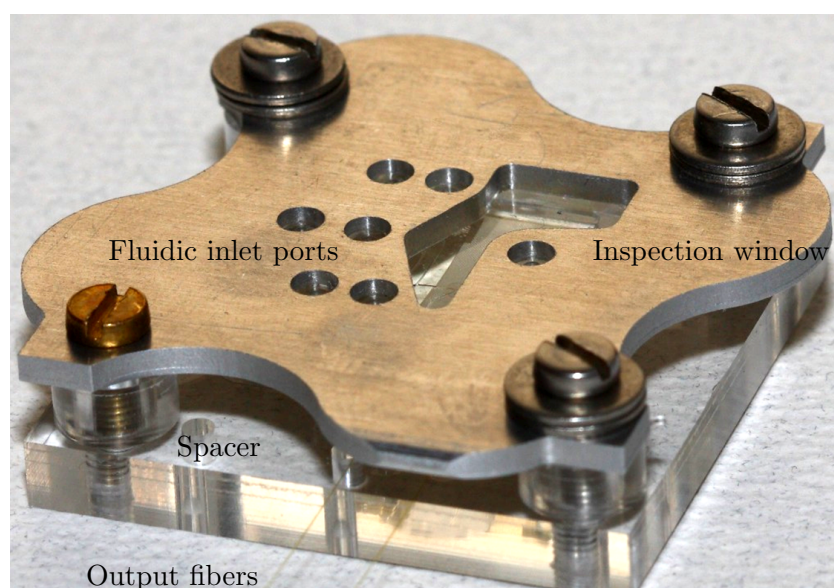


*Figure 7.2: This photo shows the chip inside the PMMA/aluminium case. The bottom part of the case is fitted with alignment holes to ensure a proper positioning relative to the laser. In the lower center of the picture two optical fibers can be seen extending from the case*

The bottom part of the case was fitted with holes that would complement the alignment pins fitted on the setup platform and thereby ensure a proper alignment relative to the

laser. A sketch of the setup platform is shown in Fig. 7.3. Here, the laser is positioned on the left on top of an x-y-z-stage. In the center of the setup the external lens was placed on a z-stage, and finally on the right the case containing the chip was placed on a platform. The x-y-z-stage and the laser would only need to be aligned once, then it should be fine for all chips (assuming the chips were all assembled properly). The z-stage with the external lens was needed since the PMMA substrates used for the bottom case would often vary in thickness and thereby shift the vertical position of the SU-8 layer. The shift was usually only in the order of a few hundred micrometer.
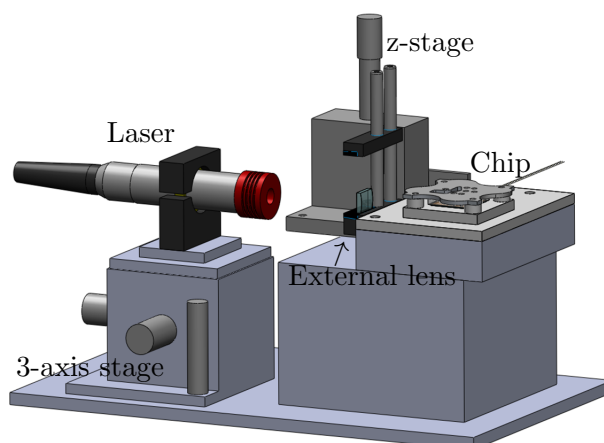


*Figure 7.3: This figure shows a 3D sketch of the setup used to evaluate if light could be coupled into the chip without using a fiber. The laser is placed on a 3-axis micro stage and the external in-coupling lens is placed on a z-stage*

To make the fluidic connections, a module was built from polycarbonate (PC) that would allow all the seven in- and outlets to be connected at the same time. The fluidic connector is shown in Fig. 7.4.
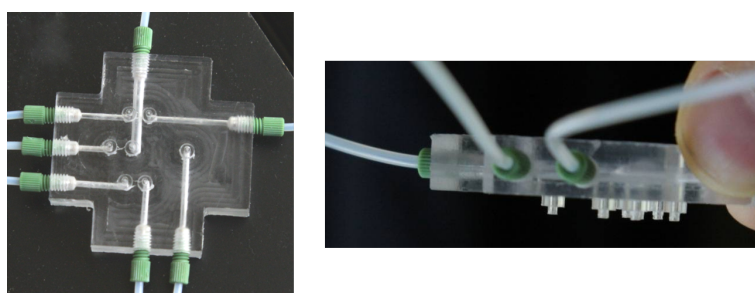


*Figure 7.4: These pictures show the fluidic connector used, which could easily be placed on top of the chip case*

To obtain a good seal, this fluidic connector was made with the same overlapping features as the one depicted in Fig. 7.20b. The pump-side of the fluidic connector is threaded and fitted with tubing connectors from Upchurch Scientific.

### 7.1.2 Improved scatter structure

With the fourth and fifth generation of the chip the scatter structure was improved in two steps. For the fourth design iteration, a zigzag pattern is added to the edge of the SU-8 pillars as shown in Fig. 7.5a. The purpose of this addition is to add more variety to the structure, so the parallel rays are spread out faster. The side length of the zigs and zags is around 5-10 $\mu$m, which makes these features too small to develop accurately. Due to the surface tension of the SU-8 the otherwise sharp corners are rounded, leaving the zigzag pattern looking more like a sinusoidal wave. This 'imperfection' was actually intended, as the sinusoidal shape will spread the light more smoothly.
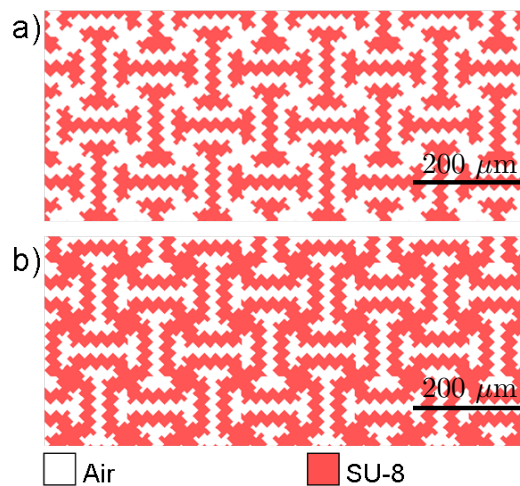


*Figure 7.5: Panel a, shows how the sides of the pillars were shaped in a zigzag pattern. Panel b, shows the final version of the structure. By inverting the structure it becomes much more stable*

One of the problems we had been facing during the fabrication of the chips was to make the SU-8 adhere to the glass substrate. Initially, the problem was solved by spinning a layer of AP300 onto the substrate, but the small scatter structures were still falling of once in a while. The solution to this issue was surprisingly straightforward, once realized. A much more stable structure was obtained by simply inverting the scatter structure as shown in Fig. 7.5b. This meant that even if part of the structure would detach from the substrate, it would still be held in place and not obstruct the functionality of the chip by blocking the flow or by coupling light out of the waveguides.

### 7.1.3 3D hydrodynamic focusing

When testing the 4th and 5th generation of the chips it quickly became obvious that there was a huge problem regarding the establishment of 3D focusing. By monitoring the signal from the light scattered by the passing particles it could be seen the something was wrong. Either the particles would leave signals varying far too much to be caused by a well focused flow or the particles would pass the detection region in intervals separated

by pauses where nothing was passing the beam. These problems came as a surprise, since the design of the microchannels had not been changed significantly between the chip generations. The largest change was the chip now being working with the PDMS facing up rather than down. As the direction of gravity usually does not influence microfluidics this was not considered being the cause of the problems. Through numerical simulations, it was verified that the employed geometries and flow conditions should provide a working 3D focus. Fig. 7.6 shows the result of three of such simulations.
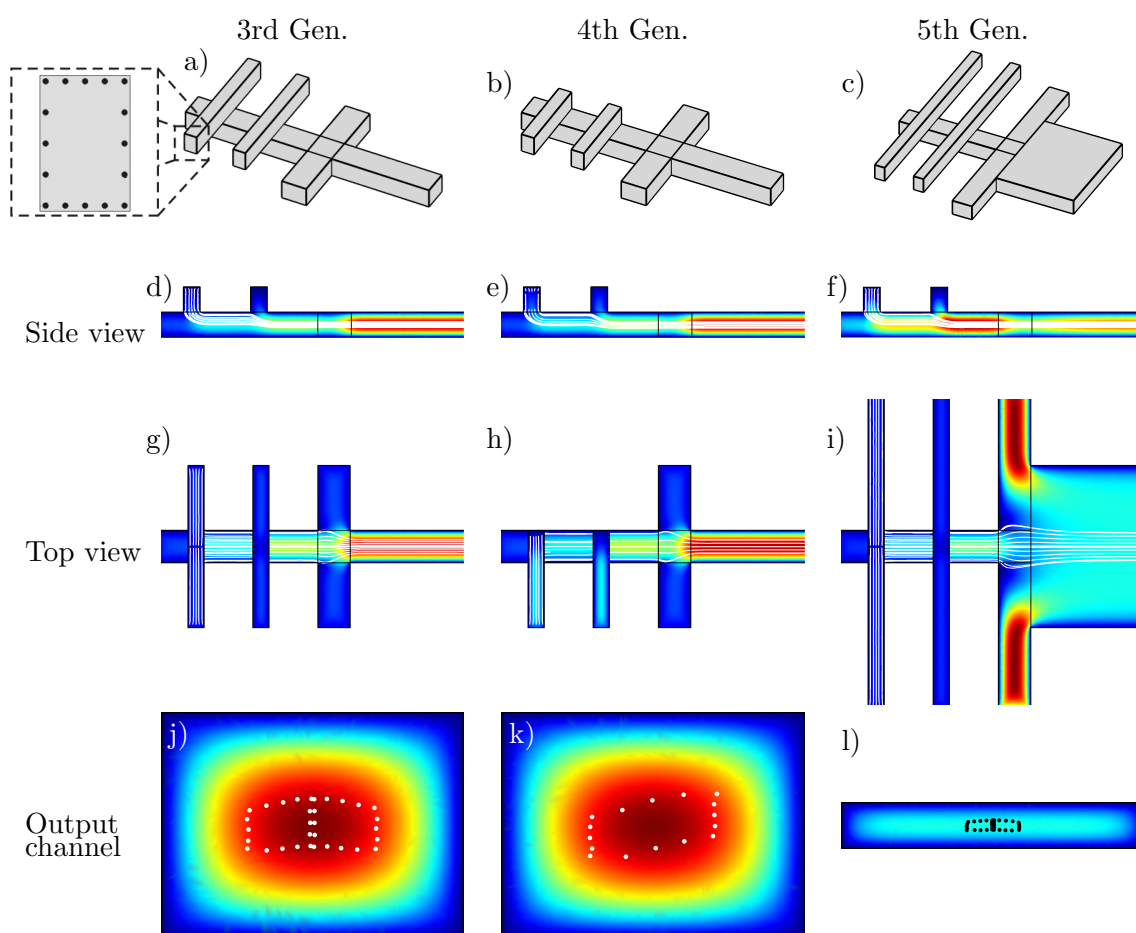


*Figure 7.6: This figure shows the result of three flow focus simulations. The displayed streamlines are all starting around the boundary of the sample flow, as shown in Panel a. In Panel j, k and l, it can be seen that the sample-streamlines are well confined to the center of the main channels. The two first simulations were performed at a total flow rate of 10 μL/min evenly distributed on all inlets. For the simulation featuring the wide main channel each in-plane sheath flow was set to 12 μL/min, giving a total flow rate of 30 μL/min. Color reprint in Appendix C*

In these simulations, the streamlines are starting along the boundary of the sample

flow(s) as indicated by the dots in the insert in Fig. 7.6a. The left column shows the geometry used for the 3rd generation. When this setup did not work for the fourth generation chip, a new channel design was created for the PDMS layer. Instead of having the sample flow and the top sheath flow arriving from both sides the channels were made on only one side. As can be seen in Fig. 7.6k, this breaks the symmetry of the focusing. The part of the sample flow furthest from the inlet side is less compressed, but the sample flow is still quite well confined to the center of the channel. The advantage of this second channel configuration is that air bubbles are much less prone to get stuck in these channels, as the flow does not have an alternative route. The right column shows a simulation of a 500 $\mu$m wide main channel, showing that also in this case 3D focusing should be possible.

The initial guess to the cause of the flow focusing problem was the presence of air bubbles. If these bubbles would repeatedly be compressed and re-expand it would cause fluctuation to the flow rates. Such flow rate fluctuations can very well be what causes the focusing to fail. All the simulations that were performed to verify the flow state were based on the assumption of the system being in 'steady state', hence any time variation (such as fluctuating flow rates) will make the simulations invalid.

To remove the bubbles, the system was carefully purged and the PDMS-lid (with channels) and the fluidic connector were redesigned several times to reduce dead volume and try different channel configurations. Though this helped eliminate the bubbles it did not fix the focusing. So, naturally the next thing that was considered as causing the problems was the quality of the pumps and syringes used and the compliance of the soft PDMS-lid itself. The only problem with these items is that they were all part of the functioning 3rd generation setup and could therefore not be (solely) responsible for the failed focusing.

Due to the lack of time this was not further investigated.

### 7.1.4  Conclusions on the 4th generation

The main objective with the fourth generation of chips was to evaluate the feasibility of coupling the laser light into the chip with lenses rather than optical fiber. Even though the particle counting experiments using the fourth generation chip were unsuccessful, it was verified that light indeed could be coupled to the chip using a combination of on-chip and external lenses. With the chip-in-a-case concept, it was much easier to replace one chip with another, and by using the case to align the chip to the setup (see Section 7.3) the coupling of light into the chip became much easier. The alignment of the chip could to a large extent be verified by simply noticing the behavior of the light scattered by the chip itself. If the light/chip is in the correct vertical position one can clearly see the light being focused at the back of the on-chip lens. Should the vertical position be off, the intensity of the focused light would be clearly lower. If the chip would be slightly rotated, then the focal point of the lens would move sideways and miss the optical fiber. In order to be able to see when/if the light did not couple to the fiber, due to rotation induced in-plane offset, the scatter structure was placed right behind the on-chip lens so the chip would literally light up. To illustrate a successful coupling of light using the lenses Fig. 7.7 shows a fourth generation chip without the PDMS lid and without the surrounding case. The chip

footprint measures 20 mm by 20 mm and was made to fit directly into the layout of the integrated chip (see Fig. 5.5). Based on the experiences with this chip, it was decided that the DetectHIV project would use the lens based solution and employ the chip-in-a-case concept.
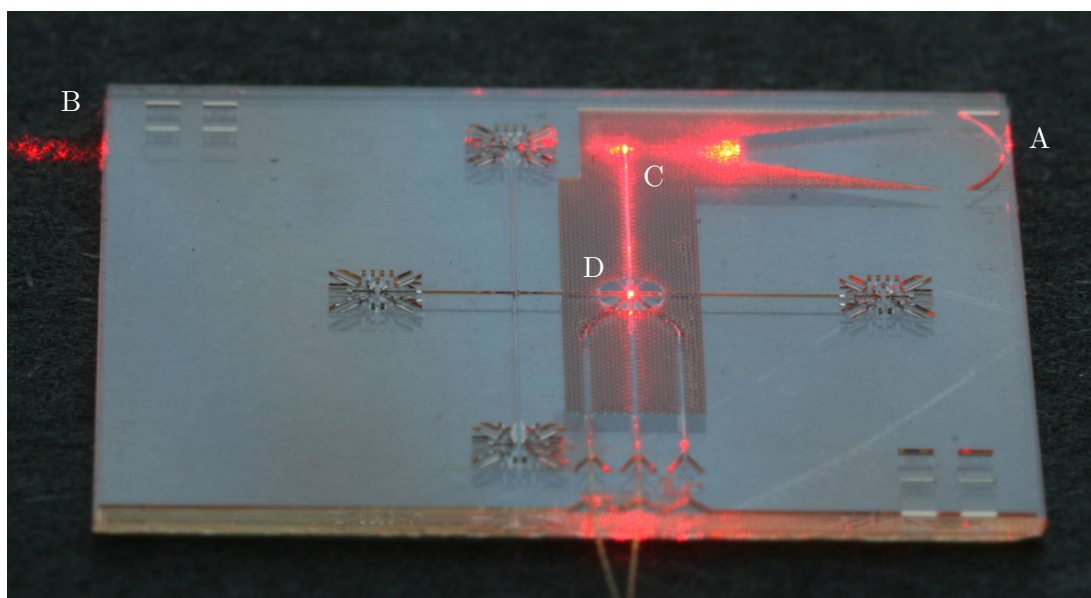


*Figure 7.7: This picture shows the 4th generation chip without PDMS lid and case. At 'A' the front face of the on-chip lens is seen, the external lens and the laser is outside the picture to the right. If the laser beam is not sufficiently focused by the external lens, some of the light will not hit the SU-8 lens and pass unguided through the chip to exit at 'B'. The scatter structure, 'C', is used to prevent stray light from flooding the chip. At 'D' it can be seen that a fair amount of light reaches the detection region. The chip is designed to be directly implemented to the design of the integrated DetectHIV-chip*

### 7.1.5  Conclusions on the 5th generation

The fifth generation chip was made with a 500 $\mu$m wide main channel, hence the detection waveguides could be placed to collect scattered light between 11° and 18°, which should be advantageous due to the increased amount of light scattered at lower angles. With the inverted version of the scatter structure, the fabrication yield was greatly improved and with the introduction of the chip-in-a-case concept, the issues with PDMS bulging down into the main channel, could be accurately controlled and easily reproduced.

As already mentioned, the 3D focusing would not work consistently for the fifth generation chip as well, hence the results shown in Fig. 7.8 were obtained without a 3D focusing flow. Though these results show a widely varying peak height, it is possible to see a significantly larger overall response from the 2 $\mu$m particles compared to the 1 $\mu$m. Hence, by evaluating the largest peak heights, it may be possible to extract information about the largest particles in a mixed sample (singlets and doublets). This concept is

further investigated in Section 7.4.3.1. These two measurements were carried out on the same chip, using the same optical settings. First the test with the 1 $\mu$m particles was conducted, then the chip was cleaned by flushing with MQ-water for 20 minutes before performing the test with the 2 $\mu$m particles. Though the chip was flushed there was still a low population of 1 $\mu$m particles present during the 2 $\mu$m experiment, but no 2 $\mu$m were present at the 1 $\mu$m test. The data was recorded from both output waveguides at 20 kHz after passing a 6 db 30 - 1000 Hz band pass filter.
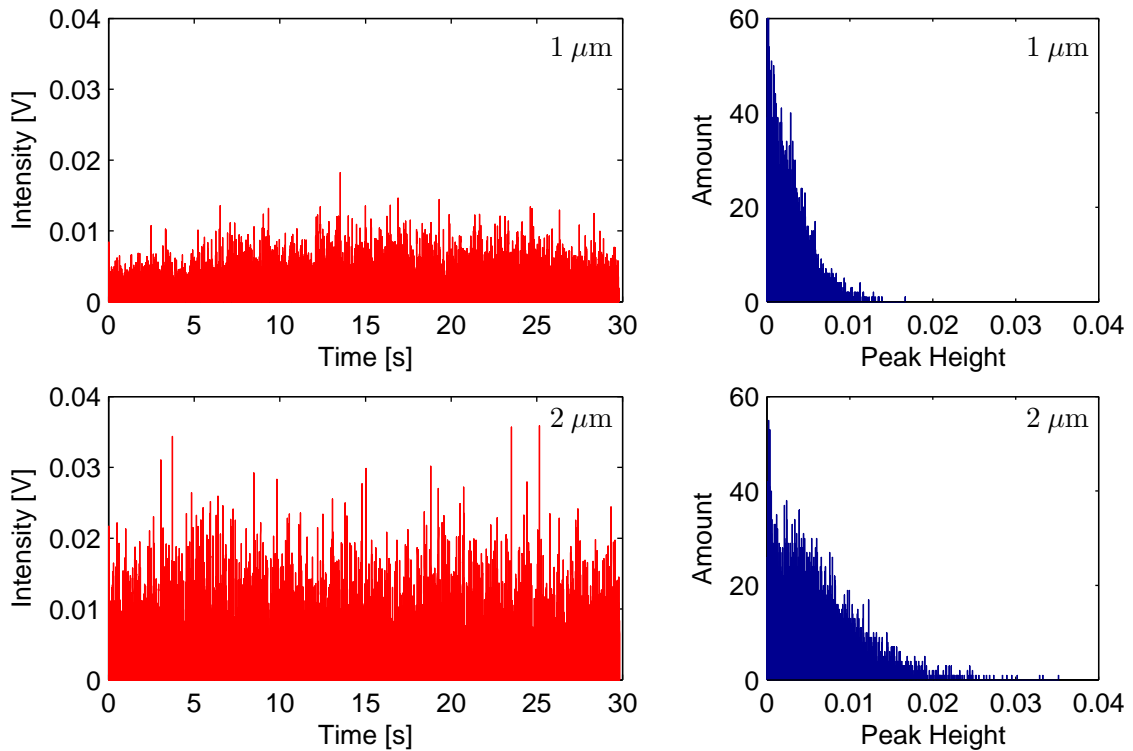


Figure 7.8: These plots shows the results of two separate measurements performed with the same chip. The upper plots show the signal from 1 $\mu$m particles, while the lower plot shows a 2 $\mu$m result. Notice that due to reuse of the chip the 2 $\mu$m data may contain traces of 1 $\mu$m particles. The left column shows the obtained data from the two waveguides after being combined and treated. The right column show histograms to illustrate the distribution of peak heights. Notice the plots have identical axes, hence it is easily seen that the 2 $\mu$m particles in general produce stronger signals. The total flow rate of the 1 $\mu$m and 2 $\mu$m experiments were 10 $\mu$L/min and 5 $\mu$L/min, respectively

To show that the 5th generation design was not fundamentally flawed with respect to achieving 3D focusing, the data shown in Fig. 7.9 was obtained during one of the rare occasions where it did in fact work. The peak heights of this experiment should not be directly compared to those above, as they were not obtained using the same chip, fibers or settings. There was found no experimental correlation between the used flow rates and the probability of successfully establishing 3D focusing.

With the hope of eventually being able to fix the unstable flow and based on the possibility of extracting information about the particle size even without well established 3D focusing, it was decided to use the 5th generation chip for implementation in the DetectHIV-project.
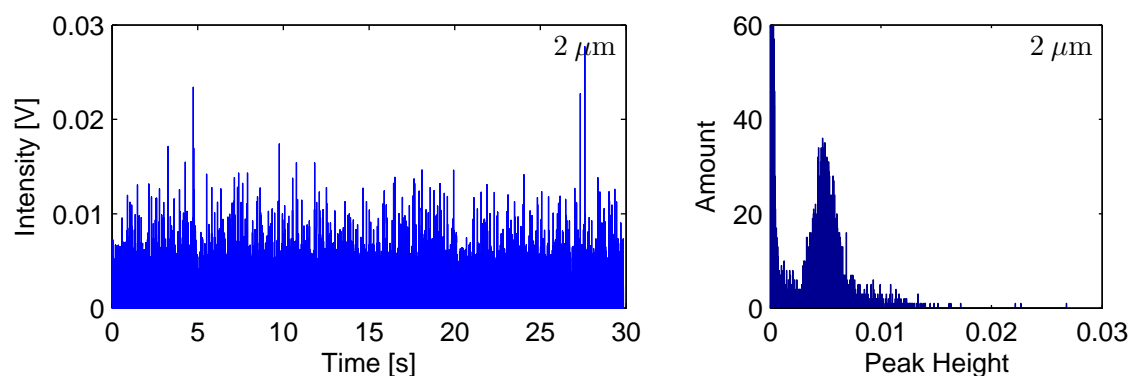


*Figure 7.9: This plot shows the result of a successfully established 3D focusing experiment performed with 2 µm particles. During this test the total flow rate was 30 µL/min*

## 7.2 Generation 6

Based on the successful use of lenses to couple light into the chip, I decided to focus my efforts on using lenses to couple the light out of the chip as well, thereby completely freeing the chip from optical fibers. To improve the stability of the setup the microstage carrying the laser was replaced by a micromilled PMMA holder. Hence, the whole setup could be made much more compact and therefore more stable. The 6th generation setup is shown in Fig. 7.10. Notice the two PMTs have been replaced by a photo detector (Thorlabs, PDA36A-EC) and the electronic filters have been removed.
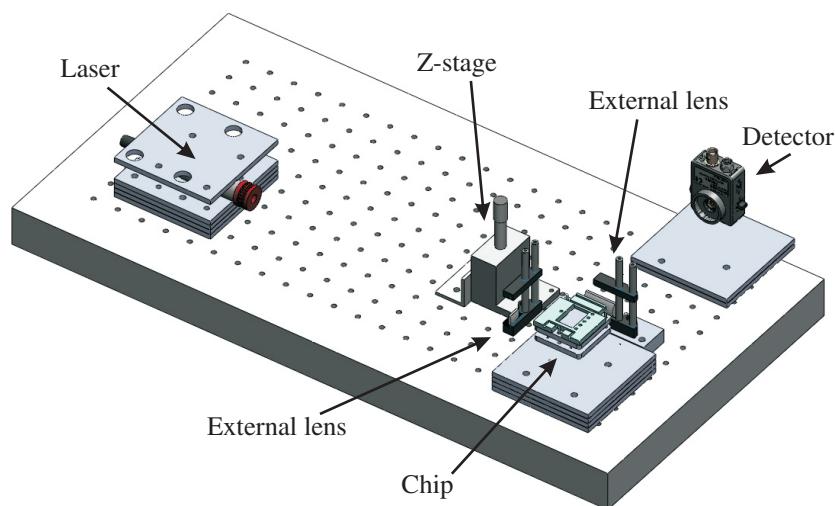
*Figure 7.10: This figure shows the setup used for the 6th generation chip. By combining micromilled holders with the grid in the optical table, sufficient alignment accuracy can be achieved*

### 7.2.1 Failed focusing

The flow focusing was not completely abandoned, however. With the sixth generation chip, a slightly different channel design was attempted. Where we before, in the 3rd, 4th and 5th generation, had been using two stacked channel layers (SU-8 and PDMS), the sixth generation chip only has well defined channels in the SU-8 layer. However, in order to obtain a three dimensional channel structure the PDMS lid is fabricated with loops to connect the SU-8 channels in the out-of-plane direction. The layout of the chip is shown in Fig. 7.11a, and a photo of a cross section of the PDMS lid showing one of the loops is shown in Fig. 7.11b. Since the best 3D focusing results were obtained with the 100 $\mu$m wide main channel, this new chip was made with a 100 by 75 $\mu$m$^2$ main channel. The thickness of the SU-8 layer could now be freely chosen as it no longer had to fit with the fibers. The thickness was, however, kept at approximately 75 $\mu$m as the SU-8 fabrication procedure (Section A.1) was already optimized for this. The loops in the PDMS lid were made by pulling a nylon string (fishing line) through the mould before the PDMS is casted.
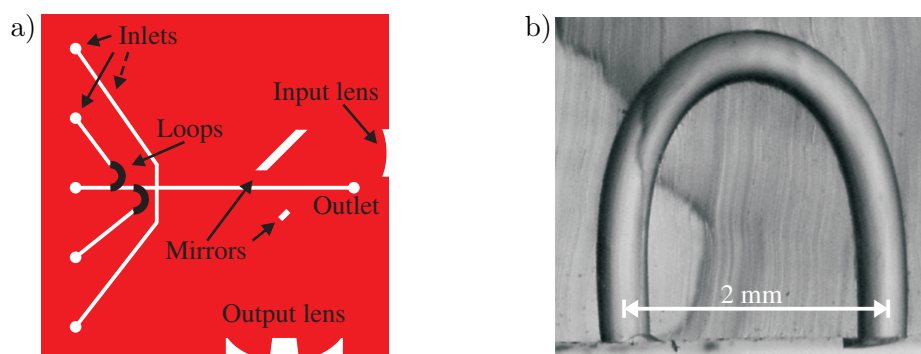
*Figure 7.11: Panel 'a' shows the layout of the channel on the 30 mm x 30 mm 6th generation chip. Notice how the 2nd and fourth inlet channels are connected to the main channel through loops in the PDMS lid. Panel 'b' shows a vertical cross section of the PDMS lid containing the channel loop. With these loops it becomes possible to utilize the 3rd dimension to connect channels on an otherwise planar chip*

By using micromilling to fabricate the mould, the holes for the nylon strings can be very accurately controlled. Hence, only the position of the loop in- and outlet and the diameter are well controlled, the exact shape of the loop will vary a little from part to part. The substitution of channels in the PDMS part with loops made the fabrication of the PDMS parts much easier. The flow simulations presented in Fig. 7.12 show that 3D focusing should be possible with loop-channels of both 200 $\mu$m and 400 $\mu$m diameter.
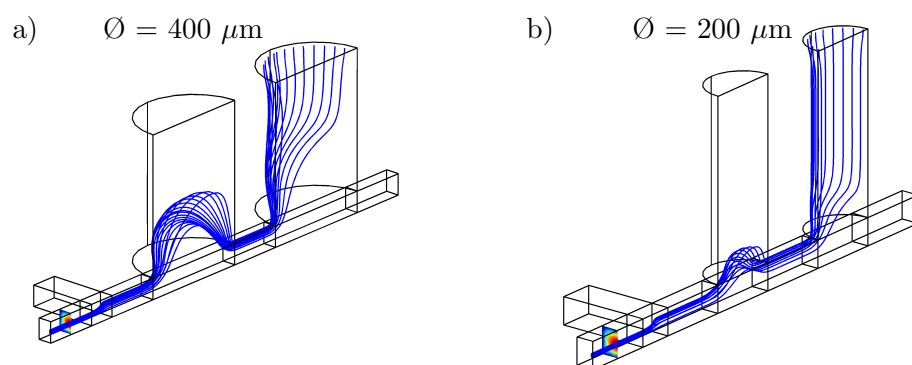


*Figure 7.12: This figure shows the result of two simulations. One with a loop diameter of 400 $\mu$m, the other with 200 $\mu$m. In both cases 3D focusing is achieved with a total flow rate of 25 $\mu$L/min. The stream lines are started close to the wall of the sample inlet tube, and are seen to be very sharply focused a the end of the channel*

Notice only one half of each geometry was modeled using symmetric boundary conditions along the mirror axis. This way a higher resolution of the mesh can be achieved, thereby increasing the precision of the result. Also notice how the flow in the main channel in both simulations extends up into the loop-channels before being pushed back down.

This effect is clearly proportional to the diameter of the loop-channels, and hence less pronounced in the 200 $\mu$m case.

As was the case with the 4th and 5th chip generation, the 3D flow focusing could not be established in the 6th generation chip either (despite the encouraging simulation results). So, in order to be able to actually perform any useful test on this system, the direction of flow was changed, such that the outlet as shown in Fig. 7.11a, was instead used as inlet, and the five original inlets were used as outlets. Hence, the chip basically only contained one channel. With the reversed flow direction, the much simpler channel form also made it possible to efficiently clean the chip by flushing for only a few minutes, something which was not previously possible.

## 7.3 Lens based cytometry manuscript

A revised version of this manuscript has been published (see List of Publications on page xix).

———————————— Start of manuscript ————————————

# Fiber free coupling between bulk laser beams and on-chip polymer based multimode waveguides

**Thomas G. Jensen, Lars Nielsen, Jörg P. Kutter\***
*DTU Nanotech*
*Dept. of Micro and Nanotechnology, Technical University of Denmark (DTU)*
*Buliding 345 east, DK-2800 Kgs. Lyngby, Denmark.*
*\*To whom correspondence should be addressed;*
*email: joerg.kutter@nanotech.dtu.dk, Fax: +45 4588 7762, Tel: +45 4525 6312*

### 7.3.1 ABSTRACT

In this paper, we demonstrate the design of a virtually alignment free optical set-up for use with microfluidic applications involving a layered glass/SU-8/PolyDiMethylSiloxane chip. We show how inexpensive external lenses combined with carefully designed on-chip lenses can be used to couple light from a bulk beam to on-chip waveguides and back into a bulk beam again. Using this setup, as much as 20 % of the light coming from the source can be retrieved after passing through the on-chip waveguides. The proposed setup is based on a pin-aided alignment system that makes it possible to change chips in the optical train in only a few seconds with a standard deviation of about 2 % in the transmission intensity. Furthermore, we demonstrate how these optical set-ups can be combined with microfluidics to create an on-chip flow cytometer enabling detection and counting of polystyrene particles down to 1 $\mu$m at a rate of 100 Hz.

### 7.3.2 KEYWORDS

light coupling, alignment free, waveguides, microfluidics, cytometry, lenses.

### 7.3.3   INTRODUCTION

In recent years, a lot of research has been put into the development of Point-Of-Care (POC) devices. These devices are characterized by their ability to function in the field or as desktop-sized units in non-specialized laboratories, where they may be operated by non-technicians. Many of these devices are built around the same basic principle of a small and cheap disposable microfluidic chip, which is loaded into a reusable highly automated instrument. In a large group of these devices, the detection mechanism is based on light (as opposed to, e.g., electrical or chemical) interactions.

Typical exploited interaction phenomena include absorption, fluorescence, scattering or various clever designs where changes of the refractive index are detected. During the years many different solutions have been presented (e.g.[58, 59, 60, 61]). The one thing in common for all these chips is the necessity of a surrounding instrument to provide a light source and a detection platform. There are exceptions, however, where both light sources and detectors [62, 63] have been integrated on chip, but these solutions are complex and expensive.

A common way to supply light to a chip is to couple the light source to an optical fiber, which can then be inserted into the chip [64, 65, 66, 67, 61]. A second method, which is often used in fluorescent based measurements, is to project light into the microfluidic channel using a microscope objective combined with a semi-transparent mirror [68]. Another, but less used, method is to simple point the laser directly at the waveguide end facets [69].

The first method mentioned is working relatively well in the highly controlled environment of a lab: it is, however, very difficult to see how a solution based on optical fibers can be commercialized. Since the quality of the fiber-to-chip alignment is very critical it is not acceptable to require the users/consumers to insert the fibers themselves. Hence, the chip must be shipped already fitted with the fibers. Yet, this still leaves the consumer with the task of attaching the fibers to the light source and possibly to the detector. Perhaps a possible task if assisted by bare-fiber-connectors or with permanent connectors, it does, however, still put the very fragile fibers in the hands of untrained users. The second method mentioned above, which, by default, is dependent on a microscope, will therefore for most applications be far too expensive to mass produce. The third method, which sends the light directly at the on-chip waveguide facets, is also associated with a few disadvantages. Firstly a large amount of the light will not be coupled into the device, and will instead scatter and perhaps even cause problems as unguided light. Secondly, this method puts a lot of limitations on the possible use and placement of sources and detectors.

Consequently, what is required to make these light-based devices work reliably and in a way that makes commercialization possible, is an instrument, which, when in use, is virtually alignment free and without any fragile components. A method to avoid the use of optical fibers for fluorescent detection was presented by Seo and Lee in 2004 [70], where multiple cylindrical on-chip lenses were used to focus light from an LED.

What we propose in this paper is a solution for an optical setup completely freed from optical fibers and without any expensive optical components. The proposed setup has only

one critical alignment step, which is during the chip assembly. Hence, from an end-user's point of view it is essentially alignment free.

### 7.3.4  THEORY

#### 7.3.4.1  General setup

The principal concept of the proposed method is to avoid the use of optical fibers altogether by pointing the laser at the end face of the input waveguide instead. However, in order to optimize this approach a number of improvements and novel design aspects are introduced, including the addition of several lenses to the setup. The setup consists of five main elements (ignoring any fluidics, electronics, etc.).
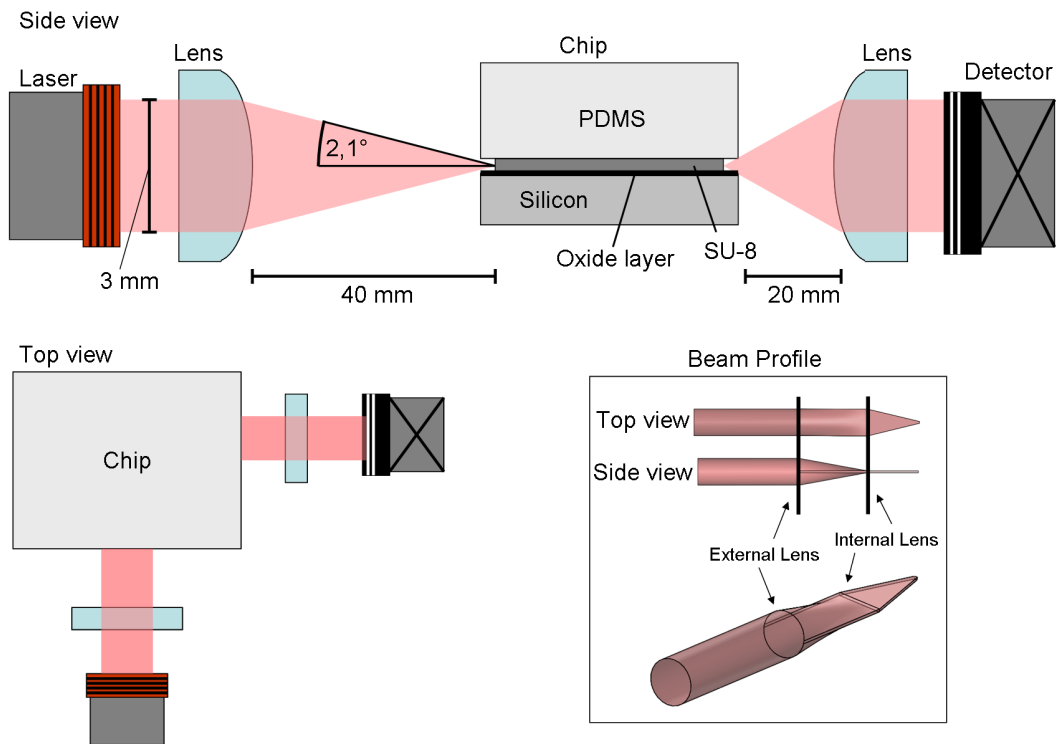


*Figure 7.13: This figure shows a sketch of the five optical components in the setup. The laser to the far left, then an external cylindrical lens. In the center, the layered microchip and on the left another external lens and a detector. Notice the laser and the detector are facing orthogonal directions in order to avoid unguided light from reaching the detector. The insert shows how the beam is first focused in one direction and then in the other*

The first element (see Fig. 7.13) is a 5 mW 635 nm laser diode (Coherent, 31-0144-000), from which a collimated beam is sent to the second element, a plano-convex cylindrical lens (Thorlabs, LJ1402L1-A), in this case with a focal length of 40 mm. At the focal point of the lens we position the edge of the third element, the chip. The chip itself consists of

a 75 $\mu$m thick patterned SU-8 layer on glass or silicon substrate. To seal fluidic channels a 5 mm thick Polydimethylsiloxane (PDMS) layer is used as a lid. The fourth element, also a plano-convex cylindrical lens (Thorlabs, LJ1328L2-A), is placed on the output side of the chip. The fifth and final element is the photo detector (Thorlabs, PDA36A-EC).

Between the laser and the chip a plano-convex cylindrical lens is placed in order to focus the laser beam in the vertical direction. By focusing the laser in the vertical direction a much larger part of the laser intensity hits the chip on the front face. Furthermore, the addition of this external (relative to the chip) lens helps reducing effects of vertical translation variations of the laser compared to the lens. Since all light hitting the external lens is focused to the same (vertical) point, translating the laser does not shift this point. The angle of incident at the focal point does change, however. A positive consequence of this translational freedom of the laser is that vibrational noise is reduced as well.

By positioning the chip at the focal point of the external lens, the beam is shaped as a thin line rather than a circle. Without going into further details at this point (but as shown later), we just note that the light passes through the chip and exits again in the shape of a line, which only diverges in the vertical direction. This allows us to use a second cylindrical plano-convex lens to shape the outgoing diverging light back into a collimated beam, which can then be sent to a detector and measured. Due to fabrication imperfections the light exiting the chip will diverge at a slightly higher angle than the incoming light's convergence angle. Hence, the focal length of the external lens on the output side should be shorter than that on the input side.

### 7.3.4.2 Design of the on-chip lens

When the incoming light hits the front face of the chip it is focused only in the vertical direction. Hence, it is still as wide as the beam leaving the laser, approximately 3 mm. If we were to place the end of a 60 $\mu$m wide waveguide (which is a typical width for a multimode waveguide) at this point, only a very small part of the light would be collected. Therefore, instead of just coupling directly to the waveguide, we add another lens - this time to focus the light in the horizontal plane. Importantly, however, this second lens is made on-chip, during the same fabrication step as the waveguides and fluidic channels. This second, on-chip lens focuses the light into the waveguide. Once the light passes the air/SU-8 interface at the front of this internal lens, it starts to diverge out of the vertical focal point. It is, however, at this point (inside the chip) no longer necessary to worry about the light paths in the vertical direction as the chip guides the light due to the vertical layering of glass, SU-8 and PDMS (n=1.46, n=1.59, n=1.4-1.45 respectively). The chip guides light at incidence angles below 21.5°, and from Fig. 7.13 we see that the actual incident angle is only about 2°.

In order to make the on-chip lens both small and effective it is necessary to pay particular attention to the shape. Typically, a lens is cylindrical, defined by a single radius of curvature (see Fig. 7.14a). These types of lenses are, however, only effective for very small angles. Thus, if we want to focus the light relatively close to the lens interface (as is often the case in microsystems) we must adjust the shape of the lens. A first improvement of the lens would be to make it parabolic instead of circular (see Fig. 7.14b).

A third possibility is to tailor the lens by dividing the front face into small segments and then calculate the optimal slope and position of each segment (see Fig. 7.14c).
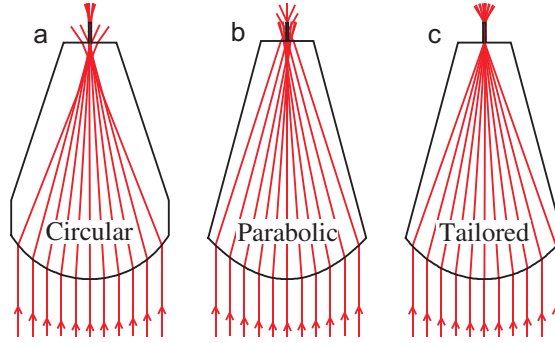


*Figure 7.14: This figure shows a raytrace simulation of 3 different lens designs. Each lens is 4 mm wide and 6 mm long. At the end of the lens a 60 μm wide waveguide is placed. It is obvious that the tailored lens outperforms the other two designs*

It is obvious from Fig. 7.14 that the tailored lens performs much better than the other two possibilities, even though the parabolic form is an improvement over the circular one. The reason why many cameras and refractive telescopes stick with using spherical lenses is that the tailored lenses are only optimized for one wavelength and are more complex and costly to fabricate. But as long as we only use one monochromatic light source and only need to tailor the lens in one dimension, the tailored lenses are easily implemented once the shape has been calculated.

To calculate the lens shape we must first define the necessary parameters. By default, we place the center of the curved lens surface at $(x, y) = (0, 0)$. The first feature of the lens, which must be defined, is the focal length ($f$). Assuming the lens faces downwards the focal point is denoted $(0, y_f)$ as shown in Fig. 7.15. Depending on the refractive index ($n$) of the chosen material the smallest effective focal ratio (lens width/focal length) will vary. Furthermore, it should be noted that, at short focal lengths, the angular dispersion of the light is larger. The refractive index of the material most also be known as it goes into the equations below.

Next, one must define the width of the lens, which in most cases should be made slightly larger than the laser spot. Finally, the number of horizontal segments ($N$) to divide the lens into must be defined and thereby also the segment width ($\delta$). Following these definitions the two $x$-values for each segment are known ($[i-1]*\delta$ and $i*\delta$, where '$i$' is the segment number), and the $y$-values can be calculated iteratively. The first step is to find the angle of incident ($\theta$) at the focal point from the center of the first segment. '$\theta$' is the angle at which light from the segment enters the waveguide. Assuming the angle of rotation ($r$) of each segment is so small that the vertical distance between the segment's end points does not significantly increase, we can find '$\theta$' using simple trigonometry (see Fig. 7.15).

**97**

$$\theta_i = \arctan\left(\frac{\delta(i - \frac{1}{2})}{y_f - y_i}\right) \tag{7.1}$$

where 'i' denotes the current segment number starting at the optical axis and moving outwards, '$\delta$' is the width of each segment and $f$ is the focal length. We note that $y_1 = 0$.

The next step is to use Snell's law to define the angle of refraction ($a$), as a function of the angle of rotation (see Fig. 7.15 insert).

$$a_i(r_i) = \arcsin\left(\frac{\sin(r_i)}{n}\right) \tag{7.2}$$

where '$n$' is the refractive index of the material and assuming the chip is surrounded by air. With this definition, we can use a numerical solver to find the value '$r_i$' that satisfies

$$r_i - a_i(r_i) = \theta_i. \tag{7.3}$$

Finally, we find

$$y_{i+1} = y_i + \delta \tan(r_i). \tag{7.4}$$

We then return to Eq. (7.1), increment '$i$' by one and do it all over again until all segments on the right-hand side of the lens have been calculated. Because of symmetry, the $y$-coordinates for the left-hand side segments are the same as those for the right-hand side.
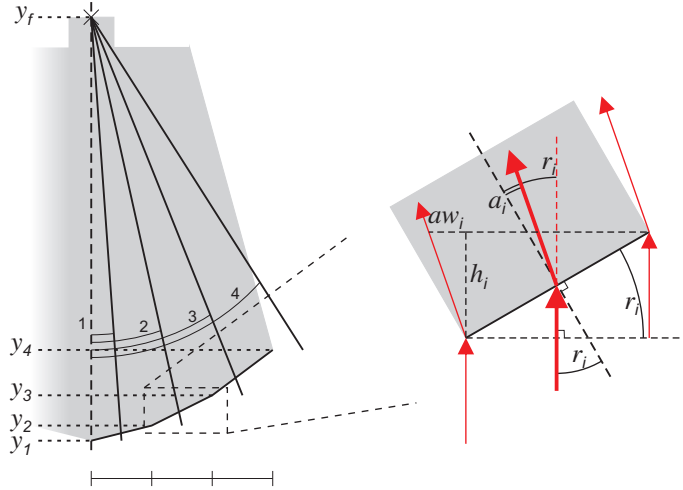


*Figure 7.15: This figure shows how to calculate the angle of rotation (r). First, one must find the angle of refraction (a) where the light changes media. Then, for each segment the angle of incidence (θ) at the focal point is found. From that, one must solve '$r_i - a_i = \theta_i$'. Notice that the segment width is greatly exaggerated in the sketch*

Since the curved lens is divided into many straight segments, all collimated rays hitting a single segment refract in the same direction and do not converge. Hence, the focus of

the light will never be any sharper than the width of a segment. Due to the light beam hitting each segment at an angle ($r_i$) and thus is progressing with an expanded width, the light beam will always be wider than the segment it passes through. Furthermore, the already expanded light from a segment also hits the focal point at an angle ($\theta_i$) with respect to the normal of the focal plane and therefore appears even wider. Following the insert of Fig. 7.15, one can express the added width ($aw_i$) of the lens segment 'i' as

$$aw_i = h_i \tan(\theta_i) = \delta \tan(r_i) \tan(\theta_i) \tag{7.5}$$

From Eq. (7.5) we see that the added width depends on '$\delta$' and on the angles '$r_i$' and '$\theta_i$'. As both these angles increase with the relative width of the lens, the added width can be regarded as dependent only on '$\delta$' and the relative width of the lens. Hence, the added width is always largest at the outermost segments of a lens.

In the lens shape calculation (Eqs. 7.1-7.4) a small error was introduced. This was due to the assumption made when calculating the angle '$\theta_i$' (see Fig. 7.15), where we assumed that the line segment would either be rotated about its center or rotated a very little amount only. This is, however, not strictly the case. In order to make a non-Fresnel type lens, each segment is rotated around its closest point to the lens' symmetry line. Hence, we ignored that the angle '$\theta$' is dependent on the value of '$r$' as the center of the segment is translated upwards with increasing '$r$'. The consequence of this error is that a beam of parallel light rays coming from a single segment no longer is centered at the focal point, but is shifted outwards by an amount given by

$$\text{Shift}_i = \tfrac{1}{2} h_i \tan(\theta_i) = \tfrac{1}{2} \delta \tan(r_i) \tan(\theta_i) \tag{7.6}$$

As the segments close to the symmetry line (the $y$-axis) are only rotated a very little amount ('$r$' is small), light from these segments is only shifted very slightly. But, as we move away from the symmetry line the angle increases and the shift becomes increasingly more problematic. Since the shift occurs in opposite direction on both sides of the optical axis the introduced error is actually twice that stated in Eq. (7.6). Interestingly, this makes the expression for the error introduced by the shift (Eq. (7.6)) and the added width (Eq. (7.5)) identical. Hence, similar as for the added width, the way to avoid the shift from becoming a serious issue is to ensure that the segments are small enough. To completely avoid the shift from appearing, the calculation of '$\theta$' must either be made through nested iterations, or the function $\theta(y)$ in Eq. (7.1) must be redefined as $\theta(y, r)$ instead. In Fig. 7.16, the width of the focal point of a tailored SU-8 lens is plotted as a function of the segment width $\delta$, and the relative lens width in units of focal length.
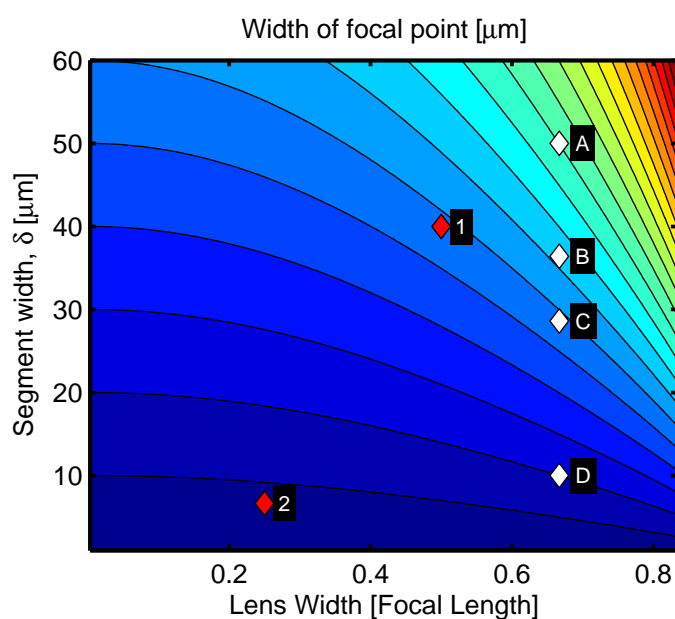
*Figure 7.16: This figure shows a contour plot of the width of the focal point as a function of relative lens width and the segment width, δ. The numbers here correspond to a refractive index of 1.59 (SU-8). The marks A-D correspond to the four similarly labeled cases depicted in Fig. 7.17. The marks 1 and 2 correspond to the design of the "rotation-chip" and "cytometer-chip", respectively (both described below). Color reprint in Appendix C*

From Fig. 7.16, we see that the broader the lens is relative to its focal length, the larger the width of the focal point becomes. Hence, if all the incident light is to be focused within a certain confined gap (such as a waveguide or sample chamber, for instance), then we must use a sufficiently small segment width.

Fig. 7.17 illustrates the performance of four lenses where different segment widths have been used, but which otherwise are identical.
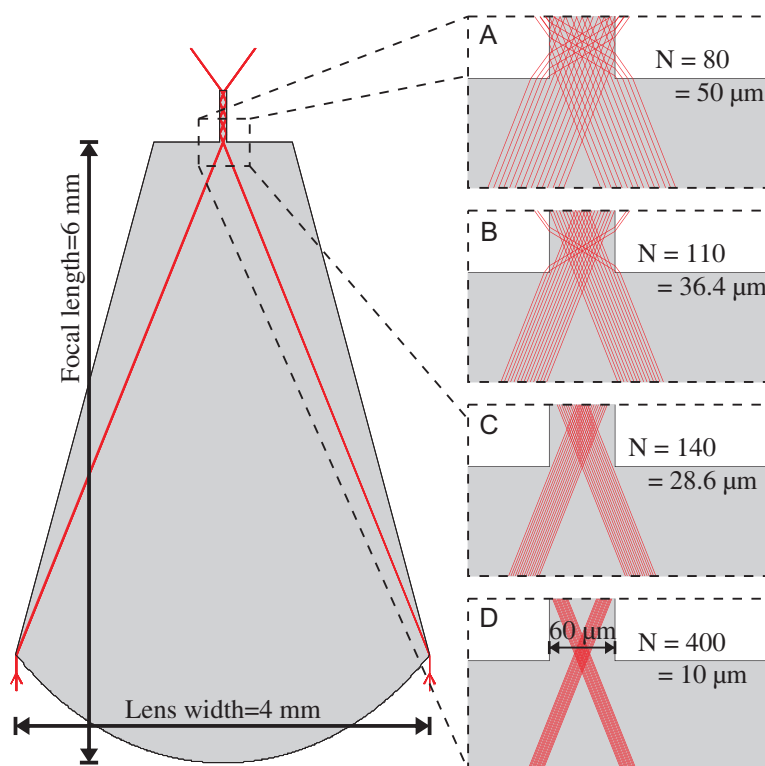
*Figure 7.17: This figure shows four raytrace simulations performed with an increasing number of lens segments, 'N' and decreasing segment width, 'δ'. Not surprisingly, we notice the performance of the lens improves when the width of segments gets smaller. Notice the four parameter sets are marked in Fig. 7.16*

Finally, now that all the incoming light is focused in a relatively small point, we either let the waveguide start from here, or we perform the desired experiment right at this location. As will be shown further down, the lenses work equally well in the reverse direction, i.e., if we need to collect light again for certain types of measurements. As long as the width of the output waveguide is sufficiently smaller than the lens, it can be regarded as a point source. This allows the lens to almost perfectly collimate the outgoing light in the chip plane.

## 7.3.5   EXPERIMENTAL

To verify the performance of the proposed lens concept, two different chips designs were developed. The first one was intended for testing the optical setup in general, while the second design was intended to work as a micro flow cytometer to show that the lens concept can be successfully implemented with a microfluidic network.

### 7.3.5.1   Chip designs

To test the setup and verify whether it was possible to transfer light from a collimated beam to a waveguide and back again to a more or less collimated beam in a reproducible manner, a "rotation-chip" was fabricated. The purpose of this rotation-chip was solely to test the optical performance and therefore no fluidic channels were added. To simultaneously test the reproducibility of the fabrication process, the rotation-chip was designed having rotational symmetry with an identical but separate test structure in each corner. Hence, by removing the chip, rotating it 90° and re-placing it again another structure would be illuminated. The structure of the rotation-chip is illustrated in Fig. 7.18. It was designed to have a tailored input lens 4 mm wide, with a focal length of 6 mm made from a total of 100 segments. Assuming a 3 mm wide laser beam, according to Fig. 7.16 this should result in a slightly less than 60 $\mu$m wide focal point. At the focal point, a 60 $\mu$m wide (75 $\mu$m high) waveguide was placed to guide the light over 5470 $\mu$m to a 90° bend. Exploiting the high refractive index of SU-8, a 45° SU-8/Air interface was used as a mirror. At the bend, the incoming and outgoing waveguides only share one common point, and two right isosceles triangles, one 60 $\mu$m wide and on 10 $\mu$m wide are added to complete the connection. The role of the small triangle is not to help guiding the light, but to prevent stress related cracks forming in the otherwise sharp corner. The design of the bend is shown in the insert of Fig. 7.18. The bend is included to prevent light coming from the laser from entering the detector directly. The outgoing waveguide is 6270 $\mu$m long and ends in the focal point of an output lens identical to the input lens.
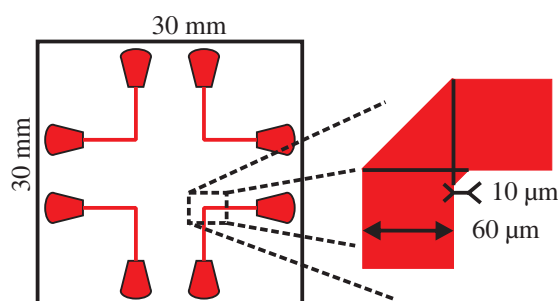


*Figure 7.18: This figure shows a sketch of the rotation-chip used to verify the performance of the optical setup. The high refractive index of SU-8 is used create sharp waveguide bends*

To show that this optical setup can also be combined with a microfluidic network, a micro flow cytometer was designed. Instead of focusing the incident light in a waveguide the "cytometer-chip" uses a tailored lens with 600 segments and a focal length of 12 mm to focus the light into the center of the 100 $\mu$m wide fluidic channel. According to Fig. 7.16, this should result in a beam width of $\sim$ 7 $\mu$m. However, through microscope inspection it was estimated that the true width of the focal point was 10-15 $\mu$m (result not shown), possibly due to fabrication and material imperfections. To avoid direct, unguided laser light reaching the detector a mirror structure (making use of an SU-8/air interface) is used to redirect the incoming light (see Fig. 7.19). On the other side of the channel, another

mirror structure (air cavity) is placed. This structure serves to deflect all non-scattered light to the sides. Light that is scattered more than approximately 11 degrees will not hit the second mirror and continue towards the output lens. The focal point of the 10 mm wide tailored output lens is 14.7 mm and is located 0.4 mm in front of the channel. This way scattered light from the channel will be focused about 20 cm from the chip rather than collimated. To reduce the amount of unintended (stray) light reaching the detector the middle part of the output lens was removed.
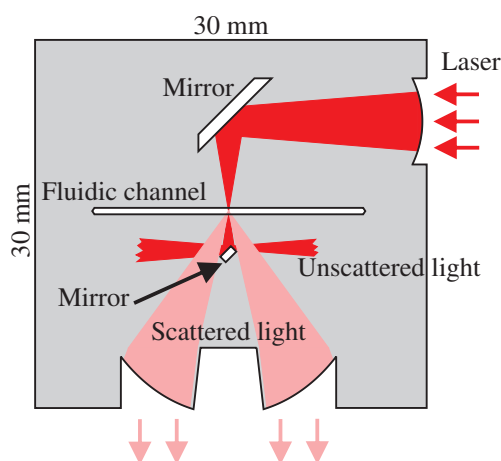


*Figure 7.19: A sketch of the optical part of the chip. The SU-8 layer (grey) acts as one big planar waveguide. Non-scattered light is separated from the scattered light using an SU-8 mirror. For illustrative purposes objects are not to scale with respect to each other. Color reprint in Appendix C*

### 7.3.5.2   Fabrication

Both chips were fabricated using a single standard UV-photolithography step to pattern a 75 $\mu$m thick SU-8 layer on a 500 $\mu$m substrate. A borofloat glass substrate was chosen for the cytometer-chip to ease microscope inspections. Silicon was chosen for the rotation-chip as it adheres much better to the small waveguide structures than glass does. After dicing, the SU-8 covered chips were aligned under a microscope to a cast PDMS lid, using alignment marks on both parts. This step is the only one where alignment is critical. If equipment for dicing the chips with high precision is available this step can be made much easier by constructing an alignment jig.

### 7.3.5.3   Chip-in-a-case

To make sure the chip can easily be positioned with sufficient precision, a holder and a case were constructed from PMMA using micromilling (see Fig. 7.20). The PDMS lid is cast such that an alignment structure extrudes in each corner. The extrusions extend beyond the footprint of the chip and two mm down. By making complementary holes in

the lower PMMA case part of the same dimensions, the elasticity/compressibility of the PDMS makes the alignment between PDMS and PMMA virtually perfect. A different set of PDMS extrusions ensures the alignment between the PDMS and the top case. These PDMS structures simultaneously work as O-rings around the fluidic connections. All fluidic connections are made using a custom-made fluidic connector manifold, which fits to both the top case and the PDMS O-rings. The connector nozzles are made 100 $\mu$m larger than the PDMS structures to ensure a proper seal. A cross section of one connection is shown in Fig. 7.20b. Once pressed into position the fluidic connector remains in place. The two PMMA case parts are fixed using three bolts. To ensure the distance between the case parts is reproducible and thereby also the compression of the PDMS, the case is equipped with custom made spacers. The final result is a chip-in-a-case that is fairly well protected from both dust and rough handling.
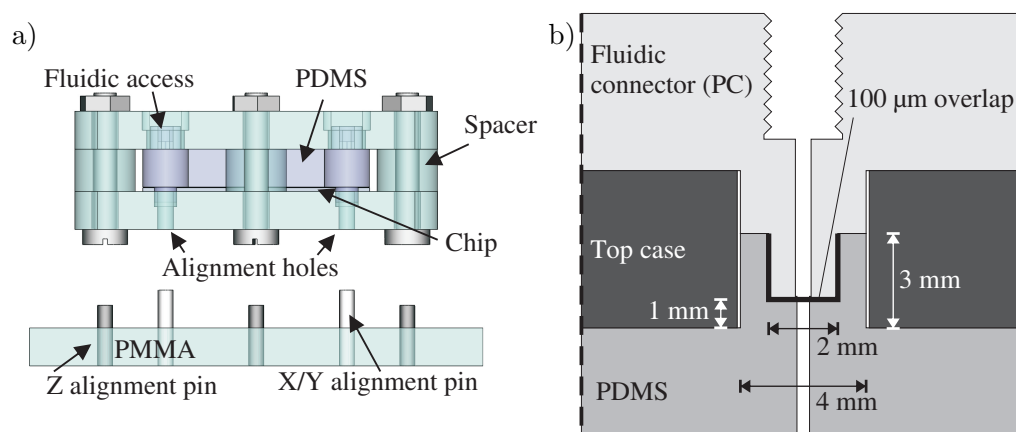


*Figure 7.20: Panel a shows a side view of the chip-in-a-case and the holder fitted with pins to aid the alignment. The bolts and the Z alignment pins are not in the same plane and hence not in contact. Panel b shows a cross section for one of the fluidic connections. The dimensions in the drawing refer to the PDMS object, the nozzle of the connector is 100 μm larger where indicated by the thick line*

On the top of the holder, a pattern of seven 2 mm holes are milled to an equal depth of 5 mm. In three of these holes, 8 mm tall metal pins are fitted. These three holes are placed as far from each other as possible, while still being able to fit under the case footprint and not conflict with the bolts. In the remaining four holes 10 mm tall metal pins are fitted. These four pins are also spread out under the footprint of the chip case. On the bottom side of the lower case part a pattern concentric to that of the four tall pins is milled to a depth of more the 2 mm. For pins with a diameter of 2 mm, a hole-size of 2.05 mm is comfortable. The chip-in-a-case can then be placed on top of the pins and gently be pushed into place. The four tall pins are now restraining the case from moving in the x-y-plane while the three short pins limit the movement in the z-direction. For the case around the rotation-chip, the four-hole pattern was made rotationally symmetric, allowing the chip-in-a-case to be placed in any of four possible positions. For the cytometer-chip,

pin symmetry was avoided resulting in only one possible placement position. Assuming that the laser, detector and the external lenses are all fixed relative to the chip holder platform, the chip-in-a-case can be exchanged in a matter of seconds without having to worry about the optical alignment.

## 7.3.6   RESULTS & DISCUSSION

### 7.3.6.1   Replacement experiment

In order to test the efficiency of the pin alignment system, the rotation-chip (inside its case) was repeatedly removed from the holder, rotated $90°$ and then placed back in the holder. Due to the transparency of the PDMS and the PMMA case it was immediately possible to see whether the rotation-chip had been re-placed correctly, as the waveguides would be glowing clearly (due to scattering losses from the waveguides). Therefore, in order to test the efficiency of the pin alignment system without any helping visual feedback, the laser was blocked whenever the rotation-chip was being removed or re-placed. This procedure was repeated over and over during a two-minute test while the transmitted light intensity was continually recorded. The plot in Fig. 7.21 shows the results from such a test.
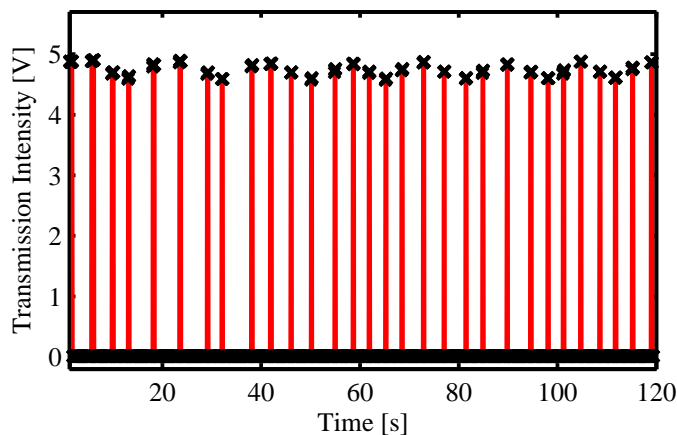


Figure 7.21: Data from a "cyclic" measurement, where the rotation-chip was rotated by $90°$ 30 times in a row, within 120 seconds

From the intensity trace for the transmitted light we see that a total of 30 rotations were achieved during the 120 seconds, i.e., only four seconds per replacement. The second thing we notice is that the transmitted intensity varies periodically in a four measurement cycle. This is obviously caused by performance differences between the four corners of the chip. The most likely reason for this difference is a small alignment inaccuracy between the SU-8 part and the PDMS lid. In Table 7.1 the obtained values are listed.

*Table 7.1: This table lists the data obtained during the replacement experiment. Each peak value is found by averaging the last 200 data points (200 ms) before the laser is blocked*

| Rotation angle | 0° | 90° | 180° | 270° | All |
|---|---|---|---|---|---|
| Cycle 1 [V] | 4.876 | 4.901 | 4.704 | 4.636 | |
| Cycle 2 [V] | 4.821 | 4.884 | 4.701 | 4.590 | |
| Cycle 3 [V] | 4.819 | 4.842 | 4.702 | 4.602 | |
| Cycle 4 [V] | 4.756 | 4.837 | 4.713 | 4.599 | |
| Cycle 5 [V] | 4.754 | 4.873 | 4.715 | 4.608 | |
| Cycle 6 [V] | 4.729 | 4.832 | 4.712 | 4.603 | |
| Cycle 7 [V] | 4.724 | 4.877 | 4.714 | 4.615 | |
| Cycle 8 [V] | 4.773 | 4.864 | | | |
| | | | | | |
| Average [V] | 4.782 | 4.864 | 4.709 | 4.607 | 4.740 |
| St. Dev [V] | 0.053 | 0.025 | 0.006 | 0.015 | 0.100 |
| St. Dev [%] | 1.106 | 0.509 | 0.129 | 0.319 | 2.111 |

When we look at the entire chip, i.e., all four corners together, we get an average output of 4.740 V with a standard deviation of 0.1 V, which is about 2 %. If we, however, look at each corner separately the standard deviation is greatly reduced by a factor between 2 and 16, yielding standard deviations between 0.1 and 1.1 %. The average value of 4.74 V corresponds to a measured power of approximately 1 mW or 20 % of the nominal laser output power. By removing the detector and projecting the transmitted light onto the laboratory wall 2.5 m away, we can determine the quality of the re-collimation. The resulting spot on the wall was rectangular in shape, 1 cm high and 4 cm wide. Hence, the vertical divergence half-angle is $\sim 0.1°$ and the horizontal half-angle is $\sim 0.5°$, which, in the authors' opinions, can be considered well collimated.

### 7.3.6.2   On-chip cytometry

To test the cytometer two series of measurements were conducted. One series was based on 1 $\mu$m polystyrene particles and the other on 2 $\mu$m polystyrene particles (Polysciences Inc, 07310-15 and 19814-15). During each measurement the intensity of the scattered light was recorded for 60 seconds using a sampling frequency of 80 kHz. For each measurement, a pre-calculated concentration of particles was injected at a flow rate of 20 $\mu$L/min using a syringe pump (Harvard Apparatus, PHD 2000). Hence, the number of particles passing the cytometer in 60 seconds was known (assuming no significant handling errors and losses). Milli-Q water filtered through a filter with a 220 nm cut-off was used to prepare the particle suspensions.

The results of the two measurement series are plotted in Fig. 7.22. The two plots show the relation between the number of injected particles and the number of counted particles. It can be seen from the figure that when counting 1 $\mu$m particles, the maximum particle flux before a deviation from the linear behavior is observed is somewhere around 6000 particles/min. For 2 $\mu$m particles the flux can safely be doubled to around

12000 particles/min. These count rates correspond to concentrations of 300 particles/$\mu$L and 600 particles/$\mu$L, respectively. Currently, it is not conclusively understood whether these limitations stem from the chip/setup or the data treatment. For the data shown in Fig. 7.22, the particle induced peak height detection threshold has been calibrated once for each particle size.
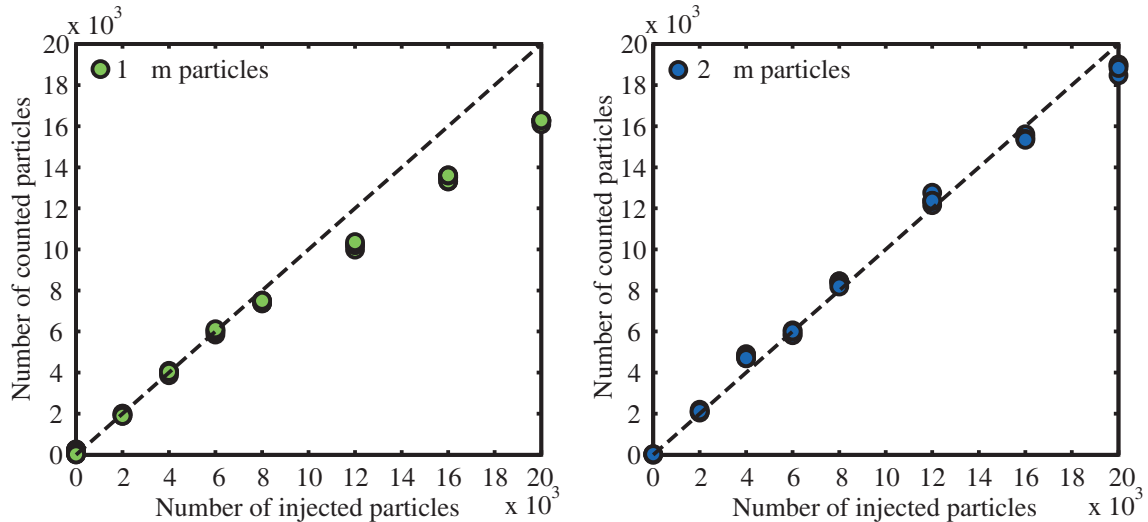


*Figure 7.22: The two plots show the relation between the number of injected particles and the number of counted particles. In both measurements the numbers start to divert from the 1:1 ratio when the concentration of particles becomes too large. The onset happens much earlier for the 1 $\mu$m particles than for the 2 $\mu$m particles.*

### 7.3.6.3   Drift issues

Though the proposed method works very well, there is a small but noticeable problem related to the focusing effect of the lens system. It appears that when light is focused sufficiently the bulk SU-8 material (of the lens or waveguiding structure) starts to heat up. As a result, a non-permanent (transient) positive change in transmission intensity can be observed. As the chip continues to heat up, the effect becomes less and less pronounced. As a consequence, the transmitted base line is not flat, especially not during the first few seconds. Hence, the system suggested here may not be useful for applications that rely on short light pulses for their detection purposes rather than a continuous light source. There are several ways to counteract this effect. The simplest solution is to use a less powerful light source. This may not completely eliminate the problem, but should certainly reduce it. Another solution could be to use a different and less absorbing polymer (or a longer wavelength) than the SU-8/red laser light combination used in this study. A third method could be to use a reference waveguide/output. Similarly, it should also be possible to compensate for the drift mathematically using appropriate calibration curves.

### 7.3.7   CONCLUSION & OUTLOOK

We have shown an easy approach to building a virtually alignment free optical setup that can be used for many different microfluidic applications. The proposed setup is especially suited for chips machined using photolithography as the fabrication of the on-chip lens is not requiring additional manufacturing steps in such cases. Using this approach, it is possible to fabricate chips that can be plugged into the setup in a matter of seconds and with a standard deviation for the transmitted light at about 2 %. The ability to collimate the light as it exits the chip makes this setup very convenient. Even though the setup is based on bulk optics it can easily fit inside a shoebox-sized instrument. Given the low loss of light it becomes possible to use low powered lasers.

Furthermore, we have successfully implemented the proposed lens system on an on-chip cytometer, which can either function as a stand-alone device or be implemented as part of a larger LOC system. Since this cytometer chip does not rely on complex flow focusing schemes it is very stable and easy to use. It is, however, dependent on calibration. We have demonstrated that particles down to 1 $\mu$m can be detected and counted reliably at 100 Hz for concentrations below 300 particles/$\mu$L. It has been demonstrated how the on-chip lenses can be used both for focusing the light directly at the point of detection or to couple light in and out of waveguides. This versatility allows the lens system to be advantageously implemented in many other microdevices exploiting light-based detection schemes (absorption, fluorescent, etc.).

Future work will strive towards exploring the possibilities of micromilling all optical surfaces for a future low cost instrument which is not dependent on relative expensive cleanroom fabrication techniques. Since many optical detection devices rely on very small singlemode waveguides, will it also be interesting to test how small waveguides are useful when coupling light using the proposed method.

### 7.3.8   ACKNOWLEDGEMENT

—————————————— End of manuscript ——————————————

## 7.4   Additional materials

### 7.4.1   Shift-free tailored lens

As mentioned in Section 7.3 the design of the tailored lens can be further optimized to remove the shift-error by including the dependence of the rotation angle, 'r', in the definition of $\theta$. The fully optimized tailored lens can be generated using the Matlab function shown here:

```matlab
─────────────── Matlab ───────────────
1  function [x,y] = TailoredLens(FocalLen,LensWidthHalf,RefIndex,NSegments)
2     x=linspace(0,LensWidthHalf,NSegments+1);              % define x-array
3     y = zeros(size(x));                                   % prepare y-array
4     delta = LensWidthHalf/NSegments;
5     for i=1:NSegments
6         SumDelta=(i-0.5)*delta;                 % X-dist from sym-axis to center of seg.
7         r(i) =fzero(@(r)r-asin(1/RefIndex*sin(r)) ...
8                              -atan(SumDelta/(FocalLen-y(i)-0.5*delta*tan(r))),1);
9         y(i+1)=y(i)+delta*tan(r(i));
10    end
11 end
```

This function only generates the coordinates for a half lens. The four input arguments needed are the focal length of the lens, the width of the half lens, the refractive index of the lens material and the number of segments in one lens half. If medium surrounding the lens is different from air, the number '1' in line 7 should be substituted by the refractive index of the medium.

To illustrate the difference between a tailored lens with and without the shift correction, the plots in Fig. 7.23 show the difference between the y-coordinates of each lens segment. Fig. 7.23a shows the case of the lens used on the cytometer-chip. For this lens the change is very minute and within the range of the fabrication tolerance. Fig. 7.23b shows the case of the lens used for the rotation-chip. Because of the much shorter focal ratio and the lower number of segments the difference is far greater in this case. Notice the y-scale for the cytometer-chip in Fig. 7.23a is given in nanometers.
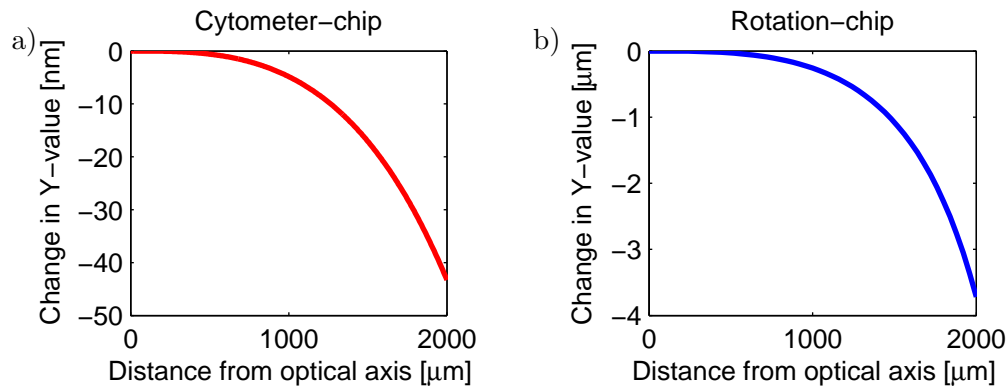


Figure 7.23: These plots show the effective change of the y-coordinates of the tailored lens when correcting for the shift. Panel 'a' shows the effect on the lens used for the cytometer-chip. Panel 'b' shows it for the rotation-chip. Notice that the y-axes differs by a factor of 1000

The performances of the shift-corrected lenses have only been verified with ray tracing, as they have not yet been used in the lab. Even though the difference between the corrected lenses and the original ones is very small and the resulting effect of the correction perhaps is unmeasurable, I see no reason not to design future lenses as the corrected version.

### 7.4.2 System characterization

#### 7.4.2.1 Effect of a rotational misalignment

With the use of fiber free chips, it becomes very important to avoid rotational misalignments between the chip and the incident laser beam. In normal use this is not a concern as the pin aided alignment of the chip-in-a-case prevents the chip from rotating. It does, however, put a certain quality restriction on the chip assembly process during the fabrication. When sealing the chip with the PDMS lid the two are manually placed on top of each other. As mentioned earlier, this step is the only one where the alignment is very critical. First of all, the positions of the fluidic inlets have to match each other. But as these are relatively large (approximately 100 $\mu$m and 200 $\mu$m) it is possible to slightly rotate the chip while still connecting all inlets. In Fig. 7.24 the effect of a chip being rotated 15° and 0.24° is illustrated.
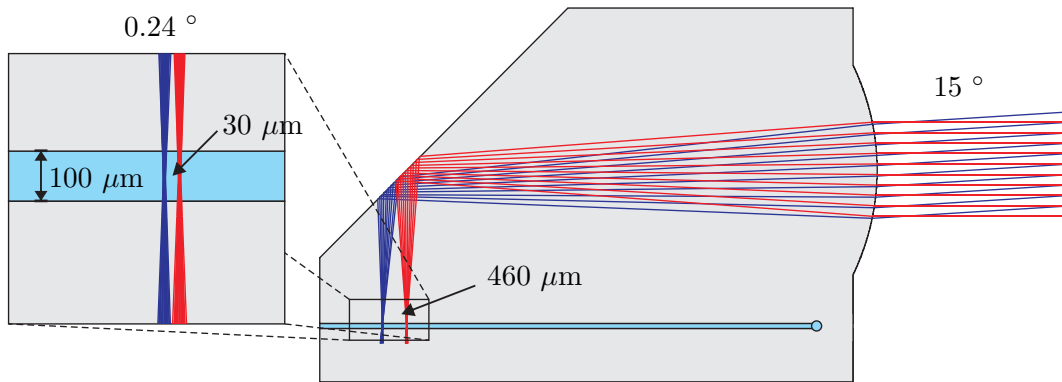


*Figure 7.24: This figure shows two ray tracing results; a rotational offset of 15 ° results in a 460 $\mu$m displacement of the focal point, and an offset of 0.24° gives an offset of 30 $\mu$m*

With the cytometer-chip the main channel is 24 mm long and it is estimated that, when using a microscope, it is fairly possible to position the fluidic inlets in each end with 100 $\mu$m precision. Hence, when carefully assembling the chip the estimated rotational offset is within

$$\text{degrees of rotation} = \arctan\left(\frac{100\,\mu m}{24\,mm}\right) = 0.24°. \qquad (7.7)$$

According to the ray trace simulation shown in the insert in Fig. 7.24 this rotation results in a 30 $\mu$m offset. Given the design of the cytometer-chip, all unscattered light is still redirected by the secondary mirror, hence the misalignment is within the acceptable range.

#### 7.4.2.2 Switching between two different chips

In Section 7.3 I discussed the replacement experiment. In that experiment only a single chip was used. In order to show that the developed setup actually supports switching between multiple chip a second experiment was conducted.

The initial idea was to switch back and forth between four chips. However, it turned out that the 5 mm PMMA substrates used for the chip cases could vary a lot in thickness, so in order to maintain a similar laser alignment the four chips had to be tested two and two instead. This issue is, of course, not related to the concept of the setup, but rather a consequence of the low quality of the PMMA substrates. Each group of chips consisted of one rotation-chip and one additional test-chip. The extra test chip was made similar to the rotation-chip, except that the corners would have 3, 5 and 7 bends instead of just one. The last corner would consist of three small parallel waveguides rather than one larger. Hence, the four corners of the second chip were expected to give four different outputs, all lower than the output of the rotation-chip. The tests was conducted by first placing the rotation-chip and rotating it through all four positions (1,2,3,4) while recording the transmitted intensity at each position. Then the second test chip would be cycled through its four positions (5,6,7,8) before returning to the rotation chip again. In total 5 cycles (position 1-8) were done with the first chip pair and 4 cycles with the second pair. The results are shown in Fig. 7.25a and Fig. 7.25b, respectively.
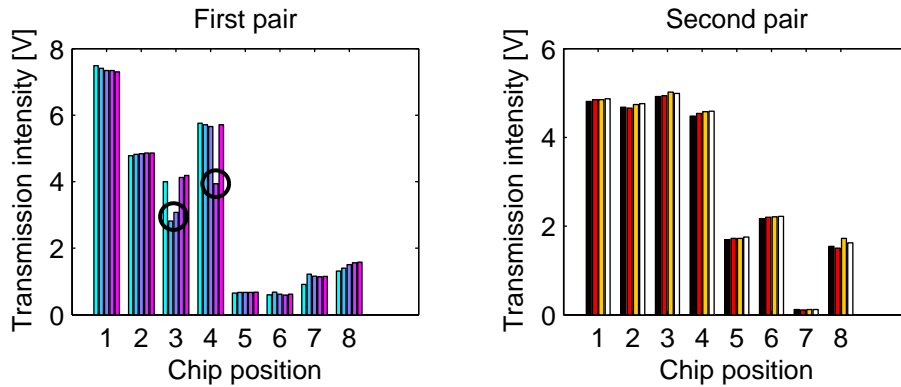


*Figure 7.25: These plots show the reproducibility of the transmission intensity as the chips are rotated. Position 1-4 is the rotation-chip and position 5-8 is from a second test chip, with non-identical corners. Except from the three errors, which are marked with circles, the result is very good*

The important thing to notice with these results is the reproducibility among each individual position. Except for three clearly misplaced points (these are marked in Fig. 7.25a), all other points lie within a very close range of each other. Hence, this experiment clearly demonstrates that it is possible to switch back and forth between several chips without loosing the alignment.

Furthermore, one may notice the lack of reproducibility from chip to chip or even from one corner to the next. This is because of bad alignment between the PDMS part and the chip. The chips used for this experiment were made with silicon substrates, to improve the SU-8 adhesion, rather than the glass substrates otherwise used. This meant that these chips could not be aligned using the method explained in Section 7.4.2.1 as they were not transparent. Hence, the alignment (both rotational and translational) was much worse on these chips.

When performing experiments like these, that serve to somewhat quantify the user-friendliness of the system, it is obviously misleading if the tests are performed by the same people how built the setup and who worked with it every day during many months (or years). This is why I recruited two of my fellow coworkers, Noemi Rozlosnik and Stephan Urs Keller, to perform these measurements during an institute team building event. Hence, both the experiments presented here, and the rotation experiment from Section 7.3.6.1 were performed within two hours by two persons with no prior knowledge of the setup.

Furthermore, tests like these could easily be repeated over and over until the wanted results were achieved. So to avoid getting a biased result these tests were only performed once, with the result as shown above. The rotation test was, however, performed twice as the first attempt ended with the chip accidentally getting dropped.

### 7.4.2.3   Parameter scaling

When performing any kind of test (or work in general) it is in most cases a goal to do it as fast as possible. With the sixth generation setup the previously used PMTs were substituted by a single photo detector, which meant that data would only be recorded from a single source, rather than two or four (PMTs and band pass filters). Hence, it was possible to increase the sampling rate by a factor of four from 20 kHz to 80 kHz. Running the experiments at an increased sampling rate meant that each peak would be defined in much better resolution. However, the total number of data points would also increase, causing the computer's memory to overflow much faster. Having already improved the memory handling of my LabVIEW data acquisition program several times, the program was able to collect data at 20 kHz for 14 minutes (16.8 million data points) and manage to save the data afterwards. So, when sampling at 80 kHz the maximum test time would be limited to approximately 3 minutes.

Being limited in time also means being limited in the total number of particles passing through the setup. If 3D focusing had been successfully implemented this would not be as much of a concern as the peaks would be separated from the baseline noise, but without the focusing the process of counting becomes more statistically dependent. Hence, the precision of the result depends on the total number of particles passing through the system. Therefore, it is not a good idea to use the increased sampling rate to further improve the signal resolution. It is much better used by increasing the flow rate with the same factor, hence keeping the peak resolution the same level (13 points for the 6th gen).

In order to verify if it was possible to obtain the same results after increasing the sampling and flow rate and decreasing the measurement time a series of tests were performed. The parameters used for the six different tests are listed in Table 7.2.

*Table 7.2: The list of parameters used for the scaling tests*

| Test # | Particle size | Flow rate | Sampling frequency | Time | Multiplier |
|--------|---------------|-----------|--------------------|------|------------|
| A1 | 1 $\mu$m | 5 $\mu$L/min | 20 kHz | 60 s | 10 |
| B1 | 1 $\mu$m | 5 $\mu$L/min | 20 kHz | 600 s | 1 |
| C1 | 1 $\mu$m | 20 $\mu$L/min | 80 kHz | 150 s | 1 |
| A2 | 2 $\mu$m | 5 $\mu$L/min | 20 kHz | 60 s | 10 |
| B2 | 2 $\mu$m | 5 $\mu$L/min | 20 kHz | 600 s | 1 |
| C2 | 2 $\mu$m | 20 $\mu$L/min | 80 kHz | 150 s | 1 |

The test was performed separately for 1 and 2 $\mu$m particles. To illustrate the influence of a high number of particles, tests A1 and A2 were performed in 1/10th of the time, the obtained result was afterwards multiplied by 10 in order to compare with the other results. Fig. 7.26a shows the resulting peak height histograms of the 1 $\mu$m tests and Fig. 7.26b shows the results from counting the 2 $\mu$m particles. The full length tests B and C were all performed three times.
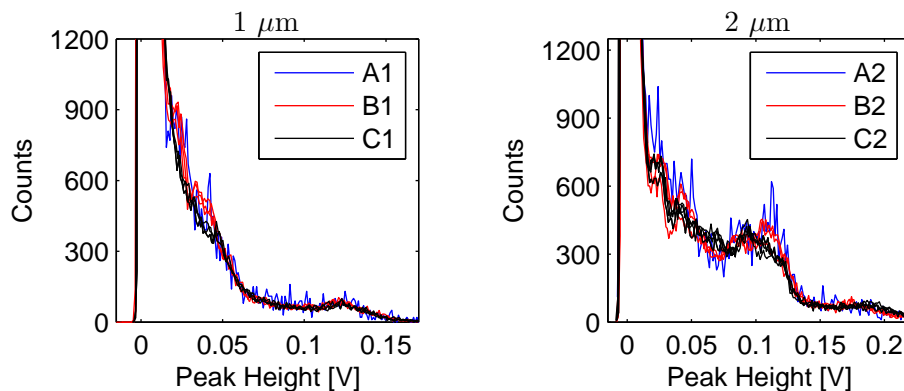


*Figure 7.26: These plots show that the shape of the peak height histograms is independent of the scaling of parameters. In both the 1 and 2 $\mu$m plots, shown left and right, respectively, all results fall very close to each other. The result from the short A-tests is seen to fluctuate much more than the rest, due to the relative low number of counts. For illustrative purposes the histograms are here shown as line-plots instead of the more conventional bar-plots*

Looking at the results plotted in Fig. 7.26 it is immediately obvious that the result from both the A-tests fluctuates a lot, a clear consequence of the short test time. Secondly, it is noticed that beside the fluctuation the results are all very similar. Hence, it can safely be concluded that the system performs identically when the parameters are scaled evenly. It is simultaneously concluded that the LabVIEW recording works as intended.

It is noted that this kind of scaling only works within the limits set by the employed equipment. It has, for example, been necessary to lower the level of amplification on the photo detector from 70 db to 50 db, in order to be within the range of the device.

### 7.4.2.4  Cytometer realignment test

Until now it has been demonstrated that the sixth generation setup can be used for both a cytometer chip and for fast and reproducible replacements of the rotation-chip. The purpose of the demonstration illustrated in Fig. 7.27 is to show that the cytometer chip can be easily picked up and repositioned as well.

This test was conducted in a similar way as any of the other cytometer tests. The cytometer-chip inside its case was placed in the setup and the fluidic connector was positioned on top. A solution of 1 $\mu$m particles was injected through the original outlet using the remaining five connections as outlets. While the particles passed through the cytometer-chip the intensity of the scattered light was recorded. During this test the Chip-In-a-Case with the attached fluidic connector was repeatedly lifted and repositioned. Hence, when the chip was lifted the optical path was interrupted while the fluidic path remained un-affected (touching the tubing and moving the chip around in general will, of course, introduce minute flow fluctuations, but these we neglect in this case). Due to the direction of the incident laser beam being perpendicular to the field of view of the optical detector, the recorded light level drops to the ambient level whenever the chip is lifted. From the raw data plotted in Fig. 7.27 it is seen how the measurement of the particles repeatedly continues every time the chip is repositioned.
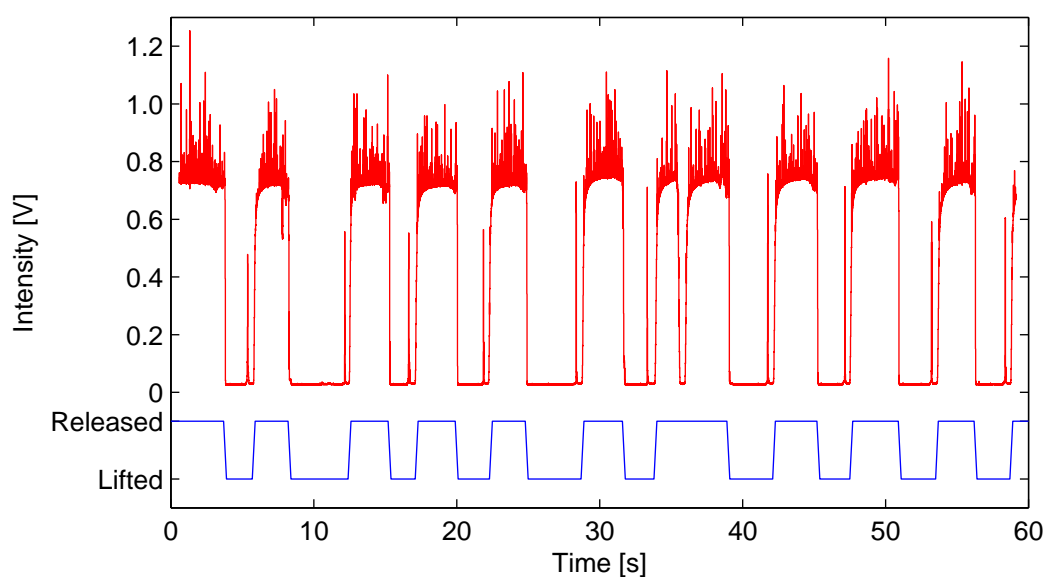


*Figure 7.27: The upper line shows the recorded data of a measurement performed on 1 $\mu$m particles. The lower line shows when the chip was lifted and repositioned. The data shows that the measurement rapidly resumes when the chip is reinserted in the setup. Notice the fluidic connection were left in place while the chip was lifted. During the 60 seconds of the measurement the chip was lifted 10 times*

Below the data, a second line has been plotted which indicates the approximate state

of the chip. When comparing the state of the chip to the data, it is noticed that right before the chip is repositioned a small sharp peak is seen. This peak is caused by an internal reflection in the lower PMMA case, which crosses the laser beam when the chip is positioned.

The result of this experiment shows that the chip can be lifted and repositioned 10 times in 60 seconds. This indicates that the proposed method of aligning the setup is very accurate, and is considered a huge advancement compared to the previously used fiber based solution.

### 7.4.2.5   Beam size

According to the calculations given in Section 7.3 the width of the beam crossing the microfluidic channel in the cytometer-chip should be approximately 7 $\mu$m. The microscope pictures in Fig. 7.28 show the beam in three different cytometer-chips all with the same lens geometry. These pictures were obtained by filling the channel with red food color. By comparing the width of the beams to the width of the channel (which we know is 100 $\mu$m), these pictures indicate that the actual beam width is slightly bigger than expected, namely 10-15 $\mu$m.
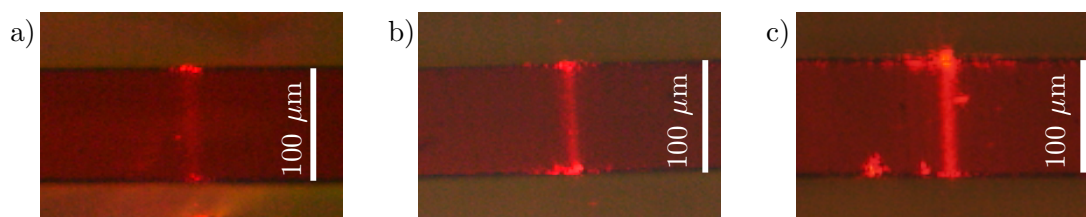


*Figure 7.28: These pictures show the actual beam width of the cytometer-chip to be 10-15 $\mu$m. The varying brightness is caused by ageing of the SU-8 which becomes increasingly opaque over time. The youngest chip, shown in Panel c, has been used extensively for more than two months*

The reason the beam is wider than calculated is most likely due to fabrication and material imperfections. This test shows that it is possible to fabricate these lenses in a reproducible way, and that it is possible to obtain not only a sharp focus but at a very high focal ratio (f/12), which in principle makes it possible to obtain a thin wall of light across an even wider channel than the 100 $\mu$m used here. This also means that the design presented here can be further optimized by reducing the size of the secondary mirror, thereby lowering the angle of the scattered light reaching the output lens and eventually the detector.

### 7.4.3  Setup Considerations

#### 7.4.3.1  Mixed particles

As it was also noticed with the 5th generation chip, there is an obvious difference in the shape of the peak height histogram between 1 $\mu$m and 2 $\mu$m measurements. This can for instance be seen from the plots in Fig. 7.26. In Fig. 7.29 the peak height histograms, from a measurement of only 1 $\mu$m particles and another measurement with a mixture of both 1 and 2 $\mu$m particles, are shown. Since there is an obvious difference, it is natural to assume that this difference can be exploited to distinguish mixtures of the two particle populations. The most concrete difference between the two shapes is the first positive peak height value at which the count reaches zero. This value corresponds to the maximum 'reasonable' peak height. At closer examination, the count-value can be seen to reach zero several times, as there are many individual events spread out at higher values. These are assumed to originate from doublets and dust particles, and since these events only appear in very low numbers separated from the main population as well as from each other, they are assumed negligible.
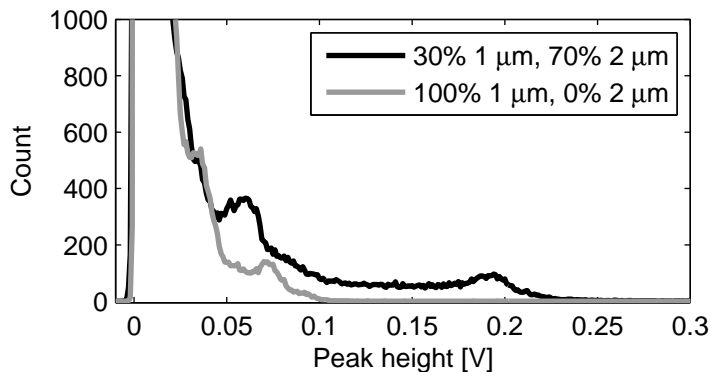


*Figure 7.29: This plot illustrates the different shapes of the peak height histograms for varying particle populations. By noticing that the 1 $\mu$m particles have a maximum peak height at approximately 0.1 V, we assume that all peaks above this value are caused by 2 $\mu$m particles. Hence, by counting peaks higher than 0.1 V we can extract the concentration of 2 $\mu$m particles, provided that the chip has been calibrated*

Looking at the histograms in Fig. 7.29 it is clear that the histogram for the pure 1 $\mu$m solution has a maximum peak height at approximately 0.1 V. Hence, for the mixed histogram we assume that all peaks above this value must originate from the 2 $\mu$m particles. Comparing the count-value above the 0.1 V threshold to the value from measurements performed only with 2 $\mu$m particles we can deduce the relation presented in Table 7.3. By definition the solution consisting of only 2 $\mu$m particles is 'estimated' to 100%. Each of the presented values are based on the average result of three measurements. The result of this test shows a monotonically increasing estimate for increased concentrations of 2 $\mu$m particles. Furthermore, the estimated amount of 2 $\mu$m particles appears to be independent on the concentration of 1 $\mu$m particles.

Table 7.3: *This table lists the different combinations of solutions used for the mixed particles test. The fourth column shows the estimate of 2 µm particles based on the data recorded during testing. A 100 % solution corresponds to 1000 particles/µL*

| Pure water | 1 µm solution | 2 µm solution | Estimate of 2 µm |
|:---:|:---:|:---:|:---:|
| 30 % | 0 % | 70 % | 54.46 % |
| 0 % | 30 % | 70 % | 54.89 % |
| 0 % | 50 % | 50 % | 46.8 % |
| 0 % | 70 % | 30 % | 31.8 % |
| 0 % | 100 % | 0 % | 0.5 % |
| 30 % | 70 % | 0 % | 0.1 % |

Even though the estimated amount does not seem to linearly fit to the injected concentration, it might still be good enough to detect changes in the concentration of the larger particles. It might even be possible to use a calibration curve to artificially remove the nonlinear response. This can, however, not be assessed without further testing. The ability of being able to extract an estimate of the concentration of the larger particles is very interesting seen from the perspective of the DetectHIV project, where the concentration of doublets directly relates to the presence of HIV. This could mean that this chip perhaps could be implemented and work without any kind of flow focusing. It is, however, expected that the signal from 1 µm doublets will be slightly lower than the signal from 2 µm particles, thereby possibly decreasing the sensitivity of this measurement even further. But considering that this presented cytometer-chip is a prototype, it is likely that it can be even further optimized. Hence, using this kind of detection scheme, would make the design and use of the integrated DetectHIV-chip much simpler. By removing the necessity for 3D focusing the number of inlets and required pumps greatly reduces. Furthermore, having only one channel in the cytometer-chip makes it possible to drive the flow using suction, which would remove the necessity of the on-chip valves. This could all in all result in a chip, which might yield a lower sensitivity than with 3D focusing, but which would be much simpler to fabricate, operate and which could be used with a much simpler instrument (fewer pumps and no valve actuators).

### 7.4.3.2   Low cost laser

Having realized that the entire DetectHIV setup perhaps could be severely simplified and already having cut the necessity of two 1100 EUR PMTs down to a single 300 EUR photo detector, I decided to do a small test to check how much the quality of the laser source was influencing the measurements.

The laser normally used in this setup is a Diode LabLaser (VLM2, 31-0144-000, Coherent), that comes with a price of more than 1500 EUR. So, to try something different I ordered a nameless 10 mW red laser module on eBay for only 6.5 USD. To be fair, this laser module did not include a power supply, but with an operating voltage of 3-4.5 Volts, a standard power supply was used. The cheap laser was fitted in the holder and a measurement with 1 µm particles was made. A data sample from this experiment is

shown in Fig. 7.30a. For easy comparison a similar plot from a measurement with the more expensive laser is shown in Fig. 7.30b.
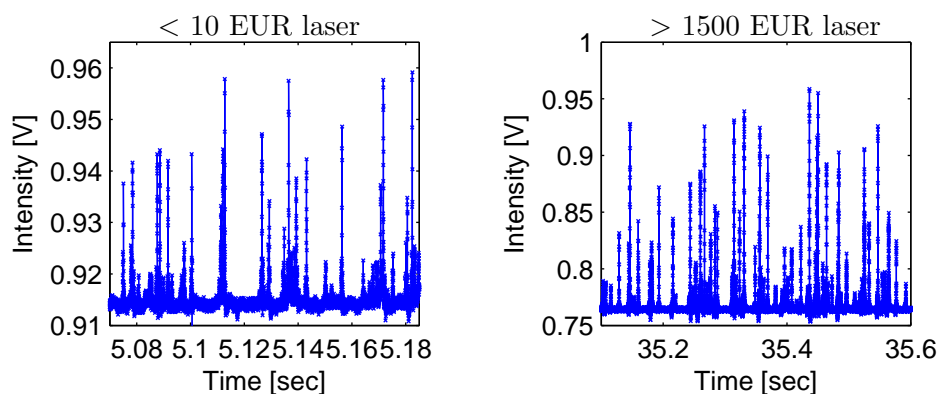


*Figure 7.30: Panel 'a' shows a data sample obtained from a measurement with a low cost laser. It is clearly seen from this plot that the passing 1 μm particles are easily detected. Panel 'b' shows a data sample obtained with the usual expensive laser. Comparing the two data samples, we can see the signal to noise ratio has only decreased approximately four times while the laser cost is lowered more than 100 times*

First of all, we notice that the individual 1 $\mu$m particles do get detected very easily by the cheap laser. However, a closer inspection reveals that the signal to noise ratio has decreased by a factor of approximately four. The wavelength of the cheap laser was measured to 664 nm compared to the 635 nm of the normal laser, which means that the on-chip lens is not perfectly optimized for the cheap laser. Furthermore, the beam width of the cheap laser was noticeably larger, which might also lead to a reduction of the signal strength. But to conclude on this minor test, the cheap laser module was found to perform surprisingly well. Furthermore, this test serves to demonstrate that the results obtained for the 6th generation chip do not rely on using high quality equipment like lasers and PMTs. It is, of course, obvious that higher quality equipment is an advantage, but if the cost/benefit balance is considered with respect to a possible commercialization, it seems reasonable to look for a cheaper lasing solution.

### 7.4.4 Other uses of the optical setup

#### 7.4.4.1 Cells

This first example of other uses is a demonstration of the possibility to detect cells. Though this test in principle is identical to everything mentioned above, it is presented here to illustrate the point that the cytometer chip works on other 'particles' than those made of polystyrene.

For this demonstration an ordinary block of household yeast-cells from the local supermarket was diluted and injected through the chip. The data sample from the result is shown in Fig. 7.31a. The data from the cell measurement is shown in blue (light) while, for

easy comparison, a regular 1 $\mu$m polystyrene particle measurement is plotted in black. In Fig. 7.31b, a microscope image of the cells is shown. The insert shows an 11 $\mu$m particle, which indicates that the cells measure approximately 3-5 $\mu$m.
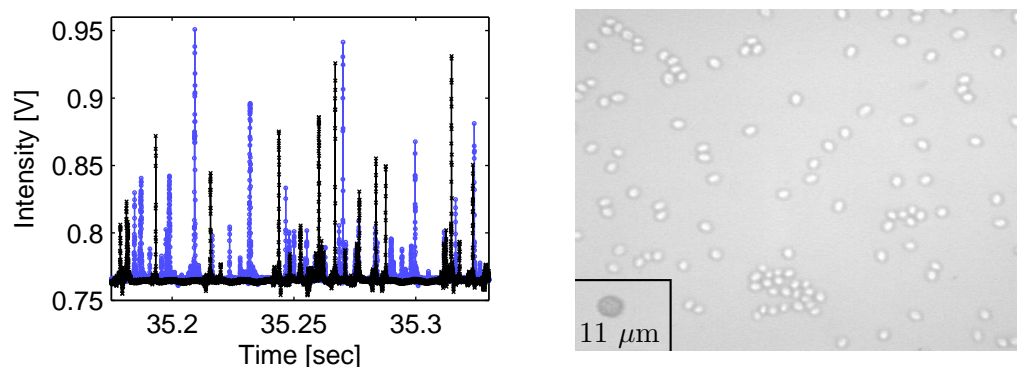


*Figure 7.31: Panel 'a' shows a data sample from a cell measurement (blue,light) and a data sample from a 1 $\mu$m polystyrene particle measurement (black). The signals are found to be of comparable size. Panel 'b' shows a microscope picture of the used cells. Compared to the 11 $\mu$m particle in the insert, the yeast cells are estimated to be 3-5 $\mu$m*

From Fig. 7.31a, we see that the signal from the cells is comparable to that of the 1 $\mu$m particles. Though the cells are larger than the particles, it makes sense that the signals are similar, as the refractive index of the cells is possibly much closer to that of water.

#### 7.4.4.2   Absorption

To show that this optical setup combined with microfluidics can be used for other applications than cytometry, a simple absorption measurement was performed using a specially designed absorption chip. The layout of the absorption chip is shown in Fig. 7.32. Each chip measures 30 mm x 30 mm and contains two devices. Hence, the input lens is positioned at the exact same spot as for the earlier described rotation-chip, making it possible to quickly switch back and forth between the two.
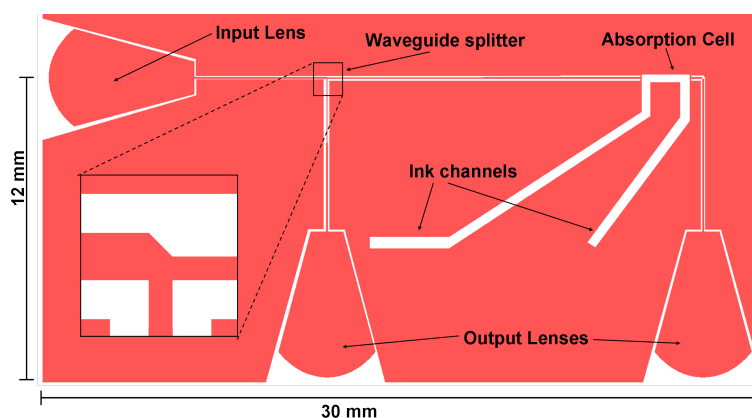
*Figure 7.32: This figure shows the design of the absorption chip. This chip is fitted with two output lenses; the left is used as reference*

To account for any variations in the in-coupled light this chip was made with two output lenses. One lens (the left one in Fig. 7.32) is intended for the reference measurement and the other lens for the absorption measurement itself. By evaluating the difference between the reference and the output, the measurement becomes independent on variations in the incoming light. In order to measure the light from two sources simultaneously the detector was replaced by a piece of paper, onto which the light from the two outputs was projected. The dots on the paper were then photographed using an immobilized digital SLR camera (Canon, EOS 450D). Through image processing the ratio between the two dots was found. Before the measurement six syringes were prepared with different ink solutions, 0 %, 4 %, 8 %, 12 %, 16 %, and 20 %, respectively. One by one, each solution was injected into the 2000 $\mu$m x 350 $\mu$m x 75 $\mu$m absorption cell and five consecutive images were recorded. For the five solutions containing ink, the measurements were repeated twice. In Fig. 7.33 the results are shown:



*Figure 7.33: This figure shows the data from the absorbance measurements. Each of the ink solutions was measured twice. From this plot we can easily see the expected relation between increased concentration and decreased transmission*

The results in Fig. 7.33 clearly reveal the expected correlation between increased concentration and increased absorption. Hence, they are presented here to serve the purpose of demonstrating the flexibility of the optical setup based on tailored lenses.
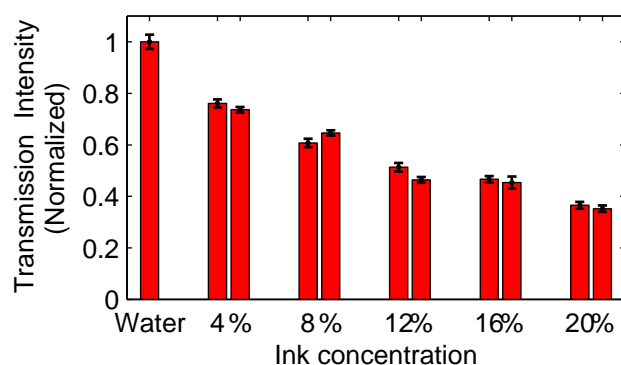
### 7.4.4.3   Using the cytometer as a flowmeter

One of the considered solutions to obtain a functional three dimensional focusing is to use hydrostatic pressure to drive the flow. With a channel configuration that only requires one buffer inlet and one sample inlet, it may be useful to drive the flow with gravity. One of the largest problems with a hydrostatic driven setup is lack of knowledge of the actual flow rates. Even though the flow in principle can be calculated if the geometry is known, it will often show in practice that air bubbles and fabrication/material imperfections make the calculations obsolete. So, in order to measure the flow rate inside the chip, I got the idea of using the cytometer as a flow meter.

The idea is to send particles through the chip as usual while recording at a fixed known sampling rate (here 80 kHz). From the data it is then possible to measure the width of the resulting peaks. We will, however, find out, that because of the pressure driven flow (or missing focusing), we have a large velocity distribution and therefore also peak width distribution. However, knowing the shape of the channel, we also know how the maximum flow velocity relates to the total flow rate (see Eq. (4.11) and Eq. (4.12)); thus, by determining the minimum peak width we can deduce the maximum velocity and thereby the total flow rate. Unfortunately, with the large distribution of peak heights, it is necessary to operate with two peak height thresholds. One low threshold (here 8mV) used to determine when a data point is high enough to be an event rather than part of the baseline. And a second threshold (150 mV) used to make sure that the evaluated peaks are sufficiently high, so they do not only cross the first threshold with a single data point or so. This means that we can use the upper threshold to calibrate our measurement.

To test this idea, a range of measurements was made with flow rates varying between 2 and 30 $\mu$L/min using a solution of 2 $\mu$m particles at a concentration of 500 particles/$\mu$L. By setting the upper threshold to 0.15 V and the laser beam width to 15 $\mu$m (see Section 7.4.2.5) we obtain the plot in Fig. 7.34.
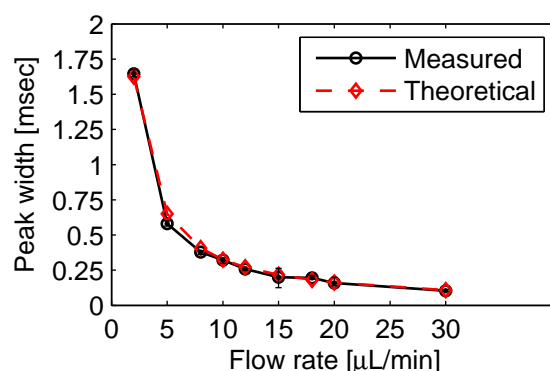
*Figure 7.34: This plot shows that the measured peak width corresponds very well to theoretical values, indicating that the cytometer can be used as a flowmeter. Each point represents the average value of 3-4 measurements. Increasing the threshold value shifts the measured values upwards. Notice the errorbars indicate the min/max value of the measurements. Color reprint in Appendix C*

Based on this result it seems very likely that the cytometer chip can actually be used to obtain the flow rate. However, the effective operation range may very well be limited. One obvious problem of this method is the highly nonlinear response that causes the sensitivity to be very low at flow rates above 25 $\mu$L/min. At the other end of the scale the lower flow rates cause the number of detected particles to be lower and lower, hence due to the statistical nature of the measurements the results become less precise. Though this flowmeter concept is expected to be used in future setups, the limited range and the need for particles makes it unlikely that this kind of flowmeter will be a commercial success.

# Concluding remarks

## 8.1 Chip summary

The performance of the six produced chips are summarized in Table 8.1.

*Table 8.1: This table provides an overview of the six generations of chips fabricated during this project. Only the third and the sixth generation chip were successful at counting the passing particles*

| Generation | Technology | Flow focusing | Detection angle | Detection limit |
|---|---|---|---|---|
| 1 | Silicon/SU-8/PDMS | 2D | $\sim 35°$ | 5 $\mu$m |
| 2 | Silicon/SU-8/PDMS | 2D | $35°$ | 1 $\mu$m |
| 3 | PDMS/SU-8/Glass | 3D | $17° - 44°$ | 0.5 $\mu$m |
| 4 | Glass/SU-8/PDMS | *Failed* | $\sim 40°$ | *unknown* |
| 5 | Glass/SU-8/PDMS | *Failed* | $11° - 18°$ | 0.5 $\mu$m |
| 6 | Glass/SU-8/PDMS | *none* | $11° - 23°$ | 0.5 $\mu$m |

Due to poor performance, the tests on the fourth generation chip were aborted before the detection limit was found. Only with the third generation chip was it possible to effectively separate the particle signal from the baseline noise. This was, however, most likely a result of the well implemented 3D focusing flow. The chips from generation four to six were all built according to the chip-in-a-case concept, which greatly improved the chip handling. These three chips were all designed with an incoupling lens rather than a fiber alignment groove. The sixth generation chip was made entirely without waveguides, using lenses for both in- and outcoupling of the light. Hence, the sixth generation chip achieved plug and play functionality.

## 8.2 Future perspectives

### 8.2.1 3rd generation

The 3rd generation chip ended up being the chip with the best performance of all the chips. Unfortunately, the design seemed to be a dead end road, as the overall handling

of the chip was terrible. The concept of inserting the optical fibers into the chip worked fine in the lab environment, but after introducing it to our collaborators it became clear that the fiber-based solution was far from user friendly. It should, however, be noted that after replacing the microscope objective and fiber alignment platform with a collimation lens the coupling of light into the fiber became much easier (see Section 6.3.1). This kind of approach is therefore highly recommended to people who, after reading this thesis, still insist on using optical fibers.

The third generation chip showed that with 3D hydrodynamic focusing the quality of the signal was greatly enhanced. However, it also showed that the establishing of such a flow was much more difficult than first realized. Combining this with the high number of required inlets, I find it unlikely that this kind of fluidic setup will have much success in the future. But if the 3D focusing somehow can be realized in a much simpler and easier way, it will be a key component of high-end on-chip cytometry.

### 8.2.2    6th generation

The sixth generation chip showed that the combination of the chip-in-a-case concept and the lens based coupling technique made it possible to very easily position an optical $\mu$TAS device into an instrument with sufficient accuracy to successfully couple light into, and out of, the chip. This technique worked so well that I find it very likely to see it successfully implemented in many other types of optical micro devices in the future. The possibility of providing a functional plug and play platform is a huge step towards a higher level of POC. So the lens coupling system is in my opinion a solution that should be seriously considered for future projects.

Another important aspect of flow cytometry, indicated by the sixth generation chip, is the possibility to avoid flow focusing completely for certain less sensitive applications. Being able to lower not only the number of chip in- and outlets, but also the number of pumps needed to drive the application, provides a great simplification of the entire setup. The reduction of device complexity may in many cases help bring the given application closer to the desired level of POC, even though it comes at the cost of a lowered sensitivity. As a future project it could be very interesting to closer examine how simple a flow cytometer can be, while still providing useful data.

Due to time restraints, there exists a number of interesting topics regarding the lens based coupling concept, which have not been covered during this project. One of the most obvious topics to look at is the dependence of the thickness of the planar waveguide layer (in this case SU-8). The question that remains unanswered is how thin (or thick) this layer can be made, while still being able to collect a sufficient portion of the incident light. With very thin layers, the critical issue may be the focusing ability of the external lens. In the work presented in Chapter 7, the external lens was more or less arbitrarily chosen among many with slightly varying specifications. Hence, the vertical focusing might be further optimized by selecting a better suited lens. It would be very interesting to investigate whether it is possible to make the external lenses in PMMA by micromilling, thereby lowering the cost significantly and perhaps even tailor the design of the external lenses. If the waveguide layer becomes very thin and the vertical focus also is severely improved, it

might turn out that the z-alignment method no longer is accurate enough. If future tests prove that this system is effective even with very thin layers, it may even be possible to use the lenses to couple light into single mode waveguides.

A second issue that could be interesting to investigate is whether the SU-8 layer could be replaced by another more transparent material. If a material with lower absorption at shorter wavelengths ($< 600$ nm) was used instead, the incident wavelength could be lowered. This might not only result in better scattering signals, but could also be used for measurements on fluorescent particles.

This leads us to the third issue: Could several detectors be used in combination with the plug and play lens system? In all the chip designs, where fibers were used for the optical output, two detectors were used to collect the scattered light from each side of the incident beam. However, with the lens design used in the sixth generation chip, the light from both sides is directed towards the same detector. By correlating the data from two (or more) detectors the signal to noise ratio may be enhanced. And, in the case of fluorescent particles, one of the detectors could be fitted with a narrow optical band filter, thereby enabling detection of the fluorescent signals. From a theoretical point of view, the layout of the chip could easily be changed, such that light would be sent towards different detectors. But since this has not been tested in the laboratory I am concerned that this might not work practically. The addition of more detectors could increase the accuracy requirement for the chip position, thereby making the current pin aided system insufficient.

A fourth thing that should have been tested had time allowed it, was the level of performance among the various described lens shapes. Both to see how well the calculation of the focal width actually matches that of the real devices, but also to find out what range of f-numbers is possible to achieve with the current fabrication process.

Finally, the issue of the lacking 3D hydrodynamic focusing should be solved.

If a setup based on the sixth generation chip were to be commercialized, then there are at least two major issues that must be dealt with first. The first, and possibly the most difficult, issue is the price tag of each chip. As the chips are currently being fabricated using cleanroom techniques the price per chip quickly increases beyond 100 EUR. This price can of course be decreased with large scale fabrication and by decreasing the chip size to allow more chips per wafer. But if the price of this kind of chip really has to go down, the fabrication must happen outside the cleanroom, by injection molding or other cheap alternative methods. My experience with these chips does indicate that it is possible to clean the chips in between measurements. Hence, if a chip can be used several times, a somewhat higher price can be acceptable. It is, though, necessary to stress that the chips once used, never can be regarded as 100 % clean again, hence recycling the chips may not be valid under clinical test conditions.

The second issue with turning this setup into a low cost device, is the use of a personal computer to acquire and process the data. The addition of an entire computer to the setup adds to both the total value, as well as to the physical size of the collected instrument. By substituting the computer by a custom made electronic system based on a fast micro-processor such as the AVR XMEGA A3 [71] both price and size can be greatly reduced. The AVR XMEGA A3 runs at 32 MHz and is capable of sampling at 2 Msps using the

two available eight channel analog to digital converters allowing 12 bit accuracy. Hence, such a 5-7 EUR microprocessor could be capable of replacing the computer. Even after including a power supply, an lcd display, some buttons for user interaction and finally a storage media where the obtained data can be saved, the total price of the electronic system can be made at one tenth of the cost of a regular computer.

## 8.3 Conclusion

One of early lessons learned in this project was the advantage of having a proper collimation lens when coupling light into optical fibers (Section 6.3.1). By having the collimation lens in a two-axis angular mount and the laser on a three-axis (two-axis would have been enough) microstage, the alignment procedure became a lot easier.

Another lesson learned was necessity of adding a surface treatment step based on AP300 to the fabrication process in order to obtain a sufficiently high adhesion strength between the smallest SU-8 structures and the glass substrate. By using glass substrates instead of silicon, it became much easier to inspect the devices with microscopes both during assembly and tests.

The scatter structure described in Section 6.1.2.1 and Section 7.1.2 proved very effective in coupling the unwanted stray light out of the chip plane. Though the scatter structure, due to simplicity issues, was not implemented in the design of the 6th generation chip, it should be considered for future designs. The scatter structure offers an easy opportunity to shield certain areas of the chip from stray light, and also provides important information about which parts of the chips are illuminated.

With the development of the RayLab (Chapter 3) software it became a lot easier to simulate and fabricate complex geometries such as the tailored lenses. One can only guess how differently this project would have evolved had I not taken the time to write that program.

The 3rd generation chip presented in Section 6.2 has shown that a micro flow cytometer can be designed and fabricated that is capable of detecting and counting unlabeled particles down to a size of 1 $\mu$m at a rate of at least 5 Hz. To my knowledge, this is first time that unlabeled particles down to 1 $\mu$m have been detected on-chip by light scattering. With microfluidic channels fabricated in both the SU-8 layer and in the PDMS, three dimensional hydrodynamic focusing was successfully achieved. With the established 3D focusing the dispersion in signal strength became much lower, and it was possible to completely separate both 2 $\mu$m and 1 $\mu$m particles from the background noise.

During the progress from the third generation towards the sixth, the development of the Chip-in-a-case concept showed that it was possible to completely separate the chip fabrication process from the test process. This separation is a very big advantage as it takes the complexity of assembling the chip away from the end user. Furthermore, the case provided an efficient and easily reproducible method to seal the chips. The case also provided good protection for the otherwise fragile chips. With the developed lens system, the case also played an important role in the alignment process of the chip.

By taking advantage of the Chip-in-a-case concept combined with the elasticity of the

PDMS lid, it was possible to fabricate a fluidic connector (see Fig. 7.4 and Fig. 7.20) that could simultaneously connect multiple in- and outlets. Except for the potential risk of trapping air bubbles, the connector showed plug and play performance. By being able to completely detach the fluidic connector from the chip, it was possible to drive pure water through the tubings at very high flow rates, thereby efficiently cleaning the connector.

Even though 3D focusing was never achieved with the 6th generation chip, the idea of creating out-of-plane connection loops (see Fig. 7.11), by inserting fishing line in the PDMS mould, was found to work very well. Since fishing line is cheap and comes in many different diameters, this approach is both easy and flexible. It was, however, never confirmed whether the channel-loop had a positive or negative effect on the flow focusing.

In Section 7.3.4.2 the theory of the on-chip tailored lens was described, the predicted results matched very well to those obtained through ray tracing simulations. The actual performance of the produced lenses, in terms of focus width, was only briefly investigated for one of the lens designs (see Fig. 7.28). Though the focus width was found to be slightly larger than expected, the overall performance of the lenses was very good.

With the 6th generation cytometer-chip it was shown that, by using the proposed lens system, the waveguide structures could be entirely avoided. This meant that, for the first time, the SU-8 layer could be made without any small free standing structures, thereby eliminating the necessity of using any adhesion promoters during fabrication.

The very small differences in the coupling quality for the rotation-chip in Section 7.3.6.1 showed that the pin-aided alignment system was capable of aligning the chip sufficiently well. With a standard deviation of the transmitted intensity at only 2.1 % for the entire chip and down to 0.1 % for the best of the corners, these results are considered very good. Keeping in mind that these replacement tests were performed by coworkers with very little training, the plug and play functionality of the entire lens based system is demonstrated. Furthermore, the test in Section 7.4.2.4, demonstrated that even the sixth generation cytometer-chip could be picked up, and repositioned, during tests without losing the optical alignment.

In Section 7.3.6.2 it has been demonstrated that particles down to 1 $\mu$m can be detected and counted reliably at 100 Hz for concentrations below 300 particles/$\mu$L without any form of flow focusing. 2 $\mu$m particles could be counted up to concentrations of at least 600 particles/$\mu$L. The lack of flow focusing does, however, mean that calibration of the data is necessary.

The functionality of the lens system has also been proven efficient for non-cytometry applications, exemplified by the absorption measurement in Section 7.4.4.2, where the chip design demonstrated an easy way to obtain a reference output, which can be used to avoid drift in the laser intensity. Furthermore, it was shown that the cytometer-cip could be used as a flowmeter (see Section 7.4.4.3) by evaluating the width of the detected peaks. This was demonstrated to work very well within a flow rate range of 5 - 25 $\mu$L/min.

The preliminary tests from Section 7.4.3.1 have shown that with calibration measurements, the non-hydrodynamically focused cytometer, can to some extent, count the largest particles in mixed populations. This result was especially interesting, as doublet detection was the overall goal for the DetectHIV project. Hence, this much simpler approach might help to greatly simplify the entire instrument.

So, as a final remark, it is stated that, even though more work is needed, this project has shown that it is possible to fabricate miniaturized flow cytometers for implementation in $\mu$TAS devices, which are able to detect and count particles down to 1 $\mu$m whether based on optical fibers or on-chip lenses. It has been demonstrated that these lens-based devices can be used without the need of expensive lasers and PMTs, hence opening the possibility of building a very low cost cytometer either as a stand alone device or as an integrated part of $\mu$TAS device. It has also been demonstrated that even though 3D flow focusing greatly improves the signal quality, it might not be necessary for all applications, thereby making it possible to create much simpler and cheaper devices.

Finally, the developed lens system demonstrated how the on-chip lenses could be used both for focusing the light directly at the detection channel or to couple light in and out of waveguides. This flexibility, combined with the demonstrated plug and play functionality resulted in a novel, highly user-friendly optical setup, that hopefully will contribute to bring future $\mu$TAS-devices closer towards the Point-Of-Care.

# Bibliography

[1] A. Manz, N. Graber, and H. M. Widmer. Miniaturized total chemical-analysis systems - a novel concept for chemical sensing. *Sensors and Actuators B-Chemical*, 1(1-6):244–248, 1990.

[2] http://www.i cyt.com. Datasheet: Eclipse flow cytomtry analyzer, Retrieved: 10. Oct 2010. `http://www.i-cyt.com/pdf/eclipse_specifications.pdf`.

[3] A. Orfao and A. RuizArguelles. General concepts about cell sorting techniques. *Clinical Biochemistry*, 29(1):5–9, 1996.

[4] G. Whitesides. Solving problems. *Lab on a Chip*, 10(18):2317–2318, 2010.

[5] D. Sabourin, M. Dufva, T. G. Jensen, J. P. Kutter, and D. Snakenborg. One-step fabrication of microfluidic chips with in-plane, adhesive-free interconnections. *Journal of Micromechanics and Microengineering*, 20(3):7, 2010.

[6] D. J. Griffiths. *Introduction to Electrodynamics*. Prentice Hall Inc, (New Jersey), 3 edition, 1999. Chapter 9.

[7] R. Syms and J Cozens. *Optical Guided Waves and Devices*. McGRAW-HILL Book Company, Europe, 1 edition, 1992.

[8] M Diem. *Introduction to Modern Vibrational Spectroscopy*. Wiley, 1 edition, 1993.

[9] D. A. Skoog, D. M. West, F. J. Holler, and S. R. Crouch. *Fundamentals of analytical chemistry*. Thomson-Brooks/Cole., 8 edition, 2004. Part V.

[10] K. N. Liou. *An Introduction to Atmospheric Radiation*. Elsevier Science (USA), 2 edition, 2002.

[11] A Ungut, G Grehan, and G Gouesbet. Comparisons Between Geometrical-Optics And Lorenz-Mie Theory. *Applied Optics*, 20(17):2911–2918, 1981.

[12] G Mie. Articles on the optical characteristics of turbid tubes, especially colloidal metal solutions. *Annalen Der Physik*, 25(3):377–445, Mar 1908. Translations available at `http://diogenes.iwt.uni-bremen.de/vt/laser/papers/RAE-LT1873-1976-Mie-1908-translation.pdf` and `http://diogenes.iwt.uni-bremen.de/vt/laser/papers/SAND78-6018-Mie-1908-translation.pdf`,.

[13] M. Kerker. *The Scattering Of Light And Other Electromagnetic Radiation*. Academic Press Inc, (New York), 2 edition, 1969. Chapter 3.

[14] P. Laven. Simulation of rainbows, coronas, and glories by use of mie theory. *Applied Optics*, 42(3):436–444, 2003.

[15] S. N. Kasarova, N. G. Sultanova, C. D. Ivanov, and I. D. Nikolov. Analysis of the dispersion of optical plastic materials. *Optical Materials*, 29(11):1481–1490, 2007.

[16] M. J. Berg, S. C. Hill, G. Videen, and K. P. Gurton. Spatial filtering technique to image and measure two-dimensional near-forward scattering from single particles. *Optics Express*, 18(9):9486–9495, 2010.

[17] D. T. Phillips, P. J. Wyatt, and R. M. Berkman. Measurement of lorenz-mie scattering of a single particle - polystyrene latex. *Journal of Colloid and Interface Science*, 34(1):159–162, 1970.

[18] Ian Moore. Raytrace v. 2.22, 2006. `http://www.ozemail.com.au/~imesoft`.

[19] Sven Melker Hagsäter. *Development of micro-PIV techniques for application in microfluidic systems*. PhD thesis, Department of Micro and Nanotechnology, Technical University of Denmark, 2008.

[20] Tanner EDA. L-edit v.12, 2006. `http://www.tannereda.com`.

[21] D. A. Zauner, A. M. Jorgensen, T. A. Anhoj, and J. Hubner. High-density multimode integrated polymer optics. *Journal of Optics a-Pure and Applied Optics*, 7(9):445–450, 2005.

[22] H Bruus. *Theoretical Microfluidics*. Oxford University Press, USA, 1 edition, 2007.

[23] *Handbook of Chemistry and Physics Online*. CRC Press, 87 edition, 2006-2007. `http://www.hbcpnetbase.com/` Section 14, Speed of sound in various media.

[24] J. Nilsson, M. Evander, B. Hammarstrom, and T. Laurell. Review of cell and particle trapping in microfluidic systems. *Analytica Chimica Acta*, 649(2):141–157, 2009.

[25] A. N. Grigorenko, N. W. Roberts, M. R. Dickinson, and Y. Zhang. Nanometric optical tweezers based on nanostructured substrates. *Nature Photonics*, 2(6):365–370, 2008.

[26] C. Piggee. Optical tweezers: not just for physicists anymore. *Analytical Chemistry*, 81(1):16–19, 2009.

[27] Zhenyu Wang. *Applications of Integrated Polymer Waveguides in Microsystems*. PhD thesis, Department of Micro and Nanotechnology, Technical University of Denmark, 2006.

[28] Z. Wang, J. El-Ali, M. Engelund, T. Gotsaed, I. R. Perch-Nielsen, K. B. Mogensen, D. Snakenborg, J. P. Kutter, and A. Wolff. Measurements of scattered light on a microchip flow cytometer with integrated polymer based optical elements. *Lab on a Chip*, 4(4):372–377, 2004.

[29] W. Mandecki, B. Ardelt, T. Coradetti, H. Davidowitz, J. A. Flint, Z. L. Huang, W. M. Kopacka, X. Lin, Z. Y. Wang, and Z. Darzynkiewicz. Microtransponders, the miniature rfid electronic chips, as platforms for cell growth in cytotoxicity assays. *Cytometry Part A*, 69A(11):1097–1105, 2006.

[30] K Cheung, S Gawad, and P Renaud. Impedance spectroscopy flow cytometry: On-chip label-free cell differentiation. *Cytometry Part A*, 65A(2):124–132, JUN 2005.

[31] J. Kruger, K. Singh, A. O'Neill, C. Jackson, A. Morrison, and P. O'Brien. Development of a microfluidic device for fluorescence activated cell sorting. *Journal of Micromechanics and Microengineering*, 12(4):486–494, 2002.

[32] M. B. Wabuyele, S. M. Ford, W. Stryjewski, J. Barrow, and S. A. Soper. Single molecule detection of double-stranded dna in poly(methylmethacrylate) and polycarbonate microfluidic devices. *Electrophoresis*, 22(18):3939–3948, 2001.

[33] M. E. Davis, Z. Chen, and D. M. Shin. Nanoparticle therapeutics: an emerging treatment modality for cancer. *Nature Reviews Drug Discovery*, 7(9):771–782, 2008.

[34] D. A. LaVan, T. McGuire, and R. Langer. Small-scale systems for in vivo drug delivery. *Nature Biotechnology*, 21(10):1184–1191, 2003.

[35] L. L. Yang, S. B. Zhu, W. Hang, L. Wu, and X. M. Yan. Development of an ultrasensitive dual-channel flow cytometer for the individual analysis of nanosized particles and biomolecules. *Analytical Chemistry*, 81(7):2555–2563, 2009.

[36] T. Hirono, H. Arimoto, S. Okawa, and Y. Yamada. Microfluidic image cytometry for measuring number and sizes of biological cells flowing through a microchannel using the micro-piv technique. *Measurement Science & Technology*, 19(2), 2008.

[37] K. Singh, X. T. Su, C. G. Liu, C. Capjack, W. Rozmus, and C. J. Backhouse. A miniaturized wide-angle 2d cytometer. *Cytometry Part A*, 69A(4):307–315, 2006.

[38] Joel P. Golden, Jason S. Kim, Jeffrey S. Erickson, Lisa R. Hilliard, Peter B. Howell, George P. Anderson, Mansoor Nasir, and Frances S. Ligler. Multi-wavelength microflow cytometer using groove-generated sheath flow. *Lab on a Chip*, 9(13):1942–1950, 2009.

[39] H. P. Zhang, C. H. Chon, X. X. Pan, and D. Q. Li. Methods for counting particles in microfluidic applications. *Microfluidics and Nanofluidics*, 7(6):739–749, 2009.

[40] X. H. Cheng, D. Irimia, M. Dixon, K. Sekine, U. Demirci, L. Zamir, R. G. Tompkins, W. Rodriguez, and M. Toner. A microfluidic device for practical label-free cd4+t cell counting of hiv-infected subjects. *Lab on a Chip*, 7(2):170–178, 2007.

[41] C. C. Chang, Z. X. Huang, and R. J. Yang. Three-dimensional hydrodynamic focusing in two-layer polydimethylsiloxane (pdms) microchannels. *Journal of Micromechanics and Microengineering*, 17(8):1479–1486, 2007.

[42] H. Y. Wang, A. K. Bhunia, and C. Lu. A microfluidic flow-through device for high throughput electrical lysis of bacterial cells based on continuous dc voltage. *Biosensors & Bioelectronics*, 22(5):582–588, 2006.

[43] S. Gawad, L. Schild, and P. Renaud. Micromachined impedance spectroscopy flow cytometer for cell analysis and particle sizing. *Lab on a Chip*, 1(1):76–82, 2001.

[44] R. Bernini, E. De Nuccio, F. Brescia, A. Minardo, L. Zeni, P. M. Sarro, R. Palumbo, and M. R. Scarfi. Development and characterization of an integrated silicon micro flow cytometer. *Analytical and Bioanalytical Chemistry*, 386(5):1267–1272, 2006.

[45] Y. N. Wang, Y. J. Kang, D. Y. Xu, C. H. Chon, L. Barnett, S. A. Kalams, D. Y. Li, and D. Q. Li. On-chip counting the number and the percentage of cd4+t lymphocytes. *Lab on a Chip*, 8(2):309–315, 2008.

[46] H. T. Chen and Y. N. Wang. Optical microflow cytometer for particle counting, sizing and fluorescence detection. *Microfluidics and Nanofluidics*, 6(4):529–537, 2009.

[47] N. Sundararajan, M. S. Pio, L. P. Lee, and A. A. Berlin. Three-dimensional hydrodynamic focusing in polydimethylsiloxane (pdms) microchannels. *Journal of Microelectromechanical Systems*, 13(4):559–567, 2004.

[48] N. Watkins, B. M. Venkatesan, M. Toner, W. Rodriguez, and R. Bashir. A robust electrical microcytometer with 3-dimensional hydrofocusing. *Lab on a Chip*, 9(22):3177–3184, 2009.

[49] X. L. Mao, J. R. Waldeisen, and T. J. Huang. "microfluidic drifting" - implementing three-dimensional hydrodynamic focusing with a single-layer planar microfluidic device. *Lab on a Chip*, 7(10):1260–1262, 2007.

[50] J. S. Kee, D. P. Poenar, P. Neuzil, and L. Yobas. Monolithic integration of poly(dimethylsiloxane) waveguides and microfluidics for on-chip absorbance measurements. *Sensors and Actuators B-Chemical*, 134(2):532–538, 2008.

[51] S. K. Y. Tang, C. A. Stan, and G. M. Whitesides. Dynamically reconfigurable liquid-core liquid-cladding lens in a microfluidic channel. *Lab on a Chip*, 8(3):395–401, 2008.

[52] M. Rosenauer and M. J. Vellekoop. 3d fluidic lens shaping-a multiconvex hydrodynamically adjustable optofluidic microlens. *Lab on a Chip*, 9(8):1040–1042, 2009.

[53] K. B. Mogensen, J. El-Ali, A. Wolff, and J. P. Kutter. Integration of polymer waveguides for optical detection in microfabricated chemical analysis systems. *Applied Optics*, 42(19):4072–4079, 2003.

[54] C. Simonnet and A. Groisman. Two-dimensional hydrodynamic focusing in a simple microfluidic device. *Applied Physics Letters*, 87(11), 2005.

[55] C. M. Chang, S. K. Hsiung, and G. B. Lee. Micro flow cytometer chip integrated with micro-pumps/micro-valves for multi-wavelength cell counting and sorting. *Japanese Journal of Applied Physics Part 1-Regular Papers Brief Communications & Review Papers*, 46(5A):3126–3134, 2007.

[56] G. Hairer and M. J. Vellekoop. An integrated flow-cell for full sample stream control. *Microfluidics and Nanofluidics*, 7(5):647–658, 2009.

[57] D. Snakenborg, G. Perozziello, H. Klank, O. Geschke, and J. P. Kutter. Direct milling and casting of polymer-based optical waveguides for improved transparency in the visible range. *Journal of Micromechanics and Microengineering*, 16(2):375–381, 2006.

[58] S. Krawczyk. Discussion on optical integration in lab-on-a-chip microsystems for medical diagnostics. *physica status solidi (c)*, 0:998–1012, 2003.

[59] B. Kuswandi, Nuriman, J. Huskens, and W. Verboom. Optical sensing systems for microfluidic devices: A review. *Analytica Chimica Acta*, 601(2):141–155, 2007.

[60] F. B. Myers and L. P. Lee. Innovations in optical microfluidic technologies for point-of-care diagnostics. *Lab on a Chip*, 8(12):2015–2031, 2008.

[61] N. C. H. Le, R. Yokokawa, D. V. Dao, T. D. Nguyen, J. C. Wells, and S. Sugiyama. Versatile microfluidic total internal reflection (tir)-based devices: Application to microbeads velocity measurement and single molecule detection with upright and inverted microscope. *Lab on a Chip*, 9(2):244–250, 2009.

[62] S. Balslev, A. M. Jorgensen, B. Bilenberg, K. B. Mogensen, D. Snakenborg, O. Geschke, J. P. Kutter, and A. Kristensen. Lab-on-a-chip with integrated optical transducers. *Lab on a Chip*, 6(2):213–217, 2006.

[63] J. A. Chediak, Z. S. Luo, J. G. Seo, N. Cheung, L. P. Lee, and T. D. Sands. Heterogeneous integration of cds filters with gan leds for fluorescence detection microsystems. *Sensors and Actuators a-Physical*, 111(1):1–7, 2004.

[64] A. Llobera, S. Demming, R. Wilke, and S. Buttgenbach. Multiple internal reflection poly(dimethylsiloxane) systems for optical sensing. *Lab on a Chip*, 7:1560–1566, 2007.

[65] C. L. Bliss, J. N. McMullin, and C. J. Backhouse. Rapid fabrication of a microfluidic device with integrated optical waveguides for dna fragment analysis. *Lab on a Chip*, 7:1280–1287, 2007.

[66] B. M. Beam, N. R. Armstrong, and S. B. Mendes. An electroactive fiber optic chip for spectroelectrochemical characterization of ultra-thin redox-active films. *Analyst*, 134(3):454–459, 2009.

[67] M. Rosenauer and M. J. Vellekoop. A versatile liquid-core/liquid-twin-cladding waveguide micro flow cell fabricated by rapid prototyping. *Applied Physics Letters*, 95(16), 2009.

[68] Y. T. Atalay, D. Witters, S. Vermeir, N. Vergauwe, P. Verboven, B. Nicolai, and J. Lammertyn. Design and optimization of a double-enzyme glucose assay in microfluidic lab-on-a-chip. *Biomicrofluidics*, 3(4), 2009.

[69] C. H. Chen, F. Tsai, V. Lien, N. Justis, and Y. H. Lo. Scattering-based cytometric detection using integrated arrayed waveguides with microfluidics. *Ieee Photonics Technology Letters*, 19(5-8):441–443, 2007.

[70] J. Seo and L. P. Lee. Disposable integrated microfluidics with self-aligned planar microlenses. *Sensors and Actuators B-Chemical*, 99(2-3):615–622, 2004.

[71] Atmel Corporation. Xmega a3 user manual, 2010. `http://www.atmel.com/dyn/resources/prod_documents/doc8068.pdf`.

# Fabrication

In this appendix I list the SU-8 fabrication procedures used throughout this project.

## A.1 Process sequence for polymer waveguides on Silicon or Glass wafers

Wafers: 4" 500 $\mu$m Silicon or glass.

<u>Day 1</u>

1. **Cleaning of wafers:**

   (a) Rinse 10 minutes in piranha (4:1 - $H_2SO_4$ : $H_2O_2$)

2. **Dehydrate wafers:**

   (a) Dehydrate wafers in 250°C oven overnight.

3. **Prepare SU-8:**

   (a) Fill SU-8 (XP2075, Microchem) in syringes, to release trapped air bubbles.

<u>Day 2</u>

4. **Spinning of SU-8 on wafers:**

   (a) Only for wafers with 'tricky' structures - Spin on AP300 ($\sim$0.5 ml) at 2500 rpm for 30 seconds. . Then 200 °C hotplate for 3 min.

   (b) Spin on 75 $\mu$m SU-8 in the KS-spinner at 500rpm (acc:100) for 10 sec, then at 3000 rpm (acc: 200) for 30 seconds.

5. **Softbaking of SU-8 layer:**

   (a) Softbake the SU-8 on a hotplate. 4 h at 60 °C, with a temperature ramp of 2 °C/min . Let wafers cool down to 30 °C.

6. **Photolithography:**

   (a) UV exposure through mask. soft contact mode. 5 sec exposure and 5 seconds wait, 7 cycles. Lamp power: 7, constant intensity. only 6 cycles if Silicon

7. **Post exposure bake:**

   (a) Bake the SU-8 on a hotplate. 6 h at 60 °C, with a temperature ramp of 2 °C/min . Let wafers cool down to 30 °C.

## Day 3

8. **Development of SU-8:**

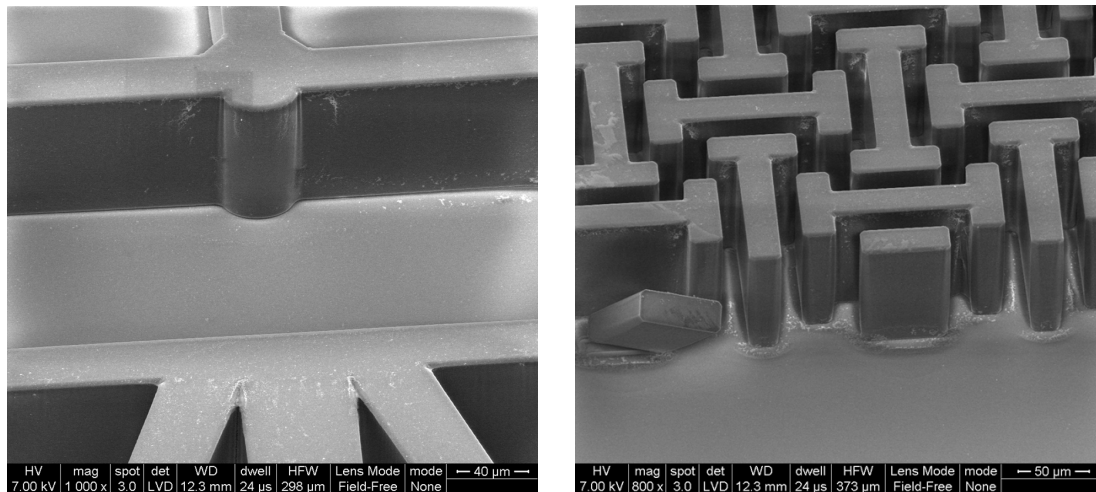   (a) Develop wafers in PGMEA: 6 minutes in "First", then 3 (+1) minutes in "final". Rinse in isopropanol.



*Figure A.1: These SEM images show the center and the scattering structure of the 3rd generation chip. It shows that the sidewalls are very vertical. Courtesy Guisheng Zhuang*

# RayLab

In this appendix I describe the internal structure of the Raylab program and provide some user instructions. The source code can be downloaded or viewed in its entirety online at `www.qlud.dk/RayLab/`.

## B.1  Inside RayLab

The basic structure of RayLab is based on notifiers and while-loops. When the user clicks the `Load File`-button the `Listen`-loop detects the Boolean value change of the button and sets the notifier to `Run Main`. This notifier then triggers the execution of the `Run Main`-case in the `Action`-loop. The first thing RayLab then does, is to call the `File Dialog`-express VI, which allows the user to select the input file using a standard windows browser dialog. Once the filename and path is established, all the light settings from the GUI-controls are gathered and the sub-VI `MakeFileHeader` is called. This sub-VI creates the two output files, and generates the header for both. The header of the CAD script only contains labeling comments. The RAYTRACE script, on the other hand, contains several settings that define the behavior of RAYTRACE. Furthermore, if a light source is selected, then the corresponding code is added to the file header as well. After the headers are completed the parsing of the input file begins.

### B.1.1  Step 0: Count objects

The purpose of this initial step is to divide the text from the input file into a string array, in such a way that each array element contains all the lines corresponding to a specific object. Because of the termination lines inserted in the MatLab script the algorithm is fairly simple, see Fig. B.1.
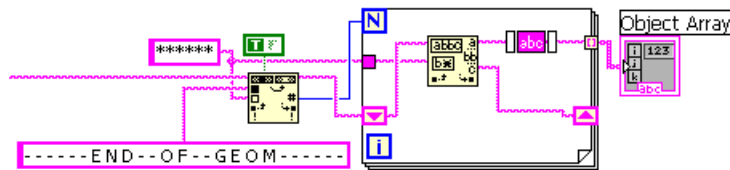
*Figure B.1: The LabVIEW algorithm used to count objects and separate the corresponding strings. The 'TRUE' constant is linked to the replace-all terminal of the 'Search and Replace String'-function. The line entering the code from the left contains the text from the input file as one long string*

The line entering the code from the left contains the text from the input file as one long string. First, the built-in `Search and Replace String`-function is used to count how many times the termination line appears. Secondly, the built-in function `Match Pattern` is combined with a shift-register and a for-loop to separate each object.

### B.1.2   Step 1: Generate Index list

The second step is intended to extract the refractive index information from each object and save it as an array for later use. To achieve this the `Match Pattern`-function is again used, this time to check if the string of each object contains the line defining the refractive index. If the line is found, the value is extracted and the line to be used in the RAYTRACE script is generated and stored in the `Index array`. If the line is not found, the default value is used to generate the line.
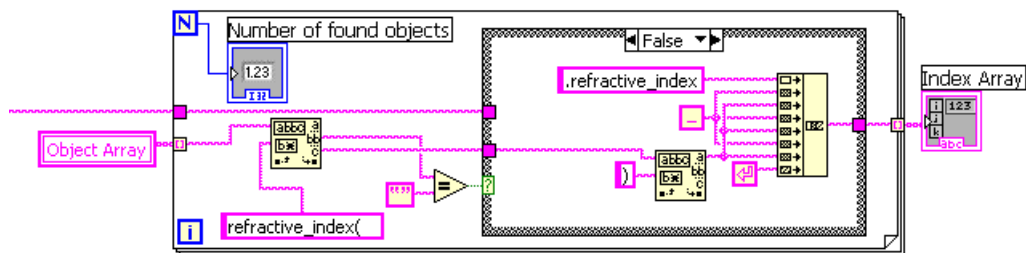


*Figure B.2: The LabVIEW algorithm used to generate the list of refractive indices. The line entering the code from the left contains the default refractive index string.*

Finally, this algorithm (shown in Fig. B.2) finds the total number of objects and displays it on the GUI.

### B.1.3   Step 2: Convert code

The next step for RayLab is to convert the string for each object. By evaluating the first line of the string the type of object can be determined. As shown in Section 3.2.1 the first line in the output of the `rect2()` function is "Rectangle solid object". If

`GetCoords()` is used the first line will be "`PolygoN`". Depending on the type of object, the string is sent to one of four sub-VIs. These will then first parse the string to extract the information and then based on the extracted data generate the code for the two output files. The algorithm responsible for parsing rectangular objects is shown in Fig. B.3.
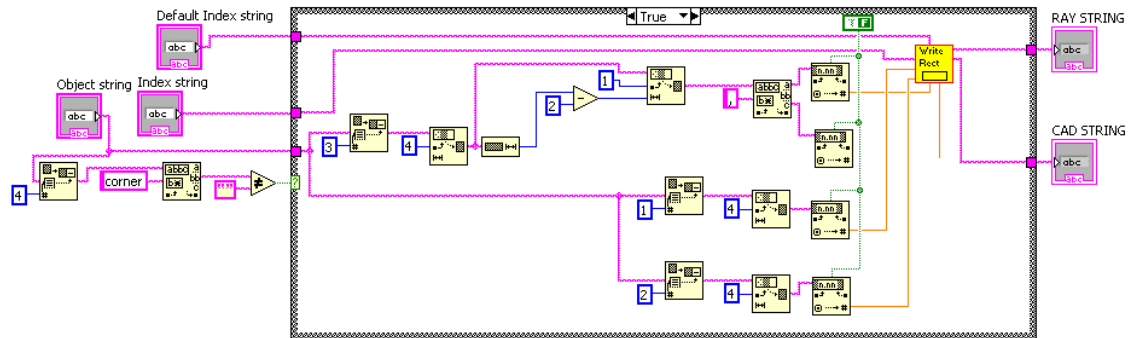


*Figure B.3: The algorithm shown in this figure is responsible for parsing the string corresponding to rectangular objects. After the parsing is completed, the data is sent to the 'WriteRect.vi'*

The first thing this algorithm does, is to look at line 4 of the 'Object string' to see if the rectangle is specified by the corner- or center-point, as this obviously influences the rest of the code. Then, the four defining values are extracted and passed to the sub-VI responsible for generating the output files. The algorithms responsible for ellipses and circles are very similar to the rectangular one. The algorithm for the polygons is, however, much more complicated as it involves much more data, that must be treated through a total of seven steps. The first of these steps is to write the basic script openings. Next, all the $x$ and $y$ data points are extracted and converted from strings to numbers. The sequence of the segments is then determined, and the data points are sorted accordingly. Next, the numbers are converted back into strings and redundant points are removed. Finally, the sorted strings are translated into the two output scripts, which are then closed.

### B.1.4  Step 3: Close scripts

The final step RayLab performs when all objects have been processed is to close the scripts. This is important as they otherwise may cause the programs to freeze or get stuck in scripting mode.

## B.2  RayLab user instructions

The RayLab program can be freely downloaded from `www.qlud.dk/RayLab/` together with the source files and a full code overview. In order to be able to run the RayLab program, either LabVIEW 8.6 or, at least, the "LabVIEW Run-Time Engine 8.6" must be installed. The latter can be downloaded for free from National Instruments' webpage (`www.ni.com`). It is, of course, also necessary to have both Matlab, Comsol and RAYTRACE available to

benefit from the RayLab program. To use the COMSOL functions for scripting, COMSOL must be started using the "COMSOL with Matlab" shortcut.

When using Matlab to build the scripts for defining the studied geometries, there are several different ways to export each geometric object. Four of these methods are illustrated in the demonstration scripts available from the RayLab GUI. In `Demo.m` each object is exported immediately after being defined. On the other hand, the script in `Demo2.m` suppresses all outputs until all objects are defined, at which point they are each exported one by one using `GetCoords()`. The script in `Demo3.m` shows how all the objects can be exported after adding them to the fem-structure ('fem' being the standard name of the main variable used in COMSOL). Finally, `Demo4.m` shows how the objects can be exported one by one without using the `GetCoords()`-functions for the simple objects. The output files from the demonstration scripts end up in the same folder as the individual scripts.

It is important to note that for some reason RAYTRACE does not seem to support long file paths. Hence, if a script will not execute in RAYTRACE it can help to copy it to the desktop and then execute it from there.
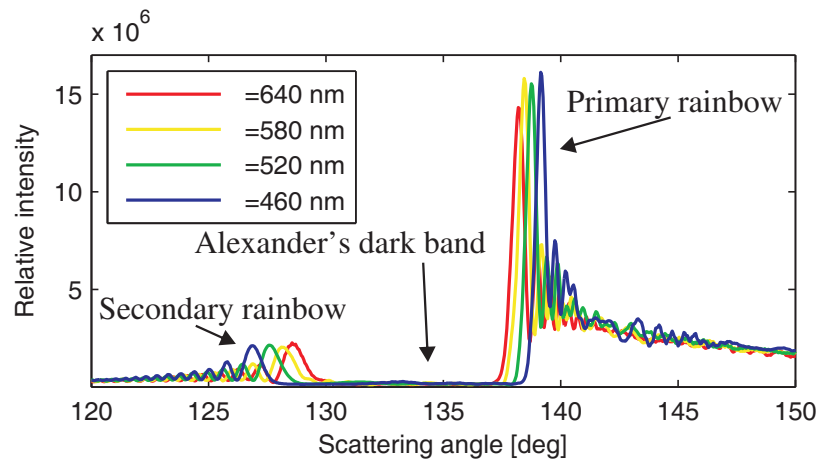
# Color reprints



*Figure C.1: Reprint of Fig. 2.11. This plot shows that it is possible to use the Mie-solutions to predict the angles of the colors in both the primary and secondary rainbow.*
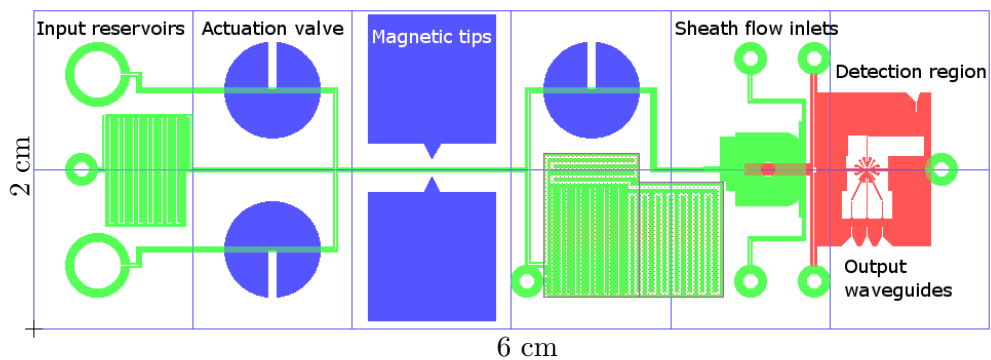


*Figure C.2: Reprint of Fig. 5.5. This figure shows the layout of the integrated chip containing both the magnetic retention and the optical detection modules. The green structures represent the PDMS layer, while red represents structures in SU-8*
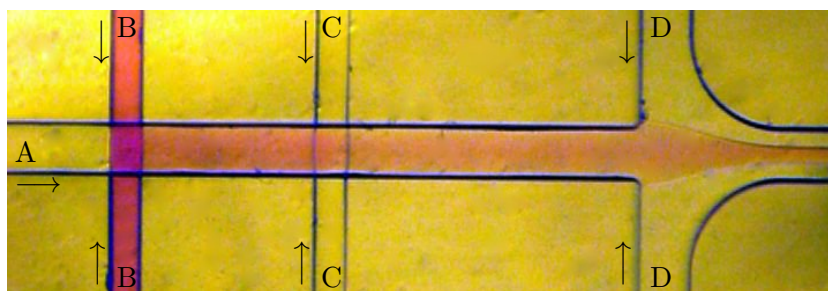
*Figure C.3: Reprint of Fig. 6.19. This figure shows how the dye solution injected into both B-channels gets focused by the buffer flows. First the dye is focused in the out-of-plane direction and then in the in-plane direction. As the flows do not mix, and diffusion can be neglected, the color intensity of the dye can be used as a measure of layer thickness. Hence, the layer of dye is thinner between C and D, than between B and C*
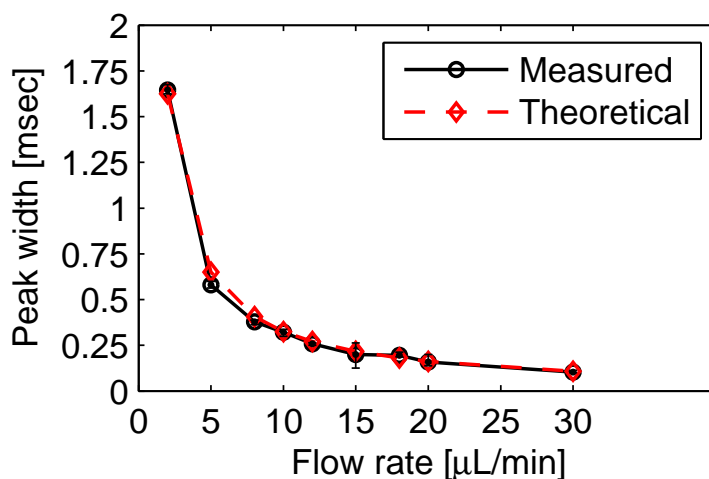


*Figure C.4: Reprint of Fig. 7.34. This plot shows that the measured peak width corresponds very well to theoretical values, indicating that the cytometer can be used as a flowmeter. Each point represents the average value of 3-4 measurements. Increasing the threshold value shifts the measured values upwards. Notice the errorbars indicate the min/max value of the measurements*

3rd Gen.          4th Gen.          5th Gen.
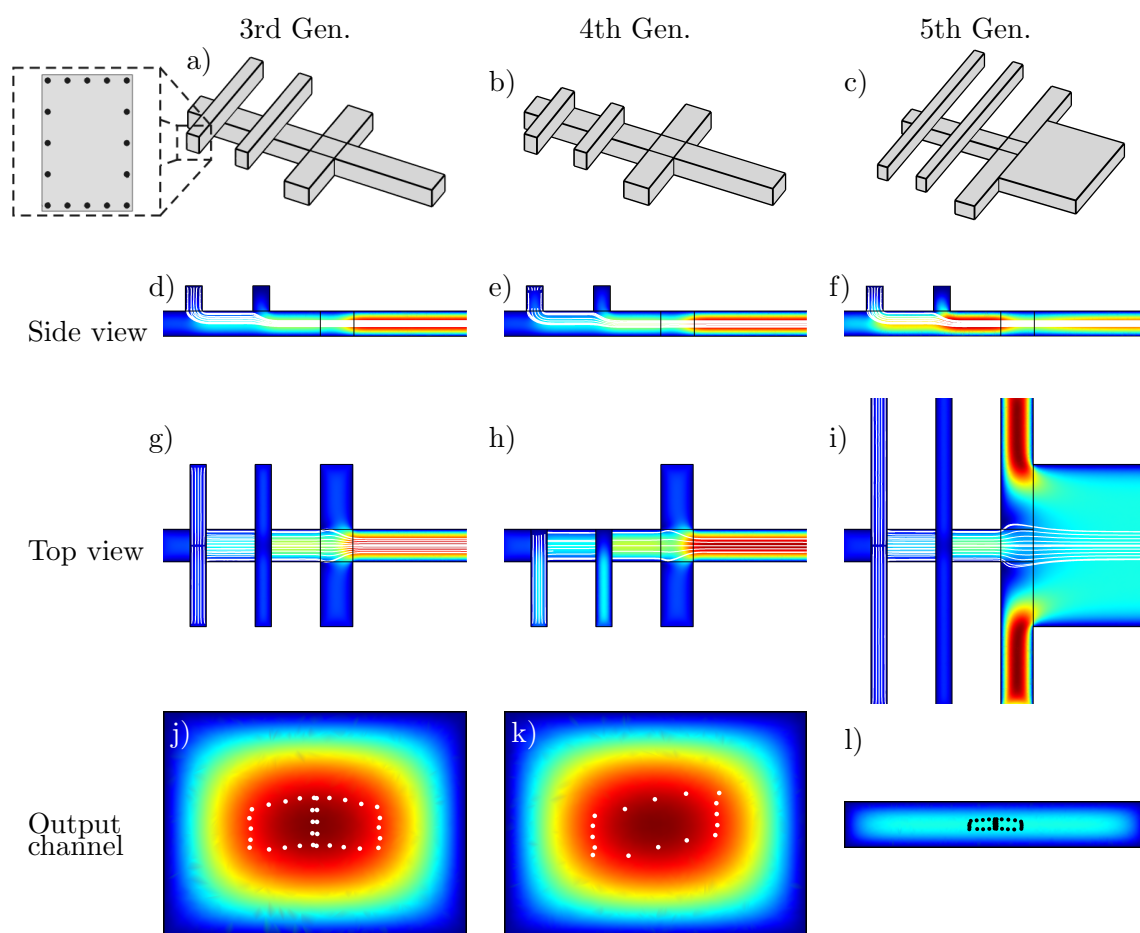
Side view

Top view

Output
channel



Figure C.5: Reprint of Fig. 7.6. This figure shows the result of three flow focus simulations. The displayed streamlines are all starting around the boundary of the sample flow, as shown in Panel a. In Panel j, k and l, it can be seen that the sample-streamlines are well confined to the center of the main channels. The two first simulations were performed at a total flow rate of 10 µL/min evenly distributed on all inlets. For the simulation featuring the wide main channel each in-plane sheath flow was set to 12 µL/min, giving a total flow rate of 30 µL/min
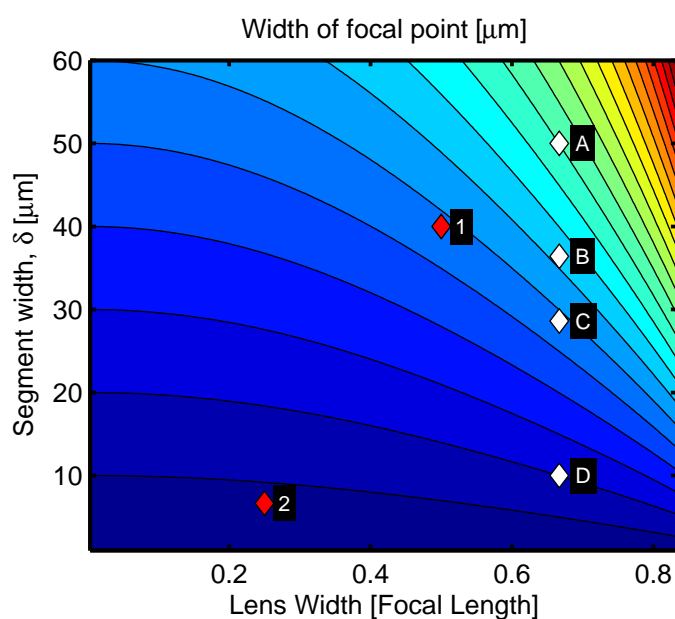
*Figure C.6: Reprint of Fig. 7.16. This figure shows a contour plot of the width of the focal point as a function of relative lens width and the segment width, 'δ'. The numbers here correspond to a refractive index of 1.59 (SU-8). The marks A-D corresponds to the subfigures in Fig. 7.17 respectively. The marks 1 and 2 correspond to the design of the rotation-chip and cytometer chip, respectively (both described below). Notice that for very narrow lenses, the width of the focal point becomes the same as the segment width*
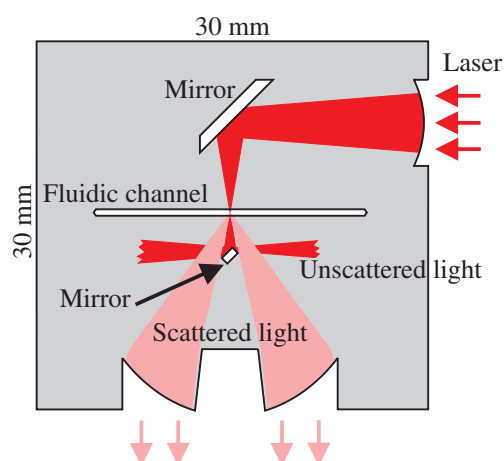


*Figure C.7: Reprint of Fig. 7.19. A sketch of the cytometer-chip. The SU-8 layer (grey) acts as one big planar waveguide. Non-scattered light is separated from the scattered light using an SU-8 mirror. For illustrative purposes objects are not to scale with respect to each other*